Modelling of injection processes in ladle metallurgy

Visser, Hessel-Jan

DOI
10.4233/uuid:1d62a001-7eb5-4faa-9d55-cbe9431c5eee

Publication date
2016

Document Version
Final published version

Citation (APA)
Visser, H.-J. (2016). *Modelling of injection processes in ladle metallurgy*. [Dissertation (TU Delft), Delft University of Technology]. https://doi.org/10.4233/uuid:1d62a001-7eb5-4faa-9d55-cbe9431c5eee

Modelling of injection processes in ladle metallurgy

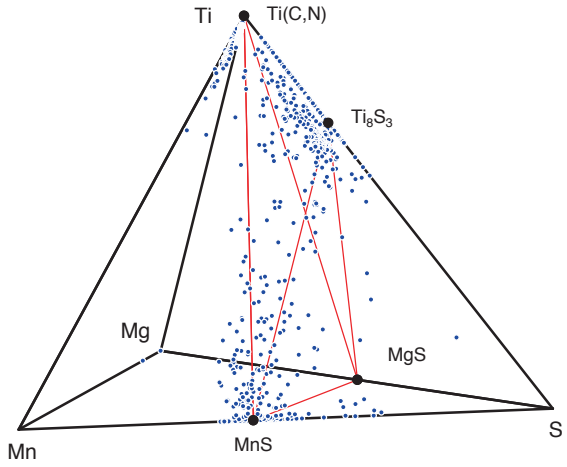

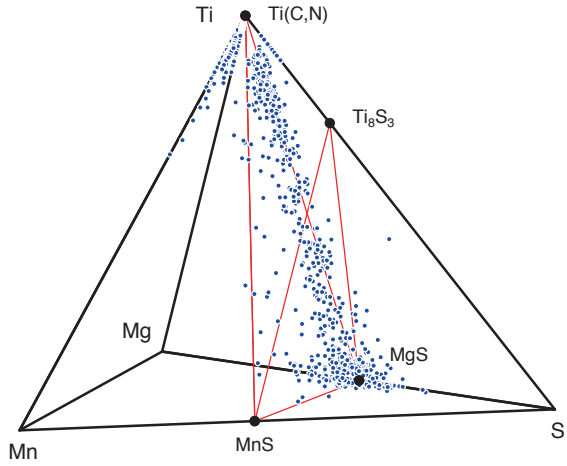

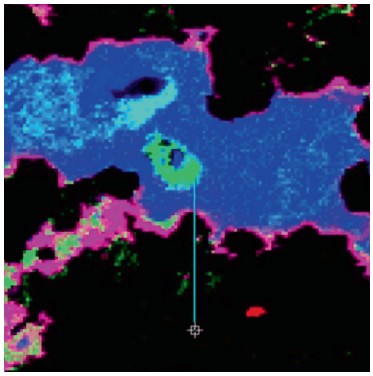

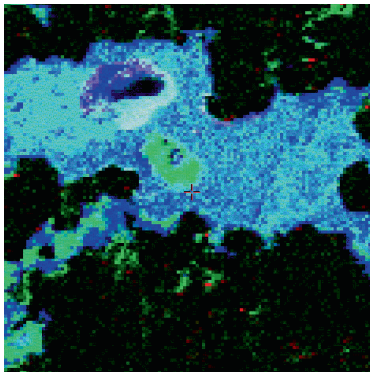

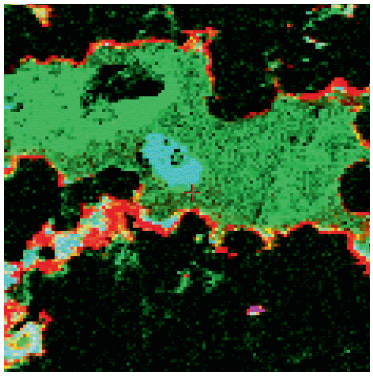

Hessel-Jan Visser

Modelling of injection processes in ladle metallurgy

Hessel-Jan Visser

Title: Modelling of injection processes in ladle metallurgy

Author: H.J. Visser

ISBN: 978-94-91909-29-0

Print: Gildeprint

Modelling of injection processes in ladle metallurgy

Proefschrift

ter verkrijging van de graad van doctor
aan de Technische Universiteit Delft
op gezag van de Rector Magnificus Prof.ir. K.C.A.M Luyben;
voorzitter van het College voor Promoties,
in het openbaar te verdedigen op
woensdag 23 maart 2016 om 10:00 uur

door

Hessel-Jan VISSER

werktuigkundig ingenieur
geboren te Sneek, Nederland

Dit proefschrift is goedgekeurd door:

Prof.dr. R. Boom, promotor

Dr. Y. Yang, copromotor

Samenstelling promotiecommissie:

Rector Magnificus	voorzitter
Prof.dr. R. Boom	Technische Universiteit Delft
Dr. Y. Yang	Technische Universiteit Delft

Onafhankelijke leden:

Prof.dr.ir. J. Sietsma	Technische Universiteit Delft
Prof.dr. B. Deo	Indian Institute of Technology Kanpur
Prof.dr. G. Irons	McMaster University
Prof.dr.ir. J.A.M. Kuipers	Technische Universiteit Eindhoven
Dr.ir. E.M. Beunder	Tata Steel IJmuiden

This research was sponsored by Tata Steel and carried out as part of the programme of the Materials innovation institute M2i under project number MC5.02123.

Contents

Summary

Ladle metallurgical processes constitute a portion of the total production chain of steel from iron ore. With these batch processes, the hot metal or steel transfer ladle is being used as a reactor vessel and a reagent is often injected in order to bring the composition of the hot metal or steel to the specification of the final product. To control and further improve these processes, often use is made of models that predict the course of the processes. Models derived from first principles of mass and energy transport have the advantage over empirical descriptions that predictions outside the established window of operation can be made. The establishment of such a model, however, requires deeper knowledge of the underlying thermo-chemical processes. The purpose of this work is to provide a uniform method for the development of a model of injection processes in the ladle metallurgy. This will give direction to the development of new models, and will clarify blind spots in the existing knowledge for which further research is required. It is chosen to study two ladle treatments and to develop a reactor model of these, namely the desulphurisation of hot metal by the injection of magnesium and lime, and the modification of inclusions in aluminium killed steel by the injection of calcium.

The hot metal desulphurisation has been studied by microscopic analysis of hot metal samples taken during different heats. The top layer of the bath, where the hot metal is in contact with the slag layer, has also been studied. From these analyses, it follows that during the injection of magnesium, magnesium sulphide particles are formed which continue to be present for some time in the hot metal, grow and later on rise out of the bath. This corresponds to the mechanism as has been proposed by G. Irons and R. Guthrie, based on their experiments on a laboratory scale. Due to the differences in scale, however, the accumulation of magnesium sulphide particles in the hot metal plays a significant role in the explanation of sulphur levels observed in the industrial desulphurisation process. The measurements furthermore show that the rise of the particles to the slag layer is partially obstructed by graphite and Ti (C, N) particles that accumulate in the colder surface layer of the hot metal. This creates a layer with a high concentration of MgS-particles that remain unnoticed but can lead to undesirable sulphur pick up in the converter process. It also appears that the MgS particles that rise to the slag layer react with co-injected lime to form MgO and CaS. In order to prevent sulphur reversal by oxidation of MgS in the ambient air, lime should always be injected in a slight excess. During the injection process, iron droplets are thrown up from the spout area. These droplets slowly sink through the slag layer and do not make it back to the hot metal before the end of the injection process. Based on this it can be explained how the hot metal loss depends on the amount of injected magnesium, the hot metal temperature, and the hot metal titanium content. Because these droplets are entrained with the sulphide containing slag during deslagging, this presents a major cost in the form of loss of hot metal.

Based on these findings, a reactor model of the hot metal desulphurisation has been developed The mixing in the hot metal bath has been described as an ideally mixed tank

reactor, wherein the residence time of injected magnesium and lime has been described by a generic model of the bubble plume. An important aspect of the model is that the total sulphur content is formed by the sulphur that is dissolved in the hot metal and the sulphur which is bound in the MgS particles suspended in the hot metal. The specific surface area of the MgS particles is derived from the microscopic observations and the flotation of the MgS particles is described by a first order rate equation. The predicted development of the concentrations of magnesium and sulphur during the duration of the injection is in good agreement with the measurements which have been made with two treatments.

The calcium treatment of aluminium killed steel has been extensively studied by W. Tiekink. Based on the measurements carried out by him on laboratory and industrial scale, the steel bath in the ladle is divided into two reaction zones: a zone plume in which the steel is saturated with calcium and a bulk zone in which initially no calcium is present. In the plume zone CaO and CaS are deposited on the Al_2O_3 particles. Induced by the bubble plume resulting from the calcium injection, a circulating current flows between these zones. Each zone is modelled by a continuously stirred, ideally mixed tank reactor (CISTR). Carried along with this circulating current, the particles are alternately exposed to high and low levels of calcium activity which ultimately results in a variation in size and composition of the particles. This is modelled by taking a population balance of the particles for each zone containing terms for convection and growth by deposition of CaO and CaS. The results of the model are consistent with the observations when it is assumed that the solubility of calcium in steel amounts to 1 ppm. There is a good prediction of particle sizes and composition, but the CaS content of the particles is slightly over-estimated by the model. This is explained by the pick up of oxygen at the surface of the steel which is not yet taken into account in the model.

The final conclusion of this work is that the chemical conversion of the hot metal and steel during ladle metallurgical injection processes can be well modelled with a detailed description of nucleation, growth and rise of the product particles in conjunction with a relatively simple macroscopic description of the flow field in the ladle. This can best be achieved by providing a population balance of the product particles in which, to the extent appropriate, terms for nucleation, growth, convection and flotation are included. The flow field in the ladle then is modelled using three CISTR's coupled by circulating currents of liquid metal. These CISTR's represent the three zones that can be distinguished in a ladle stirred by a bubble plume; the plume zone, the recirculation zone and the stagnant zone above the bottom of the ladle.

Samenvatting

Een onderdeel van de gehele productieketen om ijzererts tot staal om te vormen wordt gevormd door panmetallurgische behandelingen. Bij deze batchprocessen wordt de ruwijzer- of staalpan gebruikt als reactorvat en wordt veelal een reagens geïnjecteerd om de samenstelling van het ruwijzer of het staal op specificatie van het eindproduct te brengen. Om deze processen te besturen en te verbeteren, wordt veelal gebruik gemaakt van modellen die de het verloop van de processen voorspellen. Modellen die zijn opgesteld op basis van onderliggende principes van massa- en energietransport hebben als voordeel boven empirische beschrijvingen dat er voorspellingen buiten het normale werkgebied mee kunnen worden gedaan. Het opstellen vergt echter wel diepere kennis van de onderliggende thermo-chemische processen. Het doel van dit werk is om een uniforme methode geven voor het ontwikkelen van een procesmodel van injectieprocessen in de panmetallurgie. Hiermee kan richting worden gegeven aan de ontwikkeling van nieuwe modellen en kunnen gaten in de bestaande kennis worden blootgelegd waar verder onderzoek noodzakelijk is. Er is hierbij gekozen om twee panbehandelingen te bestuderen en hier vervolgens een reactormodel van te maken, namelijk de ontzwaveling van ruwijzer door de injectie van magnesium en kalk en de modificatie van insluitsels in aluminium rustig staal door de injectie van calcium.

De ruwijzerontzwaveling is bestudeerd doormiddel van microscopische analyse van ruwijzermonsters die zijn genomen tijdens meerdere behandelingen. Ook is de toplaag van het bad, waar het ruwijzer in contact staat met de slaklaag, bestudeerd. Uit deze analyses volgt dat tijdens de injectie van magnesium magnesiumsulfide deeltjes worden gevormd die enige tijd in het ruwijzer aanwezig blijven, groeien en later uitstijgen. Dit komt overeen met het mechanisme zoals dat door G. Irons and R. Guthrie is voorgesteld op basis van hun experimenten op laboratoriumschaal. Door de verschillen in schaalgrootte speelt de accumulatie van magnesiumsulfide deeltjes in het ruwijzer echter een belangrijke rol in de verklaring van waargenomen zwavelgehalten bij het industriële ontzwavelingsproces. Uit de metingen blijkt verder dat het uitstijgen van de deeltjes naar de slaklaag deels wordt belemmerd door grafiet en Ti(C,N) deeltjes die zich ophopen in de koudere toplaag van het ruwijzerbad. Hierdoor ontstaat een laag met een hoge concentratie MgS-deeltjes die niet wordt opgemerkt maar tot ongewenste verhoging van het zwavelgehalte van het staal na het converterproces kan leiden. Verder blijkt dat de MgS-deeltjes die naar de slaklaag uitstijgen met de co-geïnjecteerde kalk reageren tot MgO en CaS. Om terugloop van zwavel door oxidatie van MgS aan de omgevingslucht te voorkomen, moet kalk daarom altijd in een lichte overmaat worden geïnjecteerd. Tijdens het injectieproces worden ijzerdruppeltjes opgeworpen van de plaats waar de gasbellen het oppervlak bereiken. Deze druppeltjes zakken maar langzaam door de slaklaag en bereiken het ruwijzer niet meer voor het einde van het injectieproces. Op basis hiervan kan worden verklaard hoe het ruwijzerverlies afhangt van de hoeveelheid magnesium die wordt geïnjecteerd, de temperatuur van het ruwijzer en het titaniumgehalte van het ruwijzer. Doordat deze druppeltjes met het verwijderen van de sulfidehoudende slak

worden meegenomen, vormt dit een belangrijke kostenpost in de vorm van ruwijzerverlies.

Op basis van deze bevindingen is een reactormodel van de ruwijzerontzwaveling opgezet. De menging in het ruwijzerbad is beschreven als een ideaal gemengde tankreactor waarbij de verblijftijd van geïnjecteerd magnesium en kalk is beschreven door een generiek model van de bellenpluim. Een belangrijk aspect in het model is dat het totale zwavelgehalte wordt gevormd door de zwavel die is opgelost in het ruwijzer en de zwavel die is gebonden in de MgS-deeltjes die in het ruwijzer zijn gesuspendeerd. Het specifiek oppervlak van de MgS-deeltjes is afgeleid uit de microscopische waarnemingen en het uitstijgen van de MgS-deeltjs is beschreven door een eerste orde snelheidsrelatie. Het voorspelde verloop van de concentraties van zwavel en magnesium tijdens de duur van de injectie komt goed overeen met de metingen die gedaan zijn aan twee behandelingen.

De calciumbehandeling van aluminium rustig staal is uitgebreid bestudeerd door W. Tiekink. Op basis van de door hem uitgevoerde metingen op laboratorium en industriële schaal wordt het staalbad in de staalpan onderverdeeld in twee reactiezones: een pluimzone waarin het staal verzadigd is met calcium en een bulkzone waarin initieel geen calcium aanwezig is. In de pluimzone wordt CaO en CaS op de Al_2O_3-deeltjes afgezet. Geïnduceerd door de bellenpluim ten gevolge van de calciuminjectie stroomt er een circulatiestroom tussen deze zones. Elke zone wordt gemodelleerd door een continu geroerde, ideaal gemengde tankreactor (CISTR). Meegevoerd door deze circulatiestroom worden de deeltjes afwisselend blootgesteld aan hoge en lage calcium activiteit wat uiteindelijk resulteert in een variatie in afmeting en samenstelling van de deeltjes. Dit wordt gemodelleerd door voor elke zone een populatiebalans van de deeltjes op te stellen met daarin termen voor convectie en groei door afzetting van CaO en CaS. De resultaten van het model komen het beste overeen met de waarnemingen als wordt aangenomen dat de oplosbaarheid van calcium in staal 1 ppm bedraagt. Er kan een goede voorspelling van deeltjesgroottes en samenstelling worden gegeven maar de CaS-gehaltes van de deeltjes worden door het model enigszins overschat. Dit wordt verklaard doordat er in werkelijkheid opname is van zuurstof aan het oppervlak van het staal wat in het model nog niet wordt meegenomen.

De uiteindelijke conclusie van dit werk is dat de chemische conversie van het ruwijzer en staal tijdens panmetallurgische injectieprocessen goed kan worden gemodelleerd met een gedetailleerde beschrijving van ontstaan, groei en uitstijgen van de productdeeltjes in combinatie met een relatief eenvoudige macroscopische beschrijving van het stromingsveld in de pan. Dit kan het best worden bereikt door een populatiebalans van de productdeeltjes op te stellen waarin, voor zover van toepassing, termen voor nucleatie, groei, convectie en uitstijging zijn opgenomen. Het stromingsveld in de pan wordt vervolgens gemodelleerd met behulp van drie CISTR's gekoppeld door circulatiestromen van vloeibaar metaal. Deze CISTR's vertegenwoordigen de drie zones die te onderscheiden zijn in een pan die wordt geroerd door middel van een bellenpluim; de pluimzone, de recirculatiezone en de stagnante zone boven de bodem van de pan.

1 Introduction

1.1 The production of carbon steel: teamwork of iron, carbon and oxygen.

Low-alloyed carbon steel is a cheap but strong material that can be produced with a wide range of mechanical properties each suited to a specific application. At the end of the steel products lifecycle, it can be recycled for a high fraction. Therefore low-alloyed carbon steel is an important construction and packaging material and is produced in an increased production volume. The production of carbon steel is primarily concerned with the control and rearrangement of the chemical bounds between the three elements iron, carbon and oxygen:

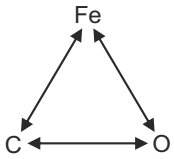

This starts with the raw materials for steelmaking: iron ore, coal and air. Iron ore is composed of different iron oxides, coal is composed of carbon and hydrocarbons and air is a mixture of nitrogen, oxygen, and argon of which primarily oxygen is used. Additional raw materials include limestone, lime, steel scrap, aluminium and alloying metals. In several steps these raw materials are transformed to carbon steel: iron with a concentration of carbon ranging from 0.001 to 0.5 %C. The state of the carbon in the iron matrix and the microstructure of the iron alloy crystals determine properties like strength, hardness and maximum elongation. The desired properties are obtained by a series of mechanical deformations and temperature treatments. As a last stage of the production process steel is often coated to stop further interaction with oxygen from the atmosphere. This coating material can be, for example, zinc, tin, paint or a plastic polymer. This can either be done directly after the final rolling step or as the last stage of the production of the end product.

In the iron-age, which approximately lasted from 1200 BC to 200 BC, iron was produced in a bloomery. Using charcoal as reducing agent and at relatively low temperatures of around 1200 °C a bloom was obtained, a porous mass of sintered iron and slag. By repeatedly heating and hammering slag and other impurities were removed. Subsequently the blacksmith fine tuned the shape and microstructure of the steel by forging it using hammer and anvil, followed by cooling in either air or in an oil or water bath to obtain the desired strength and hardness. Analysis of swords, made more than 1700 years ago, indicates the artisans actively manipulated carbon content and microstructures in the steel to obtain the best toughness of their swords [1],[2].

Figure 1-2 shows a picture of my grandfather Jan Bijlsma working at his forge in Franeker at around 1950. In the coal fire the steel is heated to around 1000-1200 °C. On the anvil

the steel work piece is formed to its desired shape by hammering and in the water reservoir next to the fire the work piece is cooled quickly to obtain its desired final toughness.

Over the years, the steelmaking process has evolved to the modern integrated steel plant capable of producing millions tonnes of steel per year. Figure 1-1 shows the Tata Steel production site at IJmuiden in The Netherlands. The plant is located at the coast and has access to a sea harbour and an international railway network for the supply of iron ore and coal from all over the world and for the export of coils of coated steel strip to customers on the mainland of Europe or overseas.

Figure 1-1. Integrated steel plant. Tata Steel IJmuiden, The Netherlands.

Even though the scale of production has enormously increased, the basis of steelmaking still is the same. The control of Fe-C-O atoms has been brought more and more into perfection to such an extent that the role of other elements, initially being minor, becomes significant as well. The raw materials used for steel production, iron ore, coal and steel scrap, contain significant concentrations of for example manganese, phosphorus, silicon, sulphur, titanium and vanadium. These elements all affect the production process and the quality of the steel end-product. For example, trace elements, otherwise not important, can have a detrimental effect on the solidification of liquid steel in continuous casters as described by Santillana.[6] An overview of the influence of various elements on the production and mechanical properties of steel is given in Figure 1-3 set-up by T. Laux[5]. This indicates it can be quite a task to obtain the desired properties of the end product.

Figure 1-2. B.C. Epker, Pake's Forge, 2015, Linocut, 19 x 15 cm.

	○ extremely undesired																											
	H	B	C	N	O	Al	Si	P	S	Ca	Ti	V	Cr	Mn	Co	Ni	Cu	As	Se	Zr	Nb	Mo	Sn	Sb	Te	Ce	W	Pb	Bi
for process control			●		●	●	●			●	●			●						●						●			
for alloying		●	●	●		●	●	●	●		●	●	●	●	●	●	●		●	●	●	●			●		●	●	●
as tramp element	○	●	●	○	○		●	○	○				●	●	●	●	○	○		●	●	●	○	○			●	●	●
Steel properties	Effects: Improvement, direct/indirect: ↑/↑ Deterioration, direct/indirect: ↓/↓																											
yield strength			↑	↑		↑	↑	↑			↑	↑	↑	↑	↑	↑	↑			↑	↑	↑	↑				↑	
toughness	↓	↑	↓	↓	↓	↑	↓	↓	↓	↑	↑	↑		↑		↑↓	↓	↓		↑	↓↑	↑	↓	↓		↑	↓		
hardenability		↑	↑			↑↓	↑				↓	↑↓	↑	↑	↓	↑	↑			↓	↑↓	↑					↑		
hot forming properties		↓	↑↓	↓	↓	↓			↓	↑			↓	↑	↓	↓	↓	↓			↓	↓	↓	↓	↓	↑	↓	↓	↓
cold forming properties	↓		↓	↓	↓		↓	↓	↓		↓	↓	↓				↓	↓		↓	↓	↓	↓	↓					↓
machinability					↓	↓	↓	↑	↑	↑	↓	↓	↓	↑	↓				↑	↓	↓	↓		↑	↑		↓	↑	↑

Figure 1-3. Influence of various elements in steel after Laux.[5]

In the next section, the production route of the integrated steel plant is described and the role of ladle treatments to control the concentrations of these elements is highlighted.

1.2 The role of ladle treatments in the production of steel strip

Figure 1-4 schematically shows the production route of steel strip at Tata Steel IJmuiden. After agglomeration of the iron ore to pellets and sinter and conversion of coal to coke, these feedstock materials are charged to the blast-furnaces. With the reduction process hot metal is produced; liquid iron with dissolved carbon, manganese, phosphorus, silicon, titanium and vanadium. Hot metal is charged into the oxygen steelmaking converter where these elements are removed by oxidation until the required concentrations are achieved. To absorb the heat generated by the oxidation reactions, steel scrap is charged in addition to hot metal up to almost 30% of the hot metal mass. Due to the similar chemical properties of sulphur and oxygen, sulphur is not removed under oxidising conditions and additional treatments, under reducing conditions, are required to achieve the desired sulphur levels. Besides sulphur removal, other secondary metallurgical treatments are applied to obtain the steel with the desired chemical composition; examples are alloying, removal of other impurities and additional carbon removal. When the liquid steel has reached its specified chemical composition, it is cast in the continuous casters. With subsequent hot rolling, cold rolling, reheating and annealing the final dimensions, surface properties and microstructure of the steel strip are obtained.

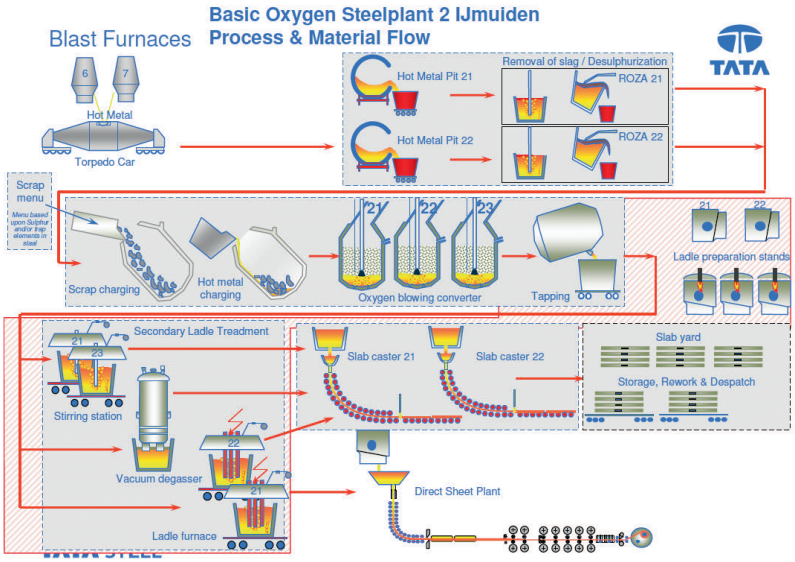

Figure 1-4. Production route of steel strip and slab at Tata Steel BOS No.2 IJmuiden.

Whereas the blast furnace and the slab casters are (semi) continuous processes, the converter process is a batch process. In the steel industry a batch is called a heat. The heat size is determined by the volume of the steel transfer ladles. At Tata Steel BOS No.2 in IJmuiden, in the following referred to as BOS No.2, the average heat size is 330 t (tonnes). In hot metal desulphurisation and in the secondary metallurgy the iron and steel transfer ladles are used as the reaction vessel. These operations therefore are called ladle treatments. Examples of ladle treatments are:[3] [4]

- Desulphurisation of hot metal by injection of desulphurising agents, followed by removal of the sulphide containing slag layer.
- Dephosphorisation of hot metal by injection of lime and iron oxide, followed by removal of the phosphate containing slag layer.
- Decarburisation and chemical heating of steel by means of vacuum treatment.
- Electrical heating of steel in a ladle arc furnace to control the temperature and slag-steel reactions.
- Alloying of steel with, for example manganese, silicon, titanium, boron, niobium or vanadium by injection of these alloying metals followed by homogenisation by gas stirring.
- Deoxidation of steel by injection of aluminium or silicon, followed by flotation of the oxides to the slag layer.
- Desulphurisation of deoxidised steel by injection of desulphurising agents or by applying a sulphur absorbing slag layer on the steel and induce stirring by gas injection.

- Modification of residual alumina oxides in deoxidised steel to calcium aluminates by injection of metallic calcium in the steel.

These ladle treatments often comprise the injection of one or more reagents into the liquid hot metal or steel. Two examples of ladle injection processes at BOS No.2, are described in further detail in the following sections: desulphurisation of hot metal and the calcium-treatment of liquid steel.

1.3 Hot metal desulphurisation

The sulphur content of hot metal tapped from the blast furnaces ranges from 150 to 800 ppm (parts per million by mass). In this thesis, concentrations are given as mass fractions unless otherwise noted. To meet the specifications of the steel end-product and to improve the performance of the calcium treatment of the liquid steel, the hot metal sulphur content has to be reduced to, in some cases as low as 20 ppm. Since sulphur removal is most efficient at low oxygen activity in the liquid iron, hot metal is desulphurised before it is charged into the oxygen steelmaking converter, in which the oxygen activity is high. Figure 1-5 shows the distributions of the sulphur contents in hot metal tapped from the blast furnaces, in hot metal after desulphurisation and in the steel end-products for the production at BOS No.2 in the period January 2013 – June 2015.

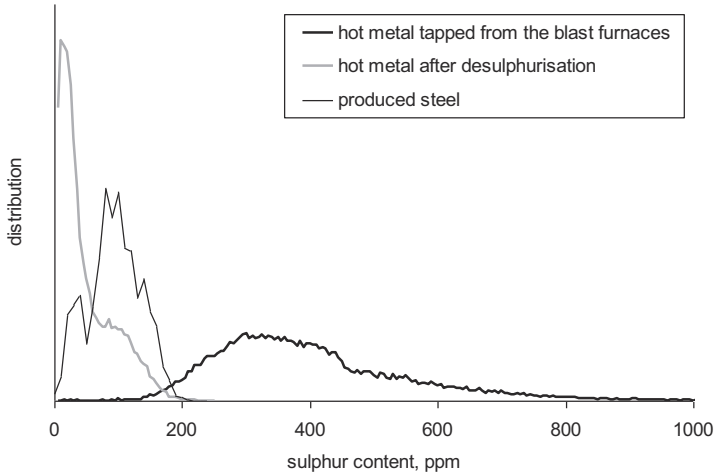

Figure 1-5. Distribution sulphur contents in hot metal and steel at BOS No2.

The average sulphur content of the steel tapped from the converter is 70 ppm higher than the hot metal charged to the converter. This is due to the input of sulphur from scrap charged to the converter. Figure 1-6 schematically shows the process as performed in the hot metal transfer ladles.

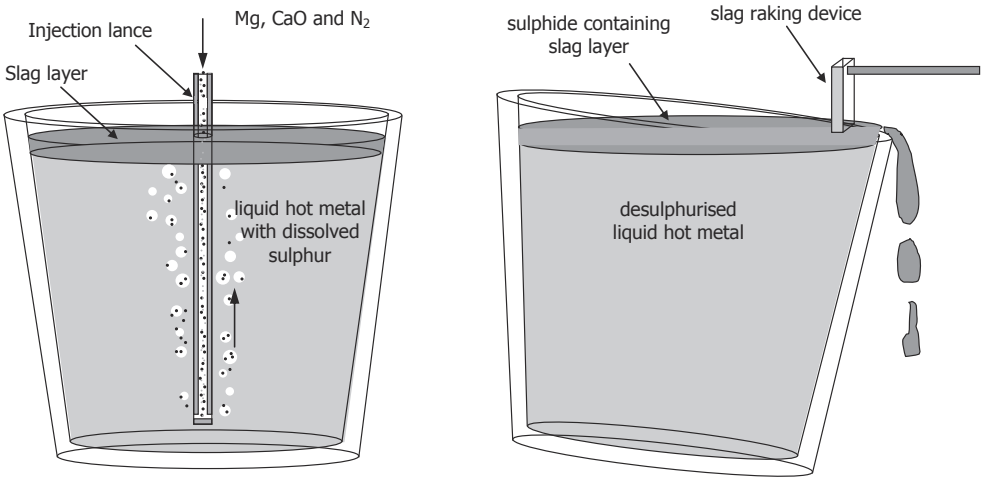

Injection of magnesium and lime Removal of slag by raking

Figure 1-6. Schematic of the hot metal desulphurisation process at BOS No.2.

Lime powder and metallic magnesium granules are injected deeply into the liquid hot metal bath using nitrogen as a carrier gas. The resulting bubble plume induces mixing of the hot metal bath. The injection and rapid vaporisation of the magnesium results in shaking of the hot metal ladle which weighs up to 450 t in total. The injected lime and magnesium react with dissolved sulphur. The basic net desulphurisation reactions are given by equations (1) to (4) where the square brackets indicate dissolved components:

$$Mg_{gas} + [S] = MgS_{solid} \quad (1)$$

$$CaO_{solid} + [S] = CaS_{solid} + [O] \quad (2)$$

$$Mg_{gas} + [O] = MgO_{solid} \quad (3)$$

$$[Si] + 2\,[O] = SiO_{2\ solid} \quad (4)$$

When magnesium and lime are injected simultaneously, reaction (3) is preferred over (4) due to the higher affinity of magnesium to oxygen. The reaction products and un-reacted reagents float to the surface and are absorbed into the slag layer covering the hot metal. This slag layer initially is formed by blast furnace slag carry over. After the proper amounts of lime and magnesium have been injected, the ladle is tilted till the hot metal is at level with the ladle lip. The slag layer is then skimmed from the hot metal by raking the slag over the lip. When all slag has been removed, the hot metal is ready to be transferred to the oxygen steelmaking converter. It is important that the slag is completely removed because during the oxygen blow sulphides present in the slag will be oxidized and sulphur will partly revert to the liquid steel again.

The costs of the raw materials used for the desulphurisation treatment amount to around 1 € per tonne liquid steel produced. In addition, the hot metal loss accompanied with the removal of the slag layer can amount to up to 1% of the hot metal mass which is a significant loss to the overall productivity of the steel plant.

1.4 Calcium treatment of liquid steel

After the converter process several secondary metallurgy treatments can be applied as described in 1.2. For almost all steel grades, the final step prior to continuous casting is deoxidation with, in most cases, aluminium. Production of high-quality deep drawing steel by continuous casting requires strict control of the final aluminium content. Residual Al_2O_3 particles that remain suspended in the steel after deoxidation and alloying have the tendency to clog the refractory nozzles in the continuous casters. This causes uncontrolled variations in the casting speed that lead to reduced properties of the steel strip and loss of productivity. To reduce these problems calcium treatment is applied in BOS No.2 to the major part of the ladle furnace heats, one third of the total production. At the final stage of the ladle furnace treatment metallic calcium is injected into the liquid steel. This leads to the conversion of solid Al_2O_3 particles into liquid calcium aluminates (CA) that do not clog and are entrained with the liquid steel flow. Dispersed in the steel slab they do not harm the properties of the steel end-product. Figure 1-7 schematically shows the process as performed in the steel transfer ladles at BOS No.2.

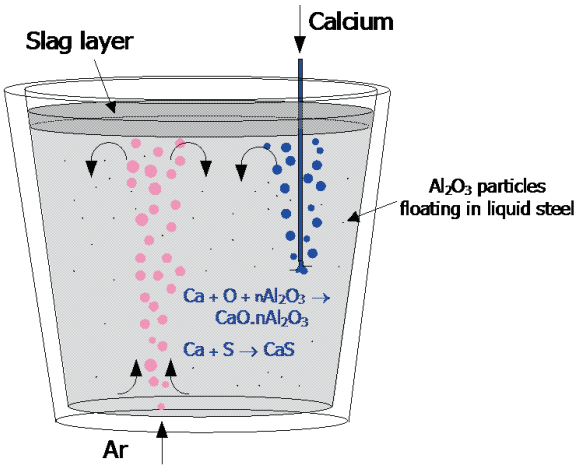

Figure 1-7. Schematic of the calcium treatment of aluminium killed steel at BOS No.2.

Metallic calcium is added to the liquid steel by injection of a cored steel wire while the steel bath is stirred simultaneously by gas injection through porous plugs located at the bottom of the ladle. At steelmaking temperatures, the vapour pressure of calcium is 1.9 bar. At sufficient dept, where the ferrostatic pressure is greater than 2 bar, the cored wire bursts open and calcium is released as liquid droplets. While floating to the surface, the ferrostatic pressure drops and the droplets vaporise resulting in a bubble plume.

The net chemical reaction is given by:

$$nCa_{vap} + n[O] + Al_2O_{3,s} = nCaO.Al_2O_3 \quad (5)$$

The success of the calcium treatment is determined by the control over the chemical composition of the calcium aluminates. The composition of the formed $nCaO.Al_2O_3$ must be such that it is liquid at the solidification temperature of the steel cast. When the oxygen activity has dropped sufficiently and sulphur activity is high enough, calcium sulphide is formed:

$$Ca_{vap} + [S] = CaS_s \quad (6)$$

Calcium sulphide can promote clogging and therefore its formation must be suppressed. Due to the vaporisation and low solubility of calcium in liquid steel the yield of injected calcium is low in practice. Furthermore, addition of calcium in excess to steel leads to increased wear of the alumina refractory ladle lining and thus must be avoided. On average, the consumption of CaFe-wire accounts for slightly more than 1 € per tonne liquid steel.

1.5 Scope and outline of this thesis

These two examples illustrate the importance of ladle injection processes to the control of the quality and costs of the steel end product:

To ensure good control over the casting process, the continuous casters require a timely delivery of steel ladles at the required temperature. No delay in the supply of liquid steel thus is permitted and therefore a corrective treatment often is not possible or leads to reduction of productivity and product quality.

Both processes use expensive reagents in the form of alkaline earth metals. Due to their stable oxides a lot of energy is required to obtain them in metallic form. To make things worse, the conversion of these reagents in the ladle processes is unsatisfactory with estimated efficiencies between 20 to 50%.

For these reasons the ladle injection processes are studied to improve their performance. From empirical relations and statistical analysis of production data process models are developed that for example predict the required amounts of reagents or alloys to be injected to obtain the desired specifications. To better suit the demands of the market, metallurgists are continuously developing new steel grades with higher strength, ductility, formability and surface properties. The production of these new grades requires operation of the existing treatments outside their familiar range of application or even investments in completely new ladle treatments. For example, for hydrogen induced crack resistant (HIC) steels with maximum sulphur content of 10 ppm a new production method needs to be developed. With this, the problem arises that process models based on empirical relations and statistical analysis fall short in making predictions outside their known window of operation. The development of new production routes thus requires extensive and expensive experimenting increasing the development time for a new product.

With models based on first principles the process is divided into the relevant physical and chemical sub-processes, described separately and joined to a model describing the complete process. This has the following advantages over empirical and statistical relations: in the first place, the research required for the modelling can be divided in separate steps that can be studied independently, giving better direction to research activities. Furthermore these models can give better predictions for the processes out of their window of operation and be helpful in the development of new production procedures or even production processes. This is promoted by the increase in computational power which has led to improved measurement and data analysis techniques and more solution power for increasingly demanding mathematical models.

The goal of the present work is to develop mechanistic models of the desulphurisation of hot metal and the calcium treatment of aluminium killed steel that help improving these processes and, from this work, give direction to future research into the modelling of other injection processes in ladle metallurgy as well.

Chapter 2 describes the analysis of hot metal samples taken during the desulphurisation heats at BOS No.2. From these data, knowledge of the formation of sulphides and their separation from the hot metal is obtained. Chapter 3 covers the absorption of the sulphides in the slag layer. This is studied by analysis of samples taken from the top layer of the hot metal bath before and after slag removal. Using the knowledge gained with these studies, in Chapter 4 a process model is developed to predict the hot metal sulphur content during the injection process. Chapter 5 is concerned with the calcium treatment of liquid steel. This process has been studied in detail by Wouter Tiekink[7] at BOS No.2. Based on his results, a process model is derived describing the transition of Al_2O_3 particles to calcium aluminates during the injection of calcium. Finally, in Chapter 6, a cross section of these two studies will be sought to obtain a general vision on the analysis and modelling of ladle treatments.

1.6 References

[1] W. Nicodemi, C. Mapelli, R. Venturini and R. Riva. Metallurgical investigations on two sword blades of 7th and 3rd century B.C. found in Central Italy, ISIJ Int. 45 (2005) 1358-1367.

[2] C. Mapelli, W. Nicodemi and R. Riva Carlo. Microstructural investigation on a medieval sword produced in 12th century A.D., ISIJ Int. 47 (2007) 1050-1057.

[3] G. Stolte. Secondary Metallurgy, Verlag Stahleisen GmbH, Düsseldorf (Germany), 2002.

[4] B. Deo and R. Boom. Fundamentals of steelmaking metallurgy. Prentice Hall Int. (UK), 1993. p 154-159.

[5] T. Laux. Influence of tramp elements on the properties of structural sections and their weldability, Appendix 4 from Effects of tramp elements in flat and long products, Technical Steel Research, European Commission, 1995, p 61-74.

[6] M.B. Santillana. Thermo-mechanical properties and cracking during solidification of thin slab cast steel, PhD-thesis, Delft University of Technology, Delft (Netherlands), 2013.

[7] W. Tiekink. Al_2O_3 in steel and its transformation with calcium, PhD-thesis, Delft University of Technology, Delft (Netherlands), 2012.

2 Hot metal desulphurisation reactions

2.1 Introduction

The hot metal desulphurisation process as performed at BOS No.2 is described in section 1.3. The first step involves the binding of dissolved sulphur and absorption into the slag layer by injection of magnesium and lime to remove sulphur from hot metal as sulphide. The kinetics of the reactions have been studied by Irons and Guthrie [1] [2]. With laboratory scale experiments pure magnesium vapour, or magnesium vapour diluted with argon carrier gas, was injected into 60 kg of carbon saturated hot metal heated to 1250 °C in an induction furnace. From the analysis of the observed changes in concentration and mass transfer rates of magnesium from and sulphur to the bubbles, it was concluded that only a maximum of one tenth of the observed desulphurisation rate could occur by diffusion of sulphur to the bubble interface. Their proposed reaction mechanism is shown schematically in Figure 2-1.

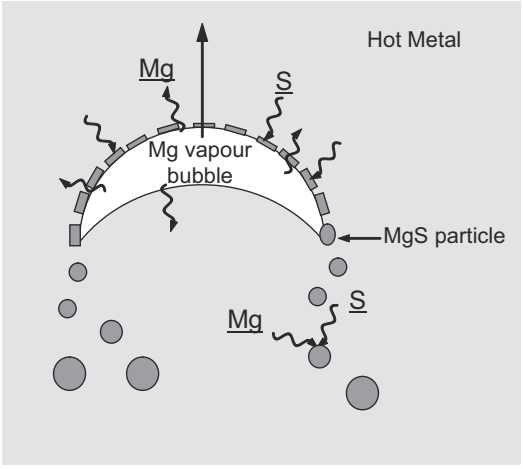

Figure 2-1. Mechanism for hot metal desulphurisation by magnesium injection as proposed by Irons and Guthrie [2].

After injection of the magnesium in the hot metal bath, the vapour bubble floats upwards. Sulphur dissolved in hot metal reacts with magnesium vapour on the vapour/hot metal interface to form MgS. Continuous hydrodynamic shear on the bubble surface prevents blockage by MgS at the bubble surface and magnesium is free to dissolve into the iron. This magnesium reacts with dissolved sulphur on seeds, probably portions of the interfacial product layer stripped from the bubbles. Because of their small size, the specific surface area and mass transfer coefficients are high. This way precipitation of MgS on seeds in the melt forms the dominant factor for the rate of desulphurisation.

With optical and scanning electron microscopic examination of samples taken from different melts, very few of these MgS inclusions could be detected. On one sample surface only one MgS particle with a diameter of 1.5µm was present on a surface of 15 mm². From this the MgS content was estimated to be of the order of 0.5 ppm.

Yang et al.[3]-[8] performed experiments with injecting in-situ produced magnesium vapour in hot metal as published in a series of papers. In a two hours period, magnesium vapour was generated and injected into a hot metal bath of 350 gram[4]. During injection black smoke was escaping from the hot metal. Based on their results, they conclude that the main desulphurisation site is the bubble surface. In later experiments carried out on a larger scale, by Mukawa et al.[9], magnesium was injected into a 30 kg hot metal bath during 20 to 60 minutes. The relation between magnesium and sulphur content indicates that during the injection process, the concentrations are above the solubility product. In the later stage of the process equilibrium is attained. With optimised injection conditions, 6 exit hole injector and optimised argon carrier gas flow rate, a desulphurisation efficiency of 74 % was attained. Again, assuming that the desulphurisation takes place only on the bubble surface the predicted change of sulphur concentration agreed well with the measurements.

Recently Lindström et al.[10] performed laboratory scale measurements to study the kinetics of hot metal desulphurisation. Under well defined conditions, 0.42 grams of magnesium was injected into hot metal samples of 250 grams. After predetermined reaction times, the samples were completely quenched for analysis. Clusters of MgO-MgS, approximately 150 µm in size, were usually found close to the upper surface of the hot metal bath. No pure MgO particles and only a few pure MgS particles with small amounts of MgO were occasionally found. Based on this it was concluded that MgS is not formed by homogenous nucleation but by precipitation on MgO particles. These MgO particles could originate from the approximately 2 µm thick oxide layer covering the magnesium granules. With the experiments a low overall conversion of magnesium is observed. This leads to the conclusion that the magnesium only slowly dissolves in hot metal. After co-injection of magnesium and lime, CaO, CaS and MgS were found in co-existence. This leads to their conclusion that CaO particles act as nucleation for MgS formation as well.

To compare the results of fore mentioned studies on laboratory scale with the process in the steel plant, the formation of reaction products and subsequent flotation to the slag layer has been studied by analysis of hot metal samples taken at various stages during the injection process. This is described in the following sections.

This work has partly been presented at SCANMET III, the 3rd International Conference on Process Development in Iron and Steelmaking in Luleå, Sweden, 8-11 June 2008[11].

2.2 Microscopic analysis

2.2.1 Initial assessment of reaction products

The study started using the regular hot metal samples from various heats, taken for quality and process control in the steel plant, both before and after the injection process. After preparation the samples were studied at the Tata Steel Ceramic Research Centre with both optical microscopy and scanning electron microscopy (SEM) equipped with energy dispersive spectroscopy (EDS).

Table 2-1 shows the properties of the heat of which hot metal samples have been analysed.

Table 2-1. Sampled heat data.

		Initial	Final
Sulphur content	(wt%)	0.031	0.0023
Titanium content	(wt%)	0.143	0.140
Temperature	(°C)	1378	1363
Hot metal mass	(t)	263.3	
CaO injected	(kg)		738
Mg injected	(kg)		145

The measurement details are described below:

Sampling: Samples were taken from the hot metal bath from a depth of 60 cm below the surface. Figure 2-2 schematically shows the cross section of a hot metal sample with the plane of analysis. The circular marking on the top indicates the upper side of the sample. The marking on the left side indicates the entrance of the sample holder. In this plane all the effects of floating or filling on the distribution of inclusions should appear. In general it is found that gas bubbles, when present, accumulate in the upper part of the sample. In the centre part of the sample graphite segregates are observable to the naked eye.

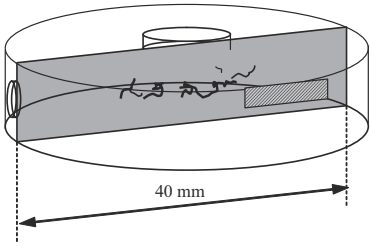

Figure 2-2. Plane of analysis of hot metal samples.

Initial microscopic observations proved that smaller inclusions, less than 50 µm, are equally distributed over the cross section. To obtain an indication of the occurrence of particles and phases, element mappings where done. To avoid interference by the graphite segregates, the mappings were done on the shaded area in Figure 2-2.

Resolution: The scan area is 100 x 100 µm and this is divided in 128 x 128 points, so the resolution of the scan is 0.78 µm. Each point is scanned for 0.1 sec. This is slightly too coarse considering the small size of the inclusions, but otherwise the measurements will take too much time.

Carbon: The concentration of carbon in the sample cannot properly be measured because a thin layer of carbon is deposited on the sample to improve the conductivity of the surface. The first mapping was performed on a non-carbon-deposited sample and failed because of loading of the sample by the prolonged electron radiation causing the electrons to be repelled from the surface.

Nitrogen: Nitrogen cannot be measured accurately with EDS and therefore nitrogen is measured using wavelength dispersive spectroscopy. With the interpretation of the results it may be noted that the k-band signal of N is close to the L-band signal of Ti and the presence of Ti can therefore affect the results for N.

Results

Figure 2-4 shows SEM backscatter images of the analysed areas together with combined EDS mappings of Mn, N, S and Ti. The colours of the elements combine as shown in Figure 2-3.

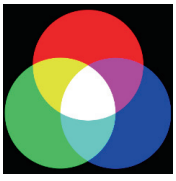

Figure 2-3. Additive combination of colours in the EDS element mappings.

Additive combination of the individual elements shows the simultaneous presence of elements giving a qualitative indication of the chemical compounds. If, for example, manganese and sulphur are both present on a certain spot, this indicates the presence of manganese sulphide. Since it is not possible to discriminate between pure titanium nitride or titanium carbonitride, spots of titanium only are considered to be titanium carbide.

Before desulphurisation:

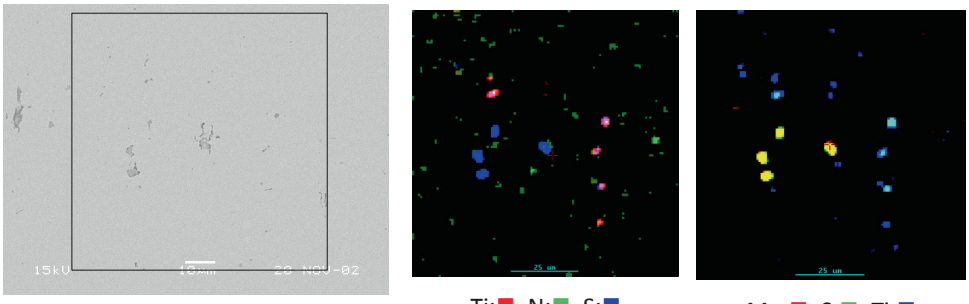

After desulphurisation:

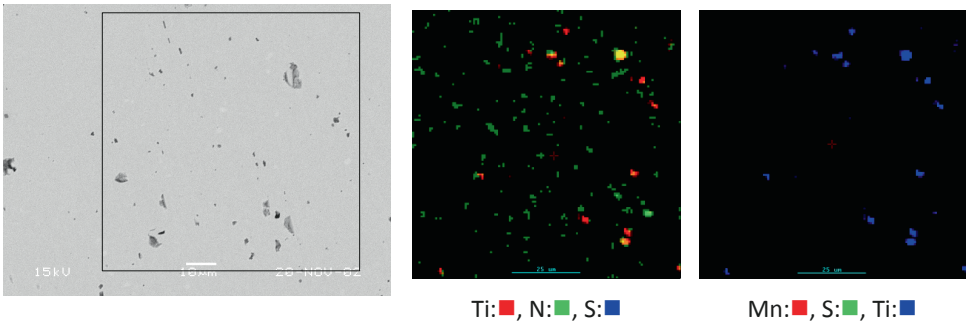

Figure 2-4. SEM BS image and EDS element mappings on samples taken before and after desulphurisation.

The figures indicate the presence of particles with sizes in the order of micrometers. In the sample taken before desulphurisation, particles composed of manganese sulphide, titanium sulphide, titanium nitride and titanium carbide are found. After desulphurisation only titanium carbide and titanium nitride particles are found. Manganese and titanium sulphides are formed with the solidification of the sample. After desulphurisation the sulphur concentration has lowered to such extent that these sulphides are not formed anymore.

The presence of titanium carbonitride is explained by the following. To repair the refractory lining of the blast furnace, ilmenite ores, containing TiO_2, are added to the blast furnace burden. This results in an enrichment of the titanium content of the hot metal. With the iron ore used at the IJmuiden site in the period of sampling the titanium content of hot metal is around 0.056 wt% without addition of ilmenite. In these samples 0.140 wt% is measured. Li et al.[12] have studied the formation of Ti(C,N) from hot metal and have derived the accompanying thermodynamics. At hot metal temperatures around 1380 °C and a partial pressure of nitrogen of 1 atm the minimum titanium concentration to form titanium carbonitride ranges between 0.025 and 0.07 wt%. In hot metal desulphurisation nitrogen is used as carrier gas. The partial pressure of nitrogen in the

bubble plume thus varies between roughly 3 atm at the depth of injection to 1 atm approaching the bath surface. Already under average hot metal conditions Ti(C,N) is a stable phase. With the cooling of the hot metal sample, the solubility of Ti(C,N) is further lowered and more will form.

2.2.2 Individual particles

In addition to element mappings, covering a larger sample surface, individual particles were studied in further detail. Figure 2-5 shows the surface of a hot metal sample taken before desulphurisation at medium magnification. For a part of the particles, the composition is measured and indicated in the figure.

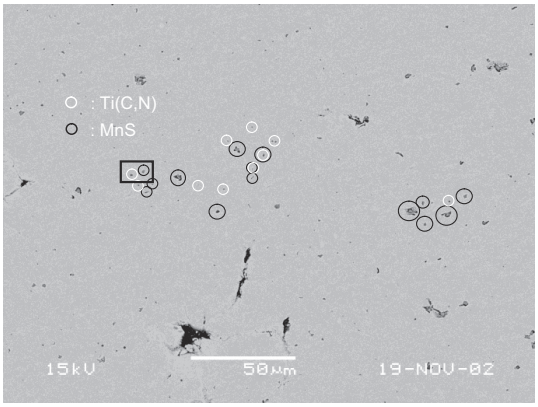

Figure 2-5. Ti(C,N) and MnS particles in a hot metal sample taken before desulphurisation. (SEM BS image).

Figure 2-6 shows a close-up of the region in Figure 2-5 indicated by the black rectangle. The Ti(C,N) particle seems to be composed of smaller, square parts. This coincides with the observations of Li et al.[12] EDS analysis of a number of Ti(C,N) particles shows that often vanadium and niobium are dissolved in the Ti(C,N) phase, effectively forming the solid solution (Ti,V,Nb)(C,N).

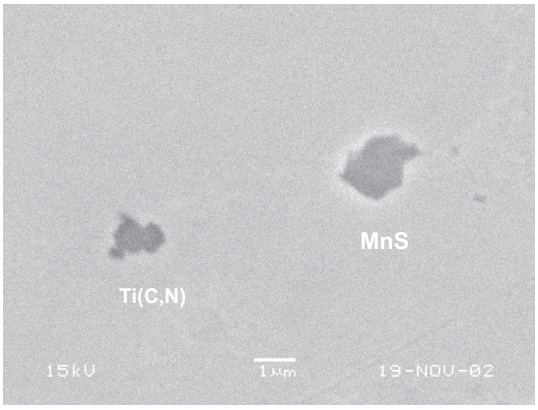

Figure 2-6. Ti(C,N) and MnS particles in a hot metal sample taken before desulphurisation. (SEM-BS image).

Figure 2-7 shows graphite segregates in samples taken before and after desulphurisation from the same heat. A clear difference in shape most likely results from the injection of magnesium. From iron foundry practices it is known that nodular cast iron is obtained after a sufficient amount of magnesium is added.[13]

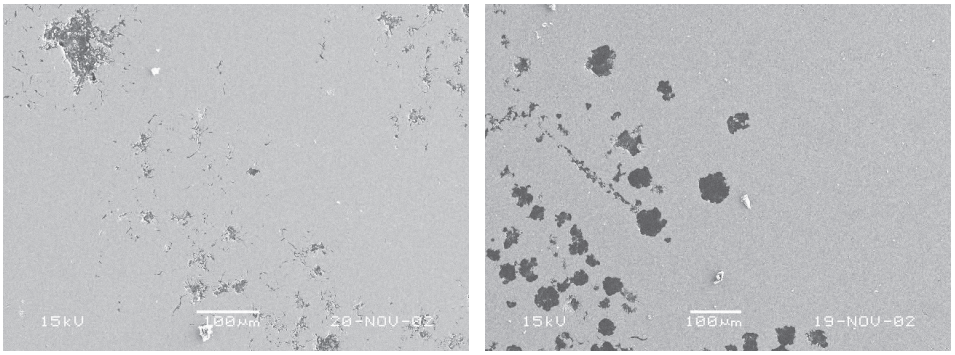

Figure 2-7. Graphite segregates in hot metal samples: left: laminar graphite before desulphurisation, right: nodular graphite after desulphurisation. (SEM-BS images).

Figure 2-8 shows an example of a cluster of two phases as frequently found in samples taken directly at the end of magnesium injection. The element mappings of the most abundant elements indicate it is composed of MgS surrounded by some smaller parts of Ti(C,N) enriched with vanadium.

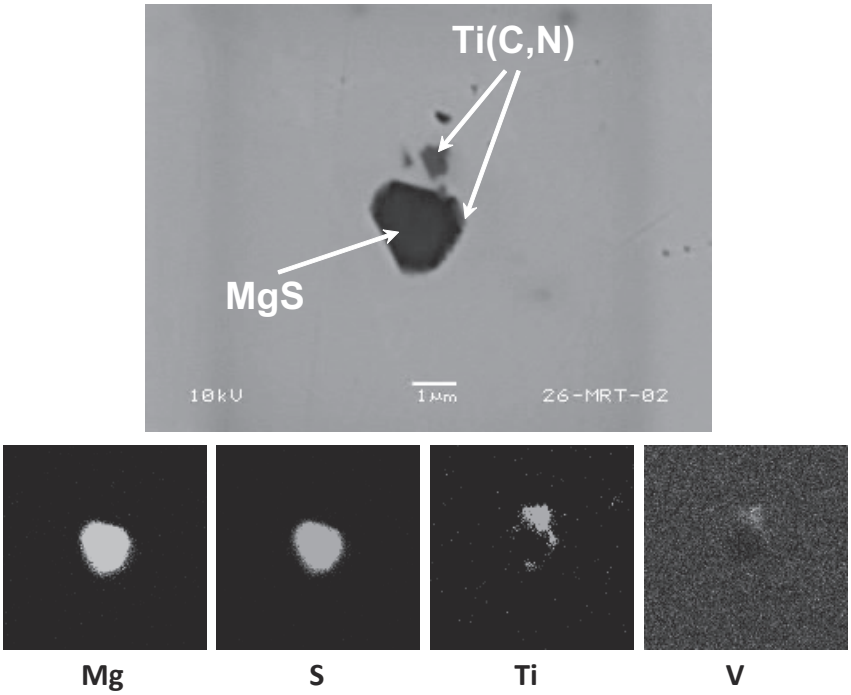

Figure 2-8. MgS-Ti(C,N) particle in a hot metal sample taken after injection of magnesium. (SEM-BS/EDS images).

Figure 2-9 shows another particle found at the same location. The EDS point measurement shows it is composed of MgO and MgS. The element mappings indicate that the MgS phase is enriched with manganese. These MgO particles have not been found in hot metal samples taken after finishing the desulphurisation treatment, thus including post-injection with CaO and slag removal.

Finally, Figure 2-10 shows an example of a cluster of phases. EDS spot analysis indicates that oxygen is also present. In this combination of elements oxygen most likely is bound as MgO. Furthermore manganese is simultaneously present with magnesium and sulphur. MgS and MnS form a completely miscible solid solution (Mg,Mn)S above 500 °C of which the melting point is above 1100 °C [14]. Compared to the size of the particle, the resolution of the EDS measurement is too low to determine whether MnS is deposited on MgS as a solidification product or is homogeneously distributed in the MgS phase.

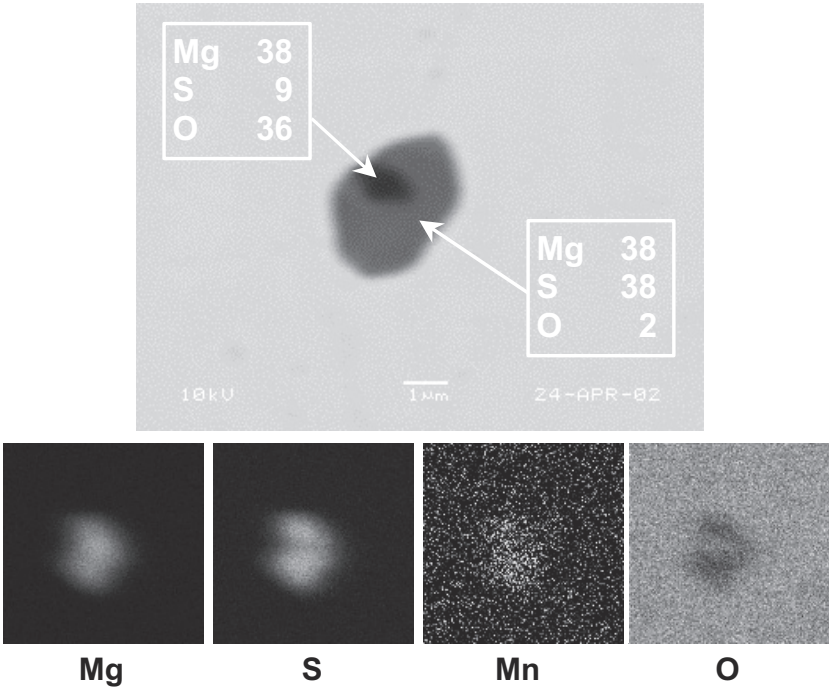

Figure 2-9. MgS-MgO particle in hot metal sample taken during desulphurisation. (SEM-BS/EDS images).

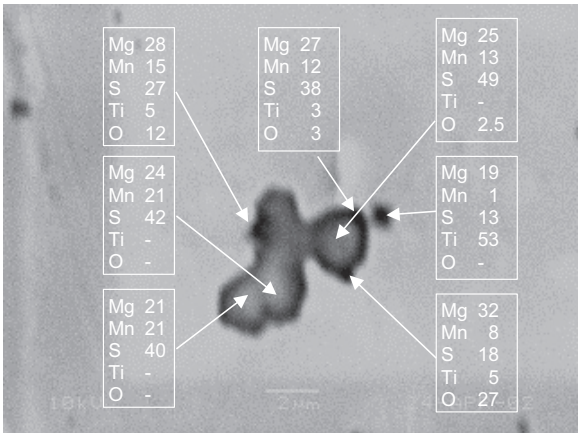

Figure 2-10. Cluster of particles in hot metal after injection of magnesium. (SEM-BS/spot EDS).

2.2.3 Discussion

MgS

MgS particles, with sizes ranging from 0.5 to 4 µm, are found in high concentrations. Irons and Guthrie[1] [2] found one MgS particle only. Most likely this is due to the differences in scale as with the laboratory scale trials, magnesium was injected for 60 minutes in a 60 kg induction furnace. In such a furnace the complete melt is stirred by the induction currents. MgS particles thus are produced at a slow rate but are removed at a high rate. Retention of MgS particles in the melt thus is low. With the industrial process, magnesium is injected over 6 minutes in a 300 t ladle stirred by a bubble plume. The hot metal bath is not stirred by induction currents and MgS particles are removed by the bubble plume only. MgS particles are thus produced at a high rate but are removed at a low rate. Under these conditions, considerable accumulation of MgS particles in the hot metal can be expected.

MgS - MgO

Comparable to the reaction products found by Lindström et al.[10], particles and clusters of particles composed of MgO-MgS are found as well. The particles, however, are smaller, 2-8 µm like in Figure 2-10, versus 150 µm. The small size of the MgO fraction in Figure 2-9 suggests that it originates from the oxide layer covering the magnesium granules. However, MgO can be the result of reaction (3). The particle in Figure 2-9 however, was the only particle of its type found with these analyses. In contrast with the results reported by Lindström, pure MgS particles are found in high concentration in samples taken directly after magnesium injection. It is possible that MgS particles are formed by the mechanism as described by Irons and Guthrie.

Graphite

Irons and Guthrie suggest graphite could act as a nucleation site for MgS formation. This could not be concluded from the present work. Carbon was not measured with the EDS-spot analysis but can be recognised on the SEM back-scatter images based on the grey scale. Graphite particles were found in high concentrations in the centre of all samples and were larger than the MgS particles, in the range of 10 - 30 µm. MgS particles with a carbon core, however, were not found.

CaO - CaS - SiO_2

During the injection process lime powder is injected simultaneously with magnesium. Particles composed of CaO or CaS were not found in these samples. This could indicate that upon injection lime powder is not absorbed into the hot metal but remain locked in the gas bubbles. As the gas bubbles reach the surface and break up, the lime powder remains floating on the hot metal. Another possibility is that some powder is absorbed into the hot metal but is effectively washed out directly as the plume reaches the surface. The question then remains why CaO/CaS particles are washed out completely whereas MgS particles are entrained with the hot metal from the plume to the bulk volume of the ladle. Particles containing SiO_2, possibly resulting from deoxidation reaction (4) were not observed.

Multiphase particles

A significant fraction of the particles are composed of multiple phases like MgS, MnS and Ti(C,N). Oikawa et al.[15] studied the formation of MnS in steel. During solidification the dispersed particles with high melting temperature, like TiN and Al_2O_3 can act as nucleants for the MnS crystals. Furthermore, they describe the formation of finely dispersed MnS in Ti-killed steel[15],[16]. Figure 2-11 is a schematic representation of the nucleation and growth mechanism of MnS inclusions taking place during solidification. During the cooling process, liquid nuclei of (Ti,Mn)O will be formed first at the solid/liquid interface, Figure 2-11 (a), followed by the nucleation of MnS droplets on the surface of (Ti,Mn)O liquid, Figure 2-11 (b). The MnS droplets so formed will then be entrapped by the solid/liquid interface together with (Ti,Mn)O as shown in Figure 2-11 (c) resulting in the fine dispersion of MnS.

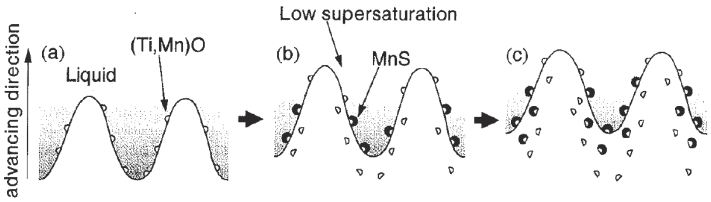

Figure 2-11. Formation of MnS in Ti-killed steel as described by Oikawa[16].

Steel differs from hot metal mainly in temperature and carbon content but this mechanism can explain the multiphase particles found in the hot metal samples in an analogous way.

The lattices of MnS and MgS are similar [14]. MgS present in liquid hot metal before solidification thus can act as nuclei for MnS. Since Mg is a strong deoxidiser, TiO_2 or (Ti,Mn)O are unlikely to form in hot metal after injection. However, as has been explained already, Ti(C,N) will form during solidification of the hot metal sample.

2.3 Analysis of the course of desulphurisation during the injection process

2.3.1 Sampling

In the previous section the reaction and solidification products in hot metal samples taken regularly before and after desulphurisation are described. To obtain a deeper insight in the reactions during the desulphurisation process, series of hot metal samples were taken during two industrial heats at BOS No. 2. The samples were taken with the regular sampling installation at a depth of 60 cm from the surface of the hot metal bath. The first samples were taken just before the start of injection. The final samples were taken after retraction of the injection lance from the hot metal bath. The interval between the samples was determined by the time required for sampling and was limited by the heating of the sampling lances.

The properties of the heats are given in Table 2-2.

Table 2-2. Properties of sampled heats.

		Heat 1	Heat 2
Hot metal mass	(t)	288	283
Hot metal temperature	(°C)	1370	1399
Manganese content	(wt%)	0.42	0.42
Silicon content	(wt%)	0.35	0.44
Titanium content	(wt%)	0.12	0.14
Initial / final sulphur content	(ppm)	200 / 7	229 / 7
CaO injection	(kg)	732	728
Mg injection	(kg)	117	144

2.3.2 Chemical analysis of hot metal samples

Table 2-3 lists the instances of sampling from the start of injection and the measured overall chemical composition. The composition was measured with XRF analysis at the Tata Steel Analytic Department. Since the XRF-analyser is not calibrated to accurately measure the Mg-content, the numbers for Mg-content are indicative.

Figure 2-12 shows the measured sulphur and magnesium concentrations during the injection processes. The injection periods of lime and magnesium are indicated by horizontal bars. At the start of the process only nitrogen is injected and the lance is lowered into the hot metal bath. The injection of lime powder starts when the lance tip has reached a depth of 0.6 m. This way no lime powder is blown into the open air that otherwise would pollute the installation. The injection of magnesium starts when 60 kg of lime has already been injected. This is to ensure that the pneumatic conveying line is not blocked and all oxygen has been flushed out of the lines. The injection of lime powder is continued for a while after all magnesium has been injected. This is to ensure that all magnesium powder has been flushed out of the lines. With these trials, the lime powder injection was prolonged on purpose to asses the effect on the process. Both heats show a similar trend of the sulphur and magnesium concentrations. Initially the decrease in sulphur content is low. Shortly after the magnesium injection has commenced the sulphur concentration decreases at a higher rate and the magnesium concentration slowly increases. In the final stage of the injection process, when the magnesium injection has stopped, the concentration of sulphur further decreases while the magnesium concentration seems to remain constant.

Table 2-3. Time of sampling and measured composition (wt%).

	No.	time	S	Mg	Si	Mn	Ti	V	P	Sn	Mo	Cu	Ni	Cr
Heat 1	1	0:00	0.0203	<0.001	0.354	0.419	0.109	0.048	0.066	<0.001	0.0007	0.006	0.028	0.025
	2	1:06	0.0203	<0.001	0.353	0.421	0.110	0.048	0.066	0.001	<0.001	0.004	0.029	0.025
	3	2:12	0.0184	0.003	0.351	0.422	0.110	0.048	0.070	<0.001	<0.001	0.005	0.041	0.025
	4	3:09	0.0138	0.004	0.348	0.426	0.110	0.049	0.066	<0.001	0.0008	0.006	0.029	0.026
	5	5:27	0.0044	0.005	0.331	0.432	0.109	0.048	0.064	<0.001	0.0005	0.005	0.030	0.026
	6	6:18	0.0035	0.006	0.333	0.427	0.108	0.048	0.069	0.002	0.0006	0.006	0.038	0.026
	7	9:49	0.0007	0.006	0.325	0.421	0.112	0.048	0.064	<0.001	<0.001	0.005	0.024	0.026

	No.	time	S	Mg	Si	Mn	Ti	V	P	Sn	Mo	Cu	Ni	Cr
Heat 2	1	0:00	0.0229	<0.001	0.474	0.421	0.138	0.050	0.066	<0.001	0.0008	0.006	0.029	0.025
	2	1:14	0.0219	0.003	0.468	0.425	0.136	0.050	0.068	<0.001	0.0007	0.006	0.031	0.024
	3	3:14	0.0116	0.005	0.447	0.431	0.136	0.049	0.069	<0.001	0.0008	0.005	0.052	0.025
	4	4:56	0.0056	0.006	0.447	0.429	0.136	0.051	0.065	0.001	0.0007	0.005	0.034	0.025
	5	7:13	0.0026	0.006	0.430	0.432	0.136	0.049	0.063	0.001	0.0008	0.006	0.032	0.026
	6	10:10	0.0007	0.005	0.436	0.431	0.136	0.050	0.064	<0.001	0.0007	0.005	0.029	0.025

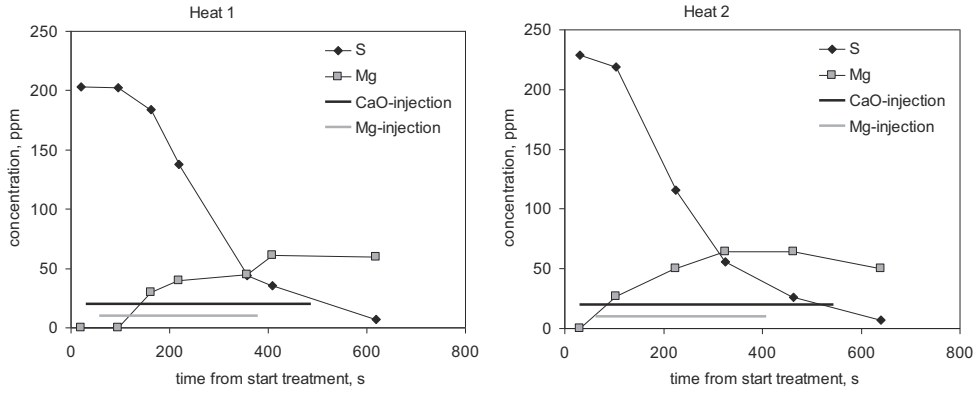

Figure 2-12. Magnesium and sulphur concentrations during the injection process.

2.3.3 Solubility of MgS

An important parameter in the hot metal desulphurisation with magnesium injection is the solubility product of MgS in liquid carbon-saturated iron. This is denoted as P_{MgS} and is expressed as ppm².

$$P_{MgS} = [ppmMg][ppmS] \tag{7}$$

Irons an Guthrie [1] used a value of 180 ppm² at 1250 °C.

Turkdogan[17] gives the following relations for the solubility product:

$$\log K_{MgS} = \log\left(f_{Mg}[wt\%Mg] f_S[wt\%S]\right) = -\frac{17026}{T} + 5.161 \tag{8}$$

With f_{Mg} = 0.22 and f_S = 4.4 at carbon saturation the solubility product of MgS is given by:

$$P_{MgS} = 1.033 \cdot 10^{-\frac{17026}{T}+13.161} \tag{9}$$

Another relation is given by Yang. et al.:[8]

$$P_{MgS} = 10^{0.18-0.11[\%C]_{sat}+11839/T} \cdot e^{\frac{-404070+169.21T}{8.314T}} \tag{10}$$

The following relation can be used for the carbon content at saturation:

$$[\%C]_{sat} = 1.3 + 0.00257 \cdot T(^{o}C) \tag{11}$$

Using the thermo-chemical software package Chemsage, Ender et al.[18] calculated the solubility product involving Thyssen Krupp Steel hot metal conditions. Their result is summarised as:

$$\log P_{MgS} = -14.3 + 0.00679 \cdot T(^{o}C) \tag{12}$$

Figure 2-13 compares the various predictions for the solubility product.

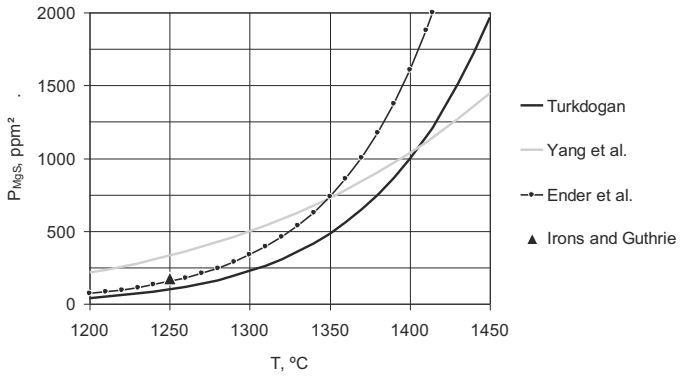

Figure 2-13. Solubility product of MgS in liquid carbon saturated iron.

In practice, differences are small. For example, at 1380 °C and 60 ppm sulphur the accompanying magnesium contents range between 12.5 and 19.6 ppm, see Table 2-4.

Table 2-4. Equilibrium magnesium content in hot metal at 1380 °C and 60 ppm sulphur.

Reference	P_{MgS} (ppm²)	[ppmMg]
Turkdogan[17]	750	12.5
Yang et al. [8]	903	15.0
Ender et al. [18]	1175	19.6

Figure 2-14 shows sulphur versus magnesium concentrations during the injection process for both heats. The arrow indicates the timeline of the process, starting on the x-axis at high sulphur concentration and finishing near the y-axis at low sulphur and high magnesium concentration. The solubility products of MgS for the two heats are shown for comparison as well. The solubility products for the respective hot metal temperatures of Heat 1 and 2 are calculated as 840 and 1040 ppm² using (10).

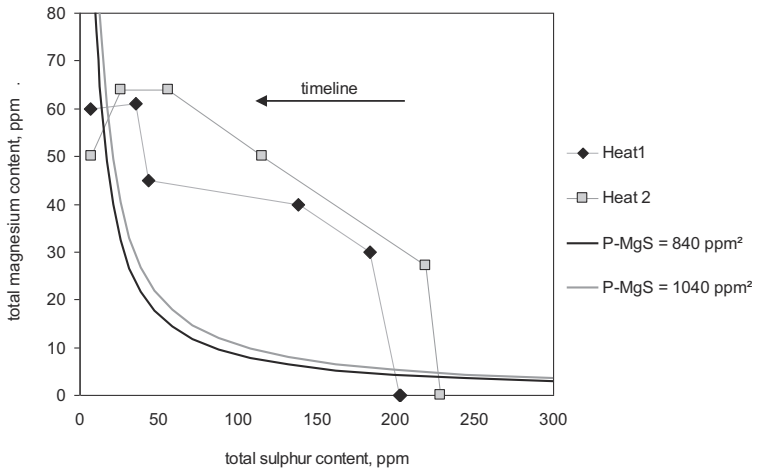

Figure 2-14. Sulphur versus magnesium concentration during the injection process.

The figure indicates that in the second sample, taken right after the start of the magnesium injection, the solubility product is already exceeded. This remains throughout the magnesium injection. With Heat 2 one sample was obtained when the magnesium injection was already over. Also at this time, the solubility product was exceeded. Only in the samples taken after the finalisation of the lime injection, the magnesium and sulphur concentrations are below the solubility product. With their experiments, Mukawe et al.[9] found the same relation between magnesium and sulphur content and the solubility product.

The fact that the magnesium and sulphur concentrations exceed the solubility product can be explained by two mechanisms:

- Reaction rate limitations. Magnesium and sulphur concentrations above the solubility product of MgS form the driving force for the formation of MgS. At the actual hot metal temperatures, 1250 to 1450 °C, local equilibrium is attained quickly. The rate of formation of MgS thus is limited by the dissolution of magnesium, nucleation of MgS seeds and the diffusion of dissolved magnesium and sulphur towards the seeds. This possibility is investigated in Chapter 4.
- Accumulation of MgS. With microscopic observations described in the previous sections MgS particles have been found in the hot metal samples taken during the injection process. After their formation and growth the MgS particles float out of the hot metal bath to the slag layer induced by the gas bubble plume. This requires some process time so during the injection process MgS particles are suspended in the hot metal. With XRF analysis the total concentrations of sulphur and magnesium are measured. This includes dissolved sulphur and magnesium and the constituents of MgS. This is further investigated in section 2.4.

Assuming thermodynamic equilibrium, the concentration of suspended MgS can be derived from the results of XRF analysis as shown in Figure 2-15. The concentrations of the dissolved substances are found by the intersection of the line down from the

measurement point with gradient determined by the stoichiometry of MgS, M_{Mg}/M_S, with the line of the solubility product, which in this example is 800 ppm².

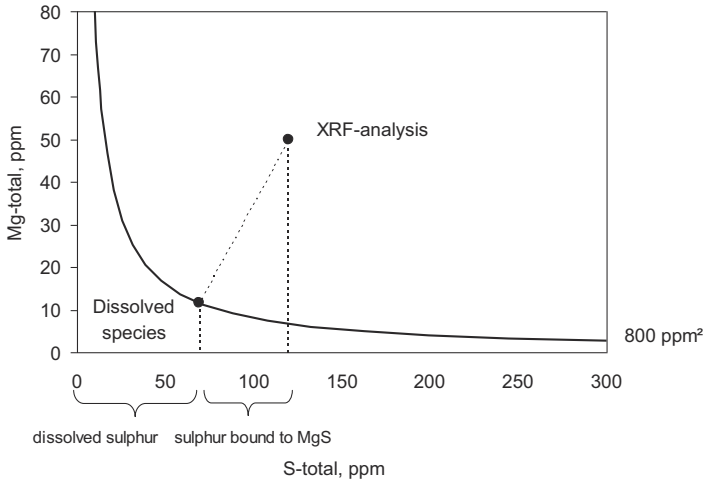

Figure 2-15. Solubility product of MgS.

This intersection is described by the following relation:

$$[ppmS][ppmMg] = P_{MgS} = [S]\left([ppmMg]_{tot} - \frac{M_{Mg}}{M_S}\left([ppmS]_{tot} - [ppmS]\right)\right) \tag{13}$$

which is rewritten to:

$$[ppmS]^2 + \left(\frac{M_S}{M_{Mg}}[ppmMg]_{tot} - [ppmS]_{tot}\right)[ppmS] - \frac{M_S}{M_{Mg}}P_{MgS} = 0 \tag{14}$$

and the concentration of dissolved sulphur follows from:

$$[ppmS] = \frac{[ppmS]_{tot} - \frac{M_S}{M_{Mg}}[ppmMg]_{tot} + \sqrt{\left(\frac{M_S}{M_{Mg}}[ppmMg]_{tot} - [ppmS]_{tot}\right)^2 + 4\frac{M_S}{M_{Mg}}P_{MgS}}}{2} \tag{15}$$

The concentration of dissolved magnesium follows from (7) and the concentration of dispersed MgS from:

$$[ppmMgS] = \frac{M_{MgS}}{M_S}\left([ppmS]_{tot} - [ppmS]\right) \tag{16}$$

It should be noted that [*ppmMg*] and [*ppmS*] refer to the concentrations of the dissolved substances whereas [*ppmMgS*] refers to the concentration of dispersed MgS particles. The MgS contents thus obtained are given in Table 2-5.

Table 2-5. MgS-contents derived from XRF analysis

sample	total concentration		dissolved		bound to MgS			
	S (ppm)	Mg (ppm)	S (ppm)	Mg (ppm)	S (ppm)	Mg (ppm)	MgS (ppm)	P_{MgS} (ppm^2)
Heat 1-1	203	0	203	0	0	0	0	840
Heat 1-2	203	0	203	0	0	0	0	840
Heat 1-3	184	30	152	6	32	24	57	840
Heat 1-4	138	40	97	9	41	31	73	840
Heat 1-5	44	45	26	32	17	13	30	840
Heat 1-6	35	61	18	48	18	13	31	840
Heat 1-7	7	60	7	60	0	0	0	840
Heat 2-1	229	0	229	0	0	0	0	1040
Heat 2-2	219	27	191	5	28	22	50	1040
Heat 2-3	116	50	70	15	46	35	81	1040
Heat 2-4	56	64	25	41	30	23	54	1040
Heat 2-5	26	64	18	58	8	6	14	1040
Heat 2-6	7	50	7	50	0	0	x	1040

Figure 2-16 and Figure 2-17 show calculated MgS contents during the injection. The CaO- and Mg-injection periods are also indicated.

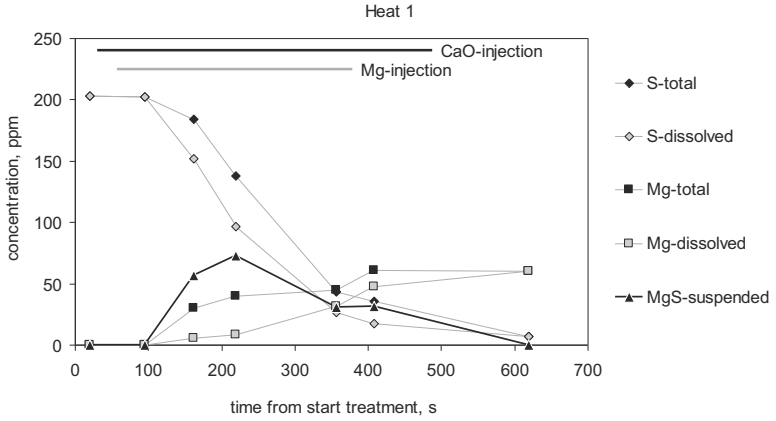

Figure 2-16. Calculated MgS content during the injection process for Heat 1.

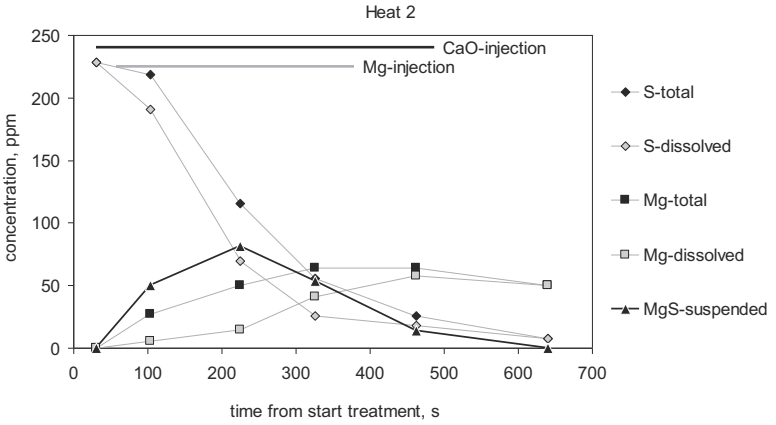

Figure 2-17. Calculated MgS content during the injection process for Heat 2.

Both graphs show a rise in MgS content in the beginning of the process, followed by a decrease half-way the magnesium injection. During the post-injection of lime, the MgS content becomes negligible. Most likely, the particles will only be flushed out during the injection so the final concentrations will be already attained at the end of lime injection.

2.3.4 Magnesium efficiency

During injection of the reagents, both desulphurisation reactions (1) and (2) take place where reaction (2) will be followed by reaction (3). Thus, for every mole of sulphur removed, one mole of either MgS or MgO is formed and one mole of magnesium will be consumed. As the concentration of dissolved sulphur decreases during the injection process, more magnesium will remain dissolved in the hot metal.

The overall efficiency of injected magnesium thus follows from:

$$\eta_{Mg} = \frac{\left(\Delta[ppmS]\frac{M_{Mg}}{M_S} + [ppmMg]\right)\cdot m_{HM}}{m_{Mg,injected}} \cdot 10^{-6} \quad (17)$$

The over-all efficiency of injected magnesium for the two heats calculated using (17) is given in Table 2-6.

Table 2-6. Calculation of over-all magnesium efficiency.

		Heat 1	Heat 2
hot metal mass	(t)	288.6	284.1
initial sulphur concentration	(ppm)	200	229
final sulphur concentration	(ppm)	7	7
final magnesium concentration	(ppm)	60	50
sulphur removed	(kg)	56	63
magnesium bound (to sulphur or oxygen)	(kg)	42	48
magnesium dissolved	(kg)	17	14
magnesium injected	(kg)	117	144
magnesium efficiency	(-)	51%	43%

The results in Table 2-6 indicate approximately half of the injected amount of magnesium is lost. Possible causes for loss of magnesium are:

- Reaction with oxygen from the air in the spout area. As discussed in the next section, the concentration of silicon decreases during the injection process. Most likely this is due to reaction with oxygen from the air at the spout area where hot metal is exposed to the environment. When dissolved silicon is oxidised, this can be expected to happen to dissolved magnesium as well.
- Reaction with the slag layer. The slag layer covering the hot metal bath initially is formed by blast furnace slag carry-over. This contains approximately 33% of SiO_2 that can be reduced by magnesium dissolved in the hot metal bath, see Table 3-4.
- Incomplete dissolution. In the operational practice, bright flames are observed above the spout which indicates burning magnesium vapour. This confirms that magnesium is unable to dissolve completely. This may be due to saturation of hot metal with magnesium or mass transfer limitations. Several references on the solubility of magnesium in hot metal are discussed by Voronova.[19] Values for the maximum solubility at 1385°C and 1 atm are in a wide range of 0.1 to 0.6 wt% or 1000 to 6000 ppm. This is significantly higher than the concentrations measured. The dissolution thus seems limited by mass transfer from the rising bubbles to the hot metal.

A decisive answer could be obtained by accurately measuring the total MgO content of the slag on the hot metal bath after the injection process and the total amount of MgO dust in the off-gas.

2.3.5 Oxidation of silicon

Figure 2-18 shows the same plot as Figure 2-12 with measured silicon contents added. The y-axes are scaled such that the decrease of the silicon content coincides with the decrease of the sulphur content.

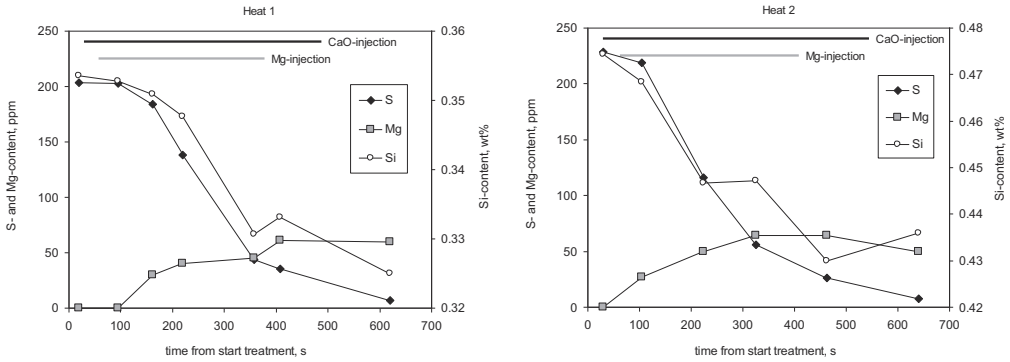

Figure 2-18. Magnesium, silicon and sulphur concentrations during the injection process.

If sulphur reacts only with lime and all oxygen released reacts with silicon according to relations (2) and (4), the decrease in silicon content relative to the decrease in sulphur content would be described by relation (18).

$$\frac{\Delta[Si]}{\Delta[S]} = \frac{\left(\frac{\Delta m_{Si}}{m_{hm}}\right)}{\left(\frac{\Delta m_{S}}{m_{hm}}\right)} = \frac{\Delta n_{Si}}{\Delta n_{S}} \frac{M_{Si}}{M_{S}} = 0.5 \frac{M_{Si}}{M_{S}} = 0.44 \qquad (18)$$

Figure 2-19 shows the measured decrease in silicon content versus the measured decrease in sulphur content for both heats together with the relation described by (18). Linear fits through the measurement points are also shown.

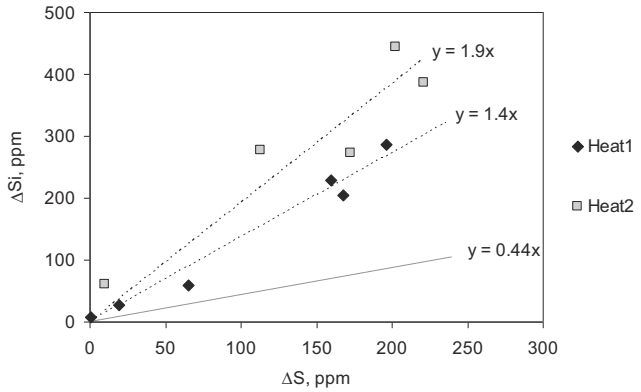

Figure 2-19. Decrease in silicon content versus decrease in sulphur content.

The observed decrease in silicon content is approximately four times higher than predicted by (18). Most likely silicon reacts with oxygen from the air. During the injection process the slag layer is pushed aside from the spout area and hot metal is exposed to the air.

Kishimoto et al.[20] performed measurements on the surface wave propagation on gas-stirred steel ladles and calculated the energy dissipation in the bulk. They concluded 41 % of the energy supplied by the gas injection is dissipated in the spout zone. Although steel and steel slag differ from hot metal and desulphurisation slag, intensive mixing between hot metal, air and slag can be expected in the spout zone. SiO_2 formed by reaction with oxygen from the air is likely to be directly absorbed into the slag layer. This would explain the absence of SiO_2 particles in samples of the hot metal bulk analysed in section 2.2.

2.4 Concentration of MgS particles

2.4.1 Automated Inclusion Analysis

In the microscopic analysis described in section 2.2, various phases and compounds were found in hot metal samples. To obtain quantitative results of the concentrations of these phases, Automated Inclusion Analysis (AIA) was used. This is suggested by Story et al.[21] as a suitable technique to study the reaction product in liquid steel samples. The analysis begins with a SEM backscatter image of a relatively large surface area, called a frame. Based on differences in grey scale spots are identified as potential particle cross sections. Subsequently each spot is scanned in more detail: shape factors are determined and the average chemical composition is measured with EDS. When all spots in the frame are scanned, a new frame is taken until the preset number of spots is analysed. The result is a list of all spots in the scanned area with their measured properties.

2.4.2 Identification of Mg-Mn-S-Ti particles

To minimise the chance that a particle is missed, the threshold for the greyscale of a possible particle is set close to the greyscale of the iron matrix. This increases the chance that small holes, scratches and dust particles are identified as potential particles. With

EDS analysis of these spots, only emission from the iron matrix is measured. Iron is considered to be part of the matrix only and not a particle constituent. The emission from iron therefore is excluded in the derivation of the chemical composition from the measured spectrum. For a non-particle this results in a weak response and a spectrum composed of noise. The intensity is expressed as the number of EDS Max Peak Counts. For a particle this should be at least 75 counts. When the chemical composition is derived from noise, this results in concentrations of elements unlikely to be present in the sample like Cu, Zn and Zr. For a particle the total molar fraction of these elements should not exceed 3 %.

Each sample from Table 2-3 is analysed with the following settings:

Pixel size	0.148 µm
Frames size	4096 x 3078 pixels or 606 x 456 µm
Magnification	500
Number of spots analysed:	5000

As described in section 2.2 particles found in hot metal samples can be composed of Ti(C,N), Ti_8S_3, MnS, MgS and MgO. Carbon, nitrogen and oxygen are not measured with the EDS analysis. Particles of interest thus have high Mg, Mn, S, or Ti concentrations. Figure 2-20 shows the number of particles as function of the sum of the molar fractions of these elements. For most samples, this number drops at a total molar fraction of around 0.9.

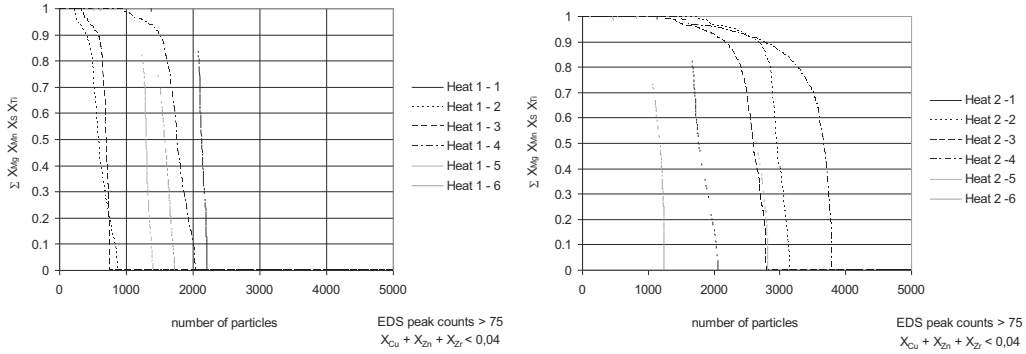

Figure 2-20. Selection criterion for identification of particles.

These considerations result in the following criteria for the identification of particles of interest:

EDS Max Peak Counts > 75

AND $X_{Cu} + X_{Zn} + X_{Zr} < 0.03$

AND $X_{Mg} + M_{Mn} + X_S + X_{Ti} > 0.9$

Table 2-7 shows the results of the analysis. Due to time restrictions the analysis of the first two samples of Heat 1 were stopped preliminary at, respectively, 3216 and 4735 spots.

Table 2-7. Results of Automated Inclusion Analysis on hot metal samples

sample	number of scanned frames	total scanned area (mm^2)	number of Mg-Mn-S-Ti particles
Heat 1-1	15	4.13	1968
Heat 1-2	11	3.03	396
Heat 1-3	7	1.80	572
Heat 1-4	7	1.78	1502
Heat 1-5	8	1.97	1040
Heat 1-6	5	1.26	1198
Heat 2-1	18	4.83	1587
Heat 2-2	11	2.99	2663
Heat 2-3	10	2.66	2156
Heat 2-4	11	2.89	2745
Heat 2-5	11	2.85	1641
Heat 2-6	5	1.28	857

Compared to Heat 1, in the samples from Heat 2, more of the initially identified spots appear to be Mg-Mn-S-Ti particles. This is probably due to differences in sample preparation and/or presence of graphite segregates in the samples.

2.4.3 Development of MgS particles

For each sample, every particle meeting pre-mentioned criteria is depicted in a Ti-Mn-S-Mg-composition plot generated using methods developed by E. Zinngrebe.[22],[23] The plots are given on the following pages. The compositions of the pure compounds are shown as well. An explanation for the transition in particle content during the injection process is given next to each figure.

In the first few samples of both heats, a considerable number of particles are present on the Ti-S line. Figure 2-21 shows the molar fraction of titanium in particles for which $X_{Ti} + X_S > 0.95$. The peak at $X_{Ti} = 1$, referring to Ti(C,N) particles, is not shown. With both heats, the peak in X_{Ti} coincides with the composition of Ti_8S_3. This compound therefore is also shown in the composition plots. In Heat 1, a peak coinciding with Ti_2S can also be recognised.

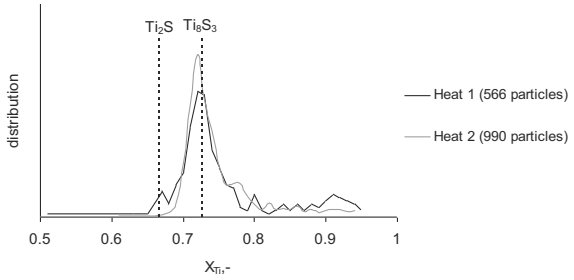

Figure 2-21. Distribution of X_{Ti} in particles composed of titanium and sulphur.

Analysis of the EDS spectra pointed out the small manganese content of particles primarily composed of titanium results from noise in the measurement and the signal from the surrounding iron matrix. These particles are solely composed of Ti(C,N).

Since the oxygen, carbon and nitrogen content of the particles are not measured, particles on the Mg-Ti line probably are multiphase particles composed of MgO and Ti(C,N) or TiO_2. This indicates that the oxygen activity increases during the post-injection of lime. Oxygen picked up at the spout eye would not result in MgO particles suspended in the hot metal since oxides formed would be absorbed in the slag layer directly as explained in 2.3.5. A possible source of oxygen source might be some hydroxide in the injected lime. During simultaneous injection of magnesium and lime this oxygen reacts with magnesium vapour in the plume directly and the oxides rise to the slag together with the CaO/CaS particles. When the magnesium injection stops this oxygen could react with magnesium dissolved in the hot metal forming suspended MgO particles.

In the sample from Heat 1, taken after 3 minutes MnS is still present whereas in the sample from Heat 2 taken at that time no MnS is found anymore. This is explained by the higher sulphur level of the Heat 1 sample. In sample from Heat 2 taken 10 minutes after the start of the injection process, no MgS particles are found anymore indicating complete flotation of these particles to the slag layer. The last sample from Heat 1, taken nine minutes after the start of the injection process was not available for AIA anymore.

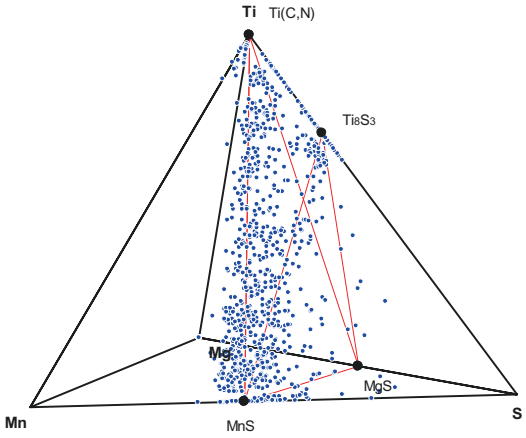

Heat 1 - sample 1, t = 0 min.

Mg and CaO has not yet been injected. Due to the high sulphur content, pure and multiphase particles composed of MnS and Ti_8S_3 are formed along with Ti(C,N) during solidification of the sample. Ti(C,N) particles show some enrichment with Mn.

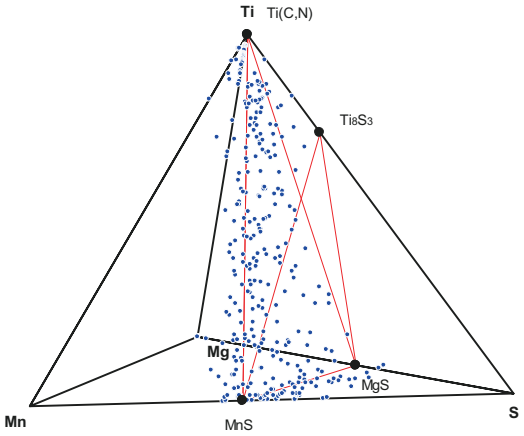

Heat 1 - sample 2, t = 1 min.
Injection of Mg and CaO has commenced. Some MgS particles have formed during injection. MnS-MgS and MnS-Ti(C,N) particles are formed during solidification of the sample. Due to the lowered sulphur content Ti_8S_3 is not formed anymore.

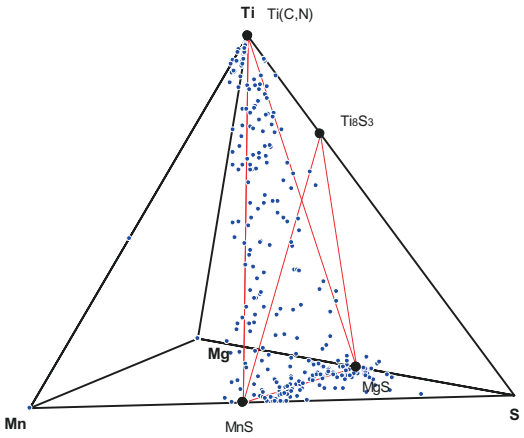

Heat 1 - sample 3, t = 2 min.
The concentration of MgS particles has increased. MnS is still formed on MgS particles during solidification of the sample.

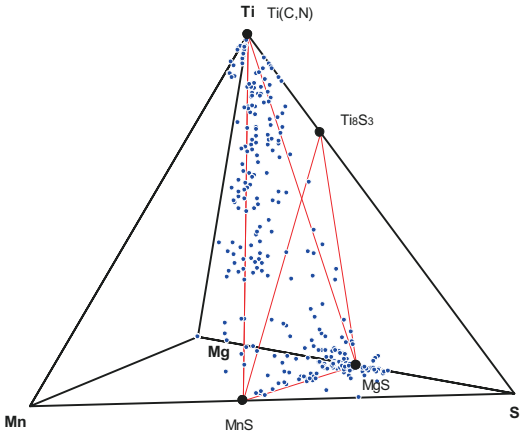

Heat 1 - sample 4, t = 3 min.
The same observations hold for the sample taken at 2 min.

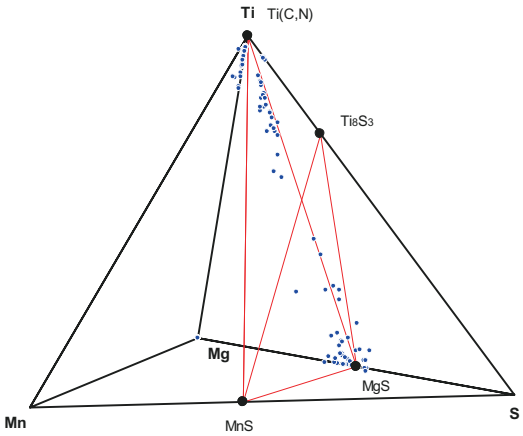

Heat 1 - sample 5, t = 5 min.
The sulphur concentration has lowered such that MnS is not formed anymore during solidification.
Compared to sample 4 the MgS concentration has lowered.

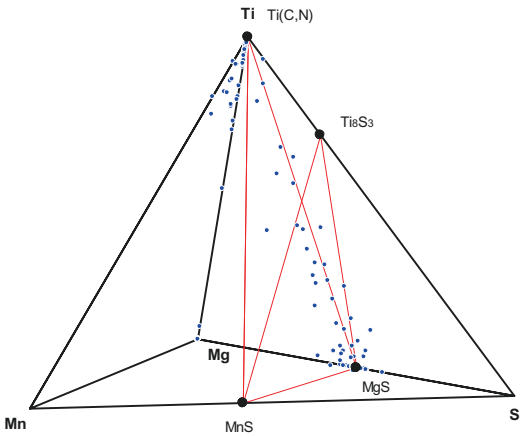

Heat 1 - sample 6, t = 6 or 9 min.
The same observations hold for the sample taken at 5 min.

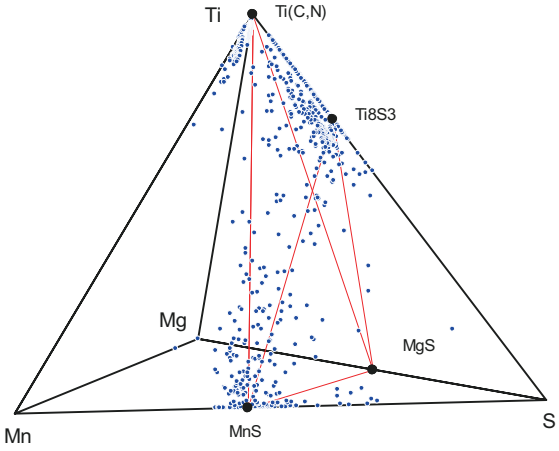

Heat 2 - sample 1, t = 0 min.
Mg and CaO has not yet been injected. Due to the high sulphur content, pure and multiphase particles composed of MnS and Ti_8S_3 are formed together with Ti(C,N) during solidification of the sample. Ti(C,N) particles show some enrichment with Mn.

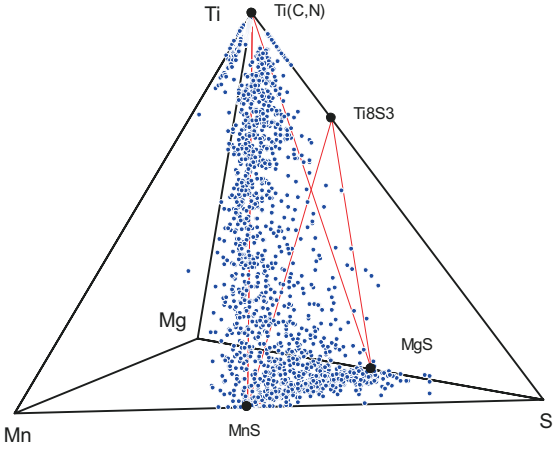

Heat 2 - sample 2, t = 1 min.
Injection of Mg and CaO has commenced. MgS particles have formed. MnS-MgS and MnS-Ti(C,N) particles are formed with the solidification of the sample.

Due to the lowered sulphur content Ti_8S_3 is not formed anymore.

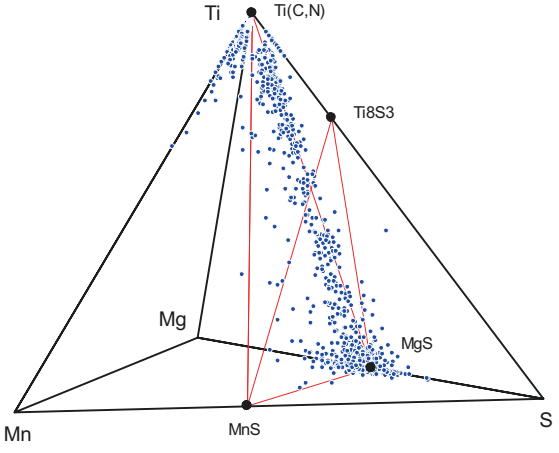

Heat 2 - sample 3, t = 3 min.
The concentration of MgS particles is high. With the solidification of the sample Ti(C,N) is deposited on the MgS particles. MnS is not formed anymore due to the lowered sulphur concentration.

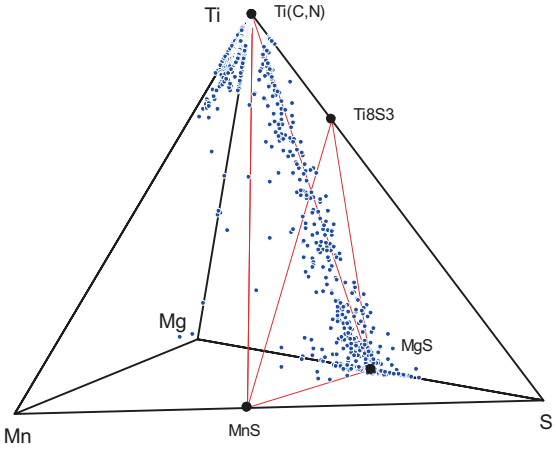

Heat 2 - sample 4, t = 5 min.
Sulphur content is further reduced and the concentration of MgS particles is decreasing due to flotation.

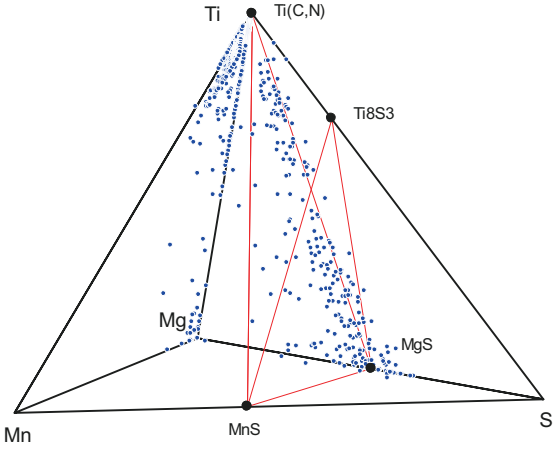

Heat 2 - sample 5, t = 7 min.
Magnesium injection is stopped while CaO injection still continues. MgS particles however are still suspended in the hot metal.

MgO particles (in the Mg-corner) are formed.

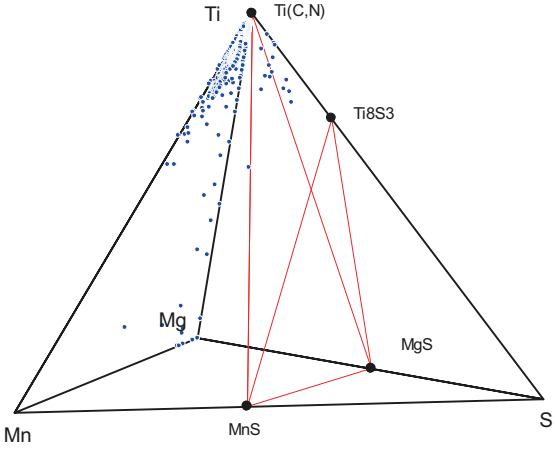

Heat 2 - sample 6, t = 10 min.
CaO injection is finished. MgS particles have been removed by flotation. The only particles found are some MgO particles and Ti(C,N) particles formed with solidification of the sample.

2.4.4 MgS content

It was shown in section 2.3.3 that during injection the product of the magnesium and sulphur concentrations can be well above the solubility product of MgS. To investigate to which extent this is caused by the accumulation of MgS particles, the concentration of MgS is derived from the AIA results.

For randomly oriented particles suspended in a matrix, the volume fraction of the particles equals the surface fraction of the particle intersections in the plane of analysis. With AIA measurements, the cross-sections of particles in the plane of analysis are measured together with their overall composition. So from these results, the concentration of MgS can be derived.

MgS often is present in multiphase particles. The volume fraction of MgS in a particle is derived as follows. It is assumed that a particle can be composed of Ti(C,N) or (Mg,Mn)S. In the first samples of both heats, Ti_8S_3 is found as well but this does not appear in samples were MgS particles are found. Thus for each particle:

$$X_{(Mg,Mn)S} + X_{Ti(C,N)} = 1 \tag{19}$$

With used criteria for the identification for particles from the measurement results, a particle can contain up to 10 % other elements. These elements are excluded in these calculations by normalisation.

The concentrations of carbon and nitrogen are not measured but it can be assumed that for each mole of titanium one mole of carbon or nitrogen is also present. This is taken into account by doubling the mole fraction of titanium.

For each particle the molar fractions of (Mg,Mn)S and Ti(C,N) thus can be calculated from the overall mole fractions by:

$$X_{(Mg,Mn)S} = \frac{X_{Mn} + X_{Mg} + X_S}{2X_{Ti} + X_{Mn} + X_{Mg} + X_S} \tag{20}$$

$$X_{Ti(C,N)} = \frac{2X_{Ti}}{2X_{Ti} + X_{Mn} + X_{Mg} + X_S} \tag{21}$$

The molar fractions of MgS and MnS follow from:

$$X_{MgS} = \frac{X_{Mg}}{X_{Mg} + X_{Mn}} X_{(Mg,Mn)S} \qquad X_{MnS} = \frac{X_{Mn}}{X_{Mg} + X_{Mn}} X_{(Mg,Mn)S} \tag{22}$$

The volume fraction of MgS, $f_{v,MgS,p}$ of the particle can be calculated using the molar volumes, V_m of the compounds:

$$f_{v,MgS,p} = \frac{X_{MgS} V_{m,MgS}}{X_{MgS} V_{m,MgS} + X_{MnS} V_{m,MnS} + X_{Ti(C,N)} V_{m,Ti(C,N)}} \tag{23}$$

The molar volumes of the compounds follow from:

$$V_{m,j} = \frac{M_j}{\rho_j} \tag{24}$$

Table 2-8 lists the properties used to calculate the molar volumes.

Table 2-8. Compound properties

		MgS	MnS	Ti_8S_3	Ti(C,N)	MgO
Density	(kg/m³)	2840	3990	4695	5000	3583
Molar mass	(g/mol)	56,4	87,0	479,5	60,9	40,3
Molar volume	(m³/kmol)	0,020	0,022	0,102	0,012	0,011

The total volume fraction of MgS in the hot metal is equal to the sum of surfaces of the MgS part of the cross section of each particle divided by the scanned area:

$$f_{v,MgS,HM} = \frac{\sum A_{pc} f_{v,MgS,p}}{A_{scan}} \tag{25}$$

The content of suspended MgS in ppm, then follows from:

$$[ppmMgS] = f_{v,MgS,HM} \frac{\rho_{MgS}}{\rho_{HM}} \cdot 10^6 \tag{26}$$

For solidified hot metal a density of 6800 kg/m³ is taken.

The composition plots of samples 2-5 and 2-6 indicates the presence of particles on the Ti-Mg-line. These most likely are particles composed of Ti(C,N) and MgO. These particles are excluded from the calculations. The results of the calculations are given in Table 2-9.

Table 2-9. MgS-content derived from AIA measurement.

Sample	No. of MgS particles	$\sum A_{pc} f_{v,MgS,p}$ (µm²)	A_{scan} (10^6 µm²)	$f_{v,\ MgS}$ (ppm)	MgS-content (ppm)
1 – 1	0	0	3.85	0	0
1 – 2	54	22	2.75	8	4
1 – 3	103	139	1.38	101	44
1 – 4	384	324	1.65	196	86
1 – 5	338	445	1.93	231	101
1 – 6	161	170	1.10	154	67
2 -1	0	0	4.68	0	0
2 -2	719	325	2.75	118	52
2 -3	754	777	2.48	314	137
2 -4	428	511	2.75	186	81
2 -5	149	89	2.75	32	14
2 -6	4	0	1.10	0	0

Figure 2-22 compares these MgS contents to those derived from the XRF analysis (section 2.3.3).

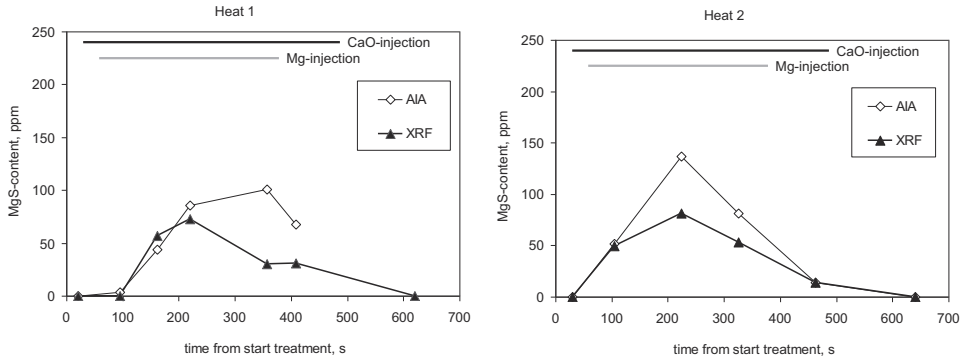

Figure 2-22. MgS contents derived from XRF analysis and AIA measurements.

Figure 2-22 shows the AIA measurements result in higher MgS-contents. For Samples 1-5 and 1-6 the sulphur content of the MgS particles exceeds the total sulphur content as measured with XRF. For the different methods of determining the MgS-content the following error sources are identified:

- The measured total Mg content: the XRF-analyser is not calibrated for analysis of the Mg-content.

- The solubility product of MgS: if the solubility product is estimated too high, the derived MgS content is underestimated. However, to bring the two results in better agreement, a value of 200 ppm² must be used. This is considerably lower than published values.
- Derivation of MgS surface: several assumptions and simplifications are made with the identification of particles from the AIA results and the derivation of MgS content of each particle.
- Inhomogeneity of MgS particles in the sample: with XRF analysis the complete bottom side of the sample, 12.5 cm² is analysed and an average composition is obtained, see Figure 2-23. With the AIA measurement, approximately 2 mm² is scanned. The intermediate results of the derivation of the MgS-content from AIA measurements show that a significant part of the total MgS content is formed by a small number of relatively large, larger than 2.5 µm, particles. A non-homogeneous distribution of such particles thus can lead to different results.

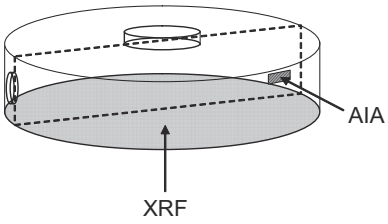

Figure 2-23. Plane of analysis of hot metal samples.

Considering these errors, the results show an agreeable similarity. The differences for samples 1-5 and 1-6, most likely, are caused by non-homogeneous distribution of the particles. The finding that the Mg and S concentrations exceed the MgS solubility product thus can be attributed to the accumulation of MgS particles in the hot metal.

For the industrial practice optimum efficiency of injected magnesium must be obtained. It therefore is important that after the injection process all MgS particles are removed from the hot metal by flotation. AIA measurements are too complicated for monitoring purposes in the industrial process. XRF analysis, however, is already done regularly. To optimise the process, XRF analysis on the final samples, extended with analysis of Mg, even indicative, can be used to determine if the product of sulphur and magnesium concentration in the final samples is below the solubility product and the MgS particles have properly been removed to the slag layer.

2.4.5 Number density of MgS particles

Assuming the MgS particles are spherical with diameter d_p, the concentration of MgS particles suspended in hot metal is described by the number density $f_1(d_p)$ which represents the number of particles per unit volume in the size range $d_p + \partial d_p$. The dimension is number per unit volume per particle diameter so $1/L^4$. Since the particle size is of the order of µm, $1/(\mu m)^4$ is used. For convenience this is written as $1/\mu m^4$. Using

stereological techniques as derived by M. Higgins [24], the number densities of the MgS particles in the hot metal samples are derived from the AIA measurement results.

Figure 2-24 and Figure 2-25 show the measured number densities of MgS particles in the samples taken during the injection of lime and magnesium. The samples in which no MgS particles were found, are absent in the graphs.

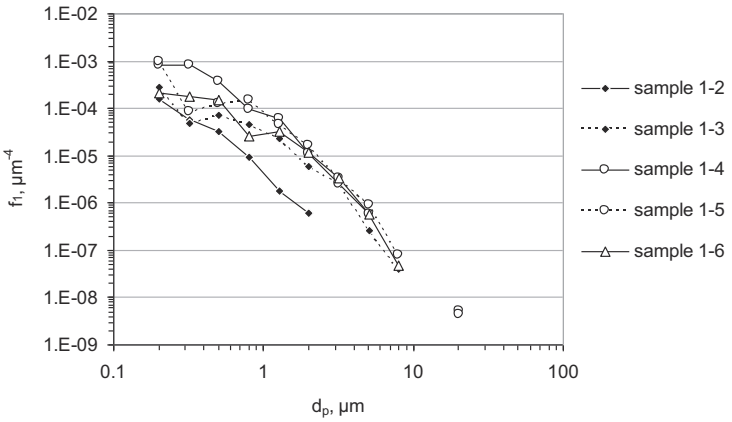

Figure 2-24. Number densities of MgS particles during desulphurisation Heat 1.

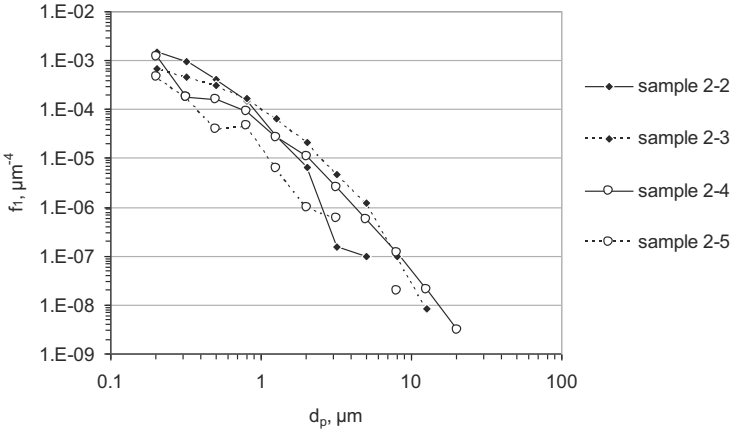

Figure 2-25. Number densities of MgS particles during desulphurisation Heat 2.

For both heats the results are comparable. Initially no MgS is present. After one minute MgS particles up to 5 µm in size appear. With Heat 2 the initial concentration of particles is almost a tenfold of Heat 1. No explanation is given for this. For the following samples, the concentrations are comparable. After three minutes, the concentration of particles increases over the entire size range and particles larger than 5 µm are found. This indicates growth of particles and generation of new particles. Later in the process, the concentration of particles decreases over the entire size range due to flotation and the

diminishing reaction rate. With the transition from sample 4 to 5 from Heat 2 the number of particles decreases over the entire size range. Sample 5 was taken after the end of magnesium injection. This indicates that MgS particles were formed during the injection and no new particles are formed anymore. The decrease in concentration is higher for larger particles. This indicates that the rate of flotation increases with particle size. With Heat 1 the time interval between the end of Mg-injection and taking the second last sample is shorter. The aforementioned transition thus is less clear. See Figure 2-16.

2.4.6 MgO particles

To investigate their possible role in the precipitation of MgS, the presence of MgO particles is investigated. In the composition plots, all pure MgO particles lie in the Mg-corner and no indication of the number of particles can be seen. Table 2-10 therefore lists the number of particles with $X_{Mg} > 0.9$ identified from the AIA results of each sample.

Table 2-10. Measured number of MgO particles in the hot metal samples.

sample	No. of MgO particles	sample	No. of MgO particles
1-1	0	2-1	1
1-2	1	2-2	0
1-3	1	2-3	0
1-4	0	2-4	0
1-5	0	2-5	11
1-6	0	2-6	4

Only in the last two samples of Heat 2a number of MgO particles is recognised. In the composition plots, MgS particles containing MgO would lie on the line between the Mg-corner and the MgS point. No particles are found here indicating MgO is not present in significant amounts.

If, like Figure 2-9, a particle contains a small fraction of MgO, the molar fraction of Mg would be slightly higher than the molar fraction of S. For three samples of the second heat, Figure 2-26 shows the ratio of the molar fractions versus the particle diameter. For this, particles with a molar fraction of MgS of at least 0.5 are grouped in classes of particle diameter. For each size class, containing at least 10 particles, the average of the ratio is calculated and shown in the graph. Even for the particles smaller than 1µm the number of EDS-counts ranges from 100 to 1000 indicating accurate measurement of the compositions.

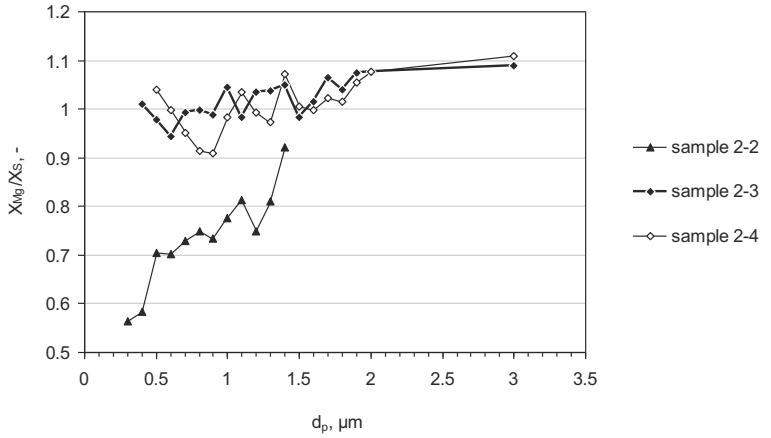

Figure 2-26. Ratio of molar fractions of Mg and S in MgS particles.

Figure 2-26 does not indicate that the molar fraction of Mg increases for smaller particles which could indicate the presence of MgO in the particle. For the second sample of Heat 2 the molar fraction of magnesium is lower than the molar fraction of sulphur. This is explained by the presence of MnS in the particles in the samples taken at the beginning of the injection process.

With microscopic analysis the particle shown in Figure 2-9 was the only one found of this kind whereas pure MgS particles or MgS/Ti(C,N) multiphase particles were found in high concentrations. Based on the results of their laboratory scale measurements Lindström et al.[10] concluded MgS is formed by precipitation on MgO particles, originating from the oxide layer on the magnesium granules. This conclusion can not be confirmed with the current measurements.

2.4.7 Other particles

With the microscopic research described in section 2.2 no particles containing CaO, CaS or SiO_2 were found. To identify these particles from the AIA measurement results, the following criteria were applied:

EDS Max Peak Counts > 90

AND $X_{Na} + X_{Cl} + X_K + X_{Cu} + X_{Zn} + X_{Zr} < 0.03$

AND $X_{Al} + M_{Ca} + X_S + X_{Si} > 0.8$

For completeness, Al is included as well.

Table 2-11 lists the number of particles containing Al, Ca, S or Si for each sample. The results for the first two samples of both heats could indicate to dispersion of blast furnace slag. With tapping through open air from the torpedo into the hot metal ladle, the hot metal falls approximately five meters. The high velocity of the falling hot metal induces high shear at the bath surface covered with blast furnace slag carry-over. This can induce

dispersion of slag in the hot metal bath. As a result of the injection process particles are flushed out again.

Table 2-11. Al-Ca-C-Si particles in the hot metal samples.

sample	particles containing Al, Ca, S or Si.
Heat 1-1	5 particles with $X_{Si} > 0.9$, 4 smaller than 1 µm², 1 of 154 µm²
	11 particles composed of Al, Ca and Si in varying compositions and sizes ranging from 0.1 to 90 µm²
Heat 1-2	6 particles composed of Ca and Si, all smaller than 0.4 µm²
Heat 1-3	1 particle with $X_{Ca} = 1$, size 1.0 µm²
Heat 1-4	12 particles with Si and Ca of varying composition, sizes ranging from 0.1 to 15 µm²
Heat 1-5	5 particles of varying composition, sizes ranging from 0.3 to 10 µm²
Heat 1-6	1 particle with $X_{Si} = 0.82$, size 1.73 µm²
	2 particles with $X_{Al} = 0.45$ and $X_{Si} = 0.45$, size 0.6 and 1.3 µm²
Heat 2 -1	21 particles of varying compositions
Heat 2 -2	16 particles of varying compositions
Heat 2-3	1 particle with $X_{Ca} = 1$, size 4.8 µm²
	2 particles with $X_{Si} = 0.95$, sizes of 1.7 and 1.3 µm²
Heat 2-4	2 particles with $X_{Si} = 0.9$, sizes of 0.76 and 0.26 µm²
Heat 2-5	1 particle of 0.22 µm² with 93 EDS counts
Heat 2-6	no particles

The samples taken at a later stage in the injection process contain very little Al-Ca-S-Si particles. For unknown reasons, only the results for sample 1-4 stand out. Over-all no CaO/CaS or SiO_2-particles are present in the hot metal bulk during the desulphurisation process. Injected lime powder thus is directly washed out from the bubble plume and is not entrained with the hot metal circulation flow. Two possible explanations can be given for this. The first is that upon injection a part of the lime powder leaves the gas bubble and gets dispersed in the hot metal. When the multi-phase bubble plume reaches the bath surface, the lime particles are completely washed out to the slag layer. The second possible explanation is that lime powder is not dispersed in the hot metal and remains in the gas bubble. When the bubble breaks up at the surface, the lime powder is released and collects at the slag layer floating on top.

In section 2.3.5 the decrease of hot metal Si-content is described. The small number of SiO_2-particles found in these samples confirms the assumption that this decrease is due to oxidation at the spout zone where hot metal is exposed to the air.

2.5 Summary and conclusions

The desulphurisation reactions have been studied by sampling the hot metal bath during the injection process and applying various microscopic techniques. The results can be summarised as follows:

- The reaction product MgS is found as component of either single- or multi-phase particles dispersed in hot metal. The MgS multi-phase particles are the result of the deposition of solidification products, like Ti(C,N), Ti_8S_3 and MnS formed during cooling of the hot metal sample.
- The concentration of dispersed magnesium particles during the injection process is considerable and contributes to the total sulphur and magnesium contents. The particle sizes indicate growth and flotation of particles during the injection process. This explains the observed low initial desulphurisation rate and the apparent super saturation of MgS.
- MgO only is rarely observed as part of MgS/MgO multiphase particles.
- MgO particles can be formed during the post-injection of lime, when the Mg-injection is stopped. Most likely this is due to the reaction of dissolved magnesium with oxygen released from the injected lime.
- Lime particles are not dispersed into the bulk of the hot metal.
- During the injection process the hot metal silicon decreases, most likely due to oxidation at the spout area.

Table 2-12 lists the process conditions and observations of the various studies described in the introduction, section 2.1 and the process studied in the present work. Some properties, regarding dimension, were estimated. The other studies were all done on laboratory scale experiments. The differences in results can be attributed to differences in scale of dimensions and mixing affecting mass transfer:

- In comparison to a large ladle stirred by gas injection, in a small induction stirred furnace mixing of the hot metal is better and the rate of flotation of MgS higher.
- In an industrial ladle, the residence time of the injected magnesium into the hot metal bath is longer than in a laboratory scale set-up. This results in a higher over-all efficiency of injected reactants.
- The ferrostatic pressure at the point of injection results in a higher vapour pressure of magnesium. This results in an increased driving force for dissolution and less violent behaviour in the hot metal bath, also resulting in a higher over-all efficiency of injected reactants.

Summarising the results it is concluded that the mechanism for formation and growth of MgS particles as proposed by Irons and Guthrie gives a good description of the desulphurisation of hot metal by injection of magnesium. To correctly describe the

process on a industrial scale however, the accumulation and flotation of MgS particles must be taken into account as well.

Table 2-12. Comparison of the laboratory and industrial scale hot metal desulphurisation processes. * indicates estimated value.

	Irons and Guthrie[1],[2]	Yang et al.[3]	Mukawa et al.[9]	Lindström et al.[10]	BOS No.2
Set-up					
hot metal mass	60 kg	0.35 kg	25-30 kg	0.25 kg	300 t
vessel diameter	20 cm	4 cm	18 cm	± 3.5 cm*	4 m
magnesium added	30-140 g	1.5 g MgO/C: 0.7 g Mg	6 g	0.42 g	120-140 kg
g Mg/kg hot metal	0.5-2.3	2	0.2-0.24	1.7	0.4-0.47
material injected	Mg vapour, pure or mixed with Ar	Mg vapour and Ar	Mg vapour and Ar	Mg chips and CaO powder	Mg granules and CaO powder with N_2 as carrier gas
Conditions					
injection time	30 - 60 min.	30-120 min.	20-60 min.	< 2 s	6 - 8 min.
hot metal temperature	1250 °C	1280-1500 °C	1350 °C	1500 °C	1380 °C
mixing conditions	induction stirring	induction stirring	induction stirring	-	bubble plume
immersion depth	± 15 cm*	4.9 cm	± 13 cm*	± 3 cm*	3.7 m
initial sulphur content	7-1900 ppm	500 ppm	200 ppm	460 ppm	230 ppm
final sulphur content	2-385 ppm	10-60 ppm	10-90 ppm	360 ppm	7 ppm
Observations					
MgS particles	one particle observed	-	-	observed in high concentrations	observed in high concentrations
MgO particles	not observed	-	-	observed in high concentrations	observed in low concentrations at end of injection
[Mg]×[S]	>K	-	-	57600 ppm² (360 ppm x 180 ppm)	>K during the process <K after post-injection
summary	Small, well stirred volume and slow rate of MgS production	Small, well stirred volume and slow rate of MgS production	Well stirred volume and slow rate of MgS production	Small volume, high rate of MgS and MgO production	Large, less well-mixed volume and high rate of MgS production

2.6 References

[1] G.A. Irons and R.I.L Guthrie: Kinetic aspects of magnesium desulphurization of blast furnace iron. Ironmaking and Steelmaking 8 (1981) 114

[2] G.A. Irons and R.I.L Guthrie: The role of an interfacial product layer in magnesium desulphurization of molten iron. Canadian Metallurgical Quarterly 21 (1982) 429-443.

[3] J. Yang, S. Ozaki, R. Kakimoto, K. Okumura, M. Kuwabara and M. Sano: Desulfurization of molten iron with magnesium vapor produced in-situ by carbothermic reduction of magnesium oxide. ISIJ Int. 41 (2001) 945-954.

[4] J. Yang, K. Okumura, M. Kuwabara and M. Sano: Desulfurization of molten iron with magnesium vapor produced in-situ by aluminothermic reduction of magnesium oxide. ISIJ Int. 41 (2001) 965-973.

[5] J. Yang, K. Okumura, M. Kuwabara and M. Sano: Effects of operating parameters on desulfurization of molten iron with magnesium vapor produced in-situ by aluminothermic reduction of magnesium oxide. ISIJ Int. 42 (2002) 595-602.

[6] J. Yang, K. Okumura, M. Kuwabara and M. Sano: Behavior of magnesium in the desulfurization process of molten iron with magnesium vapor produced in-situ by aluminothermic reduction of magnesium oxide. ISIJ Int. 42 (2002) 685-693.

[7] J. Yang, K. Okumura, M. Kuwabara, and M. Sano: Improvement of desulfurization efficiency of molten iron with magnesium vapor produced in situ by aluminothermic reduction of magnesium oxide. Metall. Mater. Trans. B 34 (2003) 619-629.

[8] J. Yang, M. Kuwabara, T. Teshigawara and M. Sano: Mechanism of Resulfurization in Magnesium Desulfurization Process of Molten Iron. ISIJ Int. 45 (2005) 1607-1615.

[9] S. Mukawa, Y. Ueshima, M. Sano, J. Yang and M. Kuwabara: The effect of magnesium gas injecting conditions on the rate of hot metal desulfurization. ISIJ Int. 46 (2006) 1778-1782.

[10] D. Lindström, P Nortier and D. Sichen: Functions of Mg and Mg-CaO mixtures in hot metal desulphurisation. Steel. Res. Int. 85 (2014) 76-88.

[11] H.J. Visser and R. Boom. Development of a reactor model of hot metal desulphurisation on an industrial scale. Proceedings of the SCANMET III-3rd International Conference on Process Development in Iron and Steelmaking Volume 2, 8-11 June 2008, Luleå, Sweden, pp. 147-156.

[12] Y. Li, Y. Li and R. J. Fruehan: Formation of Titanium Carbonitride from Hot Metal. ISIJ Int. 41 (2001) 1417–1422.

[13] K.D. Millis: Cast Ferrous Alloy. US patent 2485760, issued October 25, 1949.

[14] B. J. Skinner and F. D. Luce: Solid solutions of the type (Ca,Mg,Mn,Fe)S and their use as geothermometers for the enstatite chondrites. The American Mineralogist 56 (1971) 1269-1296.

[15] K. Oikawa, H. Ohtani, K. Ishida and T. Nishizawa: The control of the morphology of MnS inclusions in steel during solidification. ISIJ Int. 35 (1995) 402-408.

[16] K. Oikawa, K. Ishida and T. Nishizawa: Effect of titanium addition on the formation and distribution of MnS inclusions in steel during solidification. ISIJ Int. 37 (1997) 332-338.

[17] E.T. Turkdogan: Fundamentals of steelmaking, Book 656, The Institute of Materials, London, 1996, p.124.

[18] A. Ender, H. van den Boom, H. Kwast and H. Lindenberg: Metallurgical Development in Steel-plant-internal Multi-injection Hot Metal Desulphurisation. Steel Research Int. 76 (2005) 562-572.

[19] N.A. Voronova: Desulfurization of hot metal by magnesium. The international Magnesium Association, Dayton, Ohio and The Iron and Steel Society of the American Institute of Mining, Metallurgical, and Petroleum Engineers, Warrendale, Pennsylvania, 1983, p.77-80.

[20] Y. Kishimoto. Y. Sheng, G. A. Irons and J-S. Chang: Energy Dissipation Distribution In Gas-stirred Liquids. ISIJ Int. 39 (1999) 113-122.

[21] S.R. Story, T.J. Piccone, R.J. Fruehan and M. Potter: Inclusion analysis to predict casting behaviour. ISSTech 2003 Conf. Proc., 2003, 129-139.

[22] E. Zinngrebe, C. van Hoek, H. Visser, A. Westendorp and I-H. Jung: Inclusion Population Evolution in Ti-alloyed Al-killed Steel during Secondary Steelmaking Process. ISIJ Int. 52 (2012) 52-61.

[23] E. Zinngrebe, P. Seda, S. van der Laan and B. van Arendonk: A new view on Ca treatment of Al killed steel using improved chemography and particle size analysis. Proc. 5th Int. Cong. on the Sci. Technol. of Steelmaking, ENGICOM GmbH, Germany, (2012).

[24] Michael D. Higgins: Measurement of Crystal Size Distributions. American Mineralogist 85 (2000) 1105-1116.

3 The hot metal/slag interface during desulphurisation

3.1 Introduction

In the introduction section 1.3, it is explained that hot metal desulphurisation proceeds in two steps. With the first step, the injection of desulphurisation agents, sulphur dissolved in hot metal is bound to solid sulphide particles. These are subsequently washed out of the hot metal bath by the bubble plume. This was the subject of Chapter 2. The topic of this chapter is the second process step: the absorption of the sulphides into the slag layer followed by raking off this layer. Initially, at the start of the injection, this slag layer is formed by blast-furnace slag carry-over from tapping from the torpedo wagon. During the injection reaction products from the desulphurisation reactions and the silicon oxidation are added to this slag layer together with unreacted reagents. To study the hot metal/slag interaction during the injection, samples have been taken from the top layer of the hot metal bath, both after the injection and after slag raking.

3.2 Sampling

Using a large steel spoon covered with refractory material on a long rod, samples could manually be taken from the surface layer of the hot metal ladle. With this, care was taken to include the top layer of the hot metal bath. In addition samples from the uppermost slag layer were taken. The data of the heats from which the samples were taken are given in Table 3-1.

Table 3-1. Sampled heat data.

		Heat 1	Heat 2
Hot metal temperature	(°C)	1359	1374
Hot metal mass	(t)	307	300
Lime injected	(kg)	413	392
Magnesium injected	(kg)	136	129
Initial / final sulphur level	(ppm)	410 / 113	330 / 109
Si-content	(wt%)	0.31	0.40
Mn-content	(wt%)	0.38	0.39
Ti-content	(wt%)	0.049	0.065
Time required for slag removal	(min.)	10	9
Sample before slag removal		A-1	B-1
Sample after slag removal		A-2	B-2

Figure 3-1 shows how the samples were prepared for microscopic analysis. The centre parts are embedded in resin. The samples have been dry cut and polished to preserve the water-soluble components.

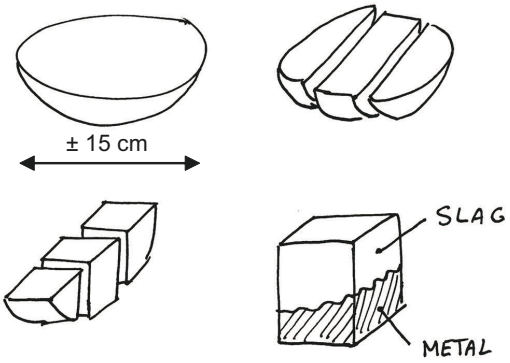

Figure 3-1. Preparation of the top layer samples.

The observations on the samples taken before and after slag removal are described in the following sections. In addition to these samples, extra samples where taken from especially the crumbly upper layer.

3.3 Top layer before slag removal

3.3.1 Layering of the samples

Figure 3-2 shows sample A-1 before embedding in resin. Sample B-1 has a similar appearance.

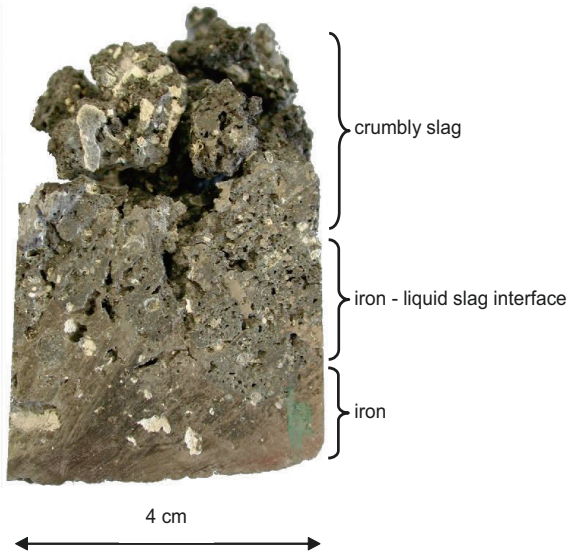

Figure 3-2. Sample A-1, taken before raking.

Three layers can be distinguished in the sample. From bottom to top these are:

1. The lower part of the sample is formed by solidified hot metal containing non-metallic particles clearly observable to the naked eye.
2. The interface between hot metal and liquid slag. This layer contains pores but has a solid structure. From this it appears that this slag layer has been, at least partially, liquid and has solidified after sampling.
3. The upper part of the sample is composed of crumbly slag with the same appearance as the slag parts in the interface layer. It appears that this layer was only partly liquid during the process.

In all layers, white dots are seen that are composed of lime. The crumbly uppermost layer of both hot metal/slag samples fell apart from these samples before it could be embedded in resin. Figure 3-3 shows a composition of optical microscopic images of sample B-1 after polishing. Included are the iron layer and the intermediate liquid slag layer. Due to the mirror-like high reflectivity of the polished iron, the slag and lime parts appear dark whereas in reality they are light grey.

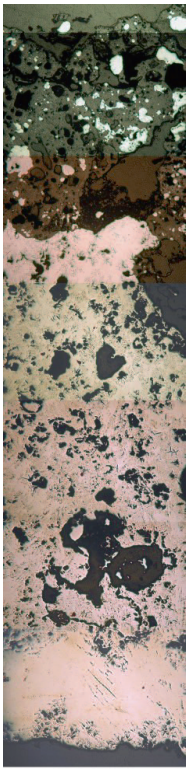

Figure 3-3. Sample B-1 embedded in resin and polished. The indicated areas are shown at higher magnifications in Figure 3-4 and Figure 3-14.

The next sections describe the microscopic analysis of each layer, starting bottom up.

3.3.2 The hot metal layer

Figure 3-4 shows the lowest of the regions indicated in Figure 3-3 at higher magnifications. The larger particles are composed of lime or slag. In the right-hand picture, clusters of MgS particles are recognised in between the graphite flakes. These clusters are found throughout the hot metal phase in the sample.

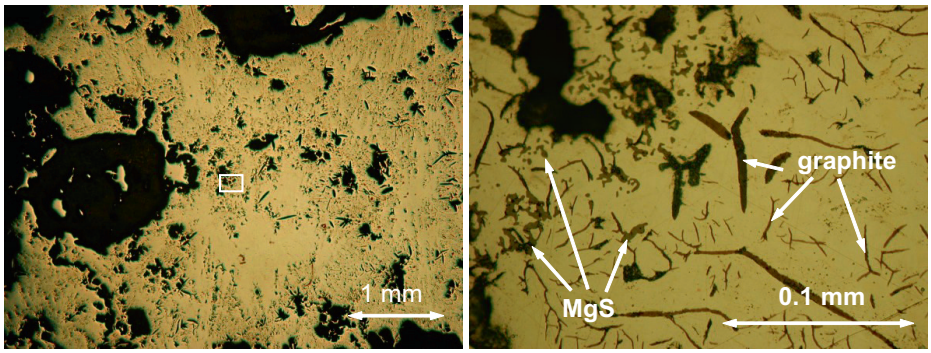

Figure 3-4. Optical microscopic images of the hot metal layer in sample B1.

In the iron layer of both samples, white to light grey spots are observable to the naked eye. With optical microscopy a large number of particles with similar appearances were found. Three particles have been studied in detail by SEM microscopy. It is assumed that the observations on these particles can be generalised to the greater part of the particles in this layer.

Figure 3-5 is an optical microscopic image of the iron phase in sample A-1 showing high concentrations of different non-metallic phases including laminar graphite. The circle was engraved to identify the particle in the centre for further SEM-analyses.

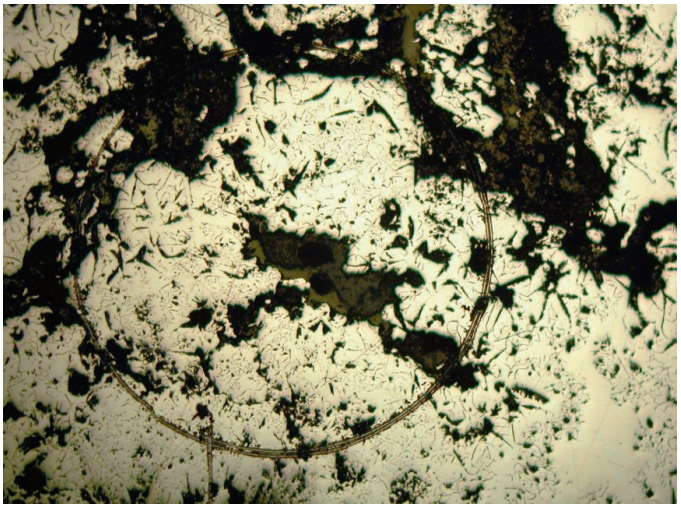

Figure 3-5. Optical image of the iron layer in sample A-1, taken before slag raking.

Figure 3-6 shows the particle in the centre of Figure 3-5 together with the combined EDS element mappings of Ca, Mg, O and S. The colours of the elements combine as shown in Figure 3-7.

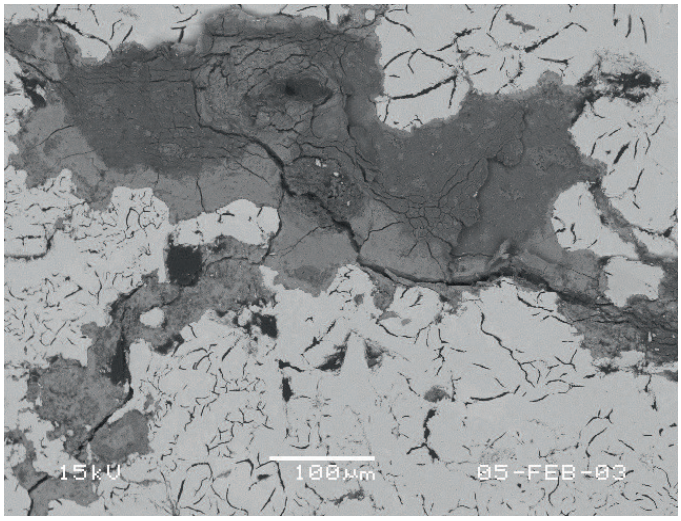

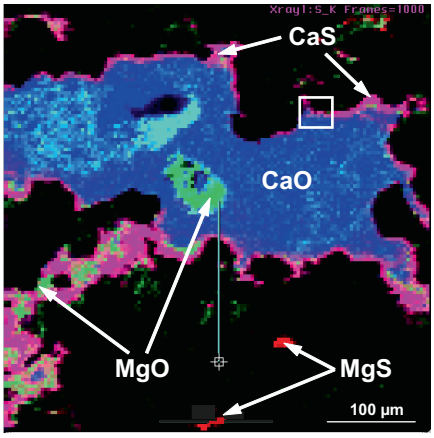

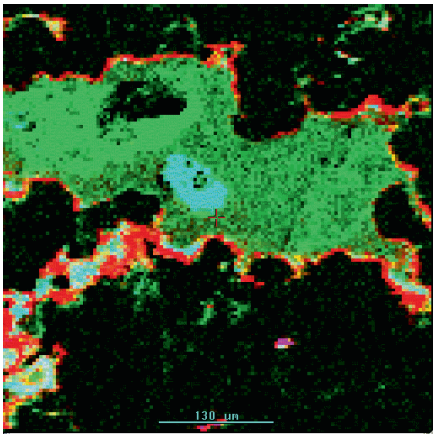

Ca:■, S:■, O:■ Mg:■, S:■, O:■

Figure 3-6. SEM-BS image and EDS-composition plot of a CaO particle in the iron layer in sample A-1, taken before slag raking.

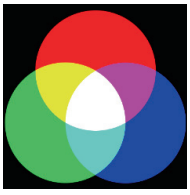

Figure 3-7. Additive combination of colours in element mappings.

The composition plot indicates that the particle is composed of CaO covered with a layer of CaS. Smaller particles composed of MgO and MgS are also present in the solidified iron. Figure 3-8 shows a close-up of the product layer the CaO particle, indicated by the white square in the composition plot in Figure 3-6.

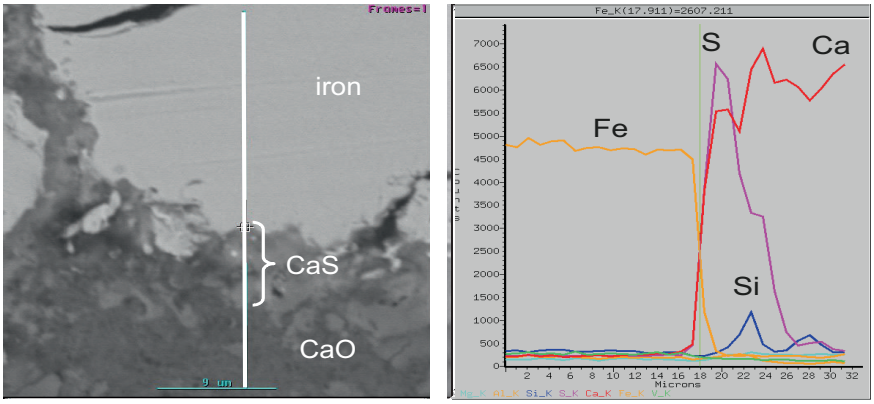

Figure 3-8. SEM/BS image and EDS line-scan of the CaS product layer.

On the right hand side the results of the EDS line-scan indicated by the white line in the SEM image are presented. The line-scan shows that the product layer is composed of CaS with sulphur concentration gradually decreasing inwards the lime particle. The product layer is enriched with Si. This indicates the presence of SiO_2/CaO.SiO_2. No enrichment with Mg, Mn or Fe is measured. This indicates MgO/MgS, MnS or FeO are not present in this product layer. The Fe-content decreases over a distance of approximately 2 µm which corresponds to the spatial accuracy of the EDS-measurement.

Figure 3-9 shows the image and a high resolution composition plot of the product layer on another lime particle from sample B-1.

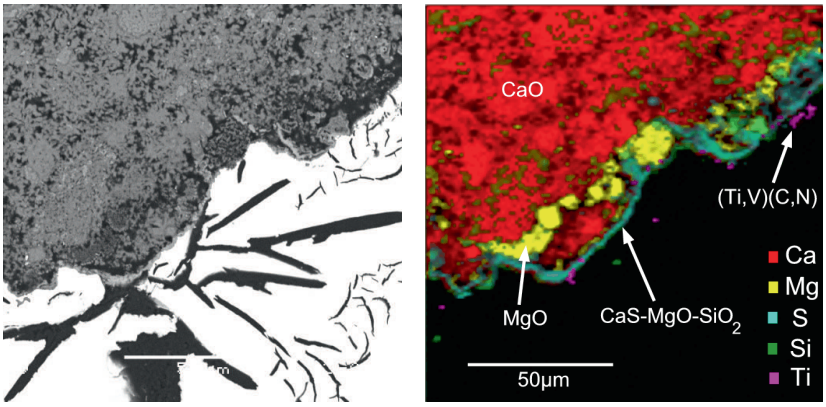

Figure 3-9. SEM-BS image and EDS composition plot of the product layer on a lime particle in sample B-1, taken before slag raking.

The distribution of phases is derived from the EDS element mappings. The particle is composed of CaO containing traces of SiO_2. According to the material specification of the

injected lime powder the upper limit for SiO_2 content is 2.5%. Furthermore, silicon oil is added to the powder to improve its properties for pneumatic transport.

The particle is covered with a product layer composed of CaS. In this layer Mg and Si are also detected indicating the presence of MgO and SiO_2. MgO as a separate phase is also found on the outer surface of the particle. It seems Mg has penetrated deeper into the lime particle than S. The product layer does not contain Mn or Fe. Furthermore, the titanium spots indicate the presence of Ti(C,N) particles on the product layer.

Another image, taken from sample B-1, is shown in Figure 3-10.

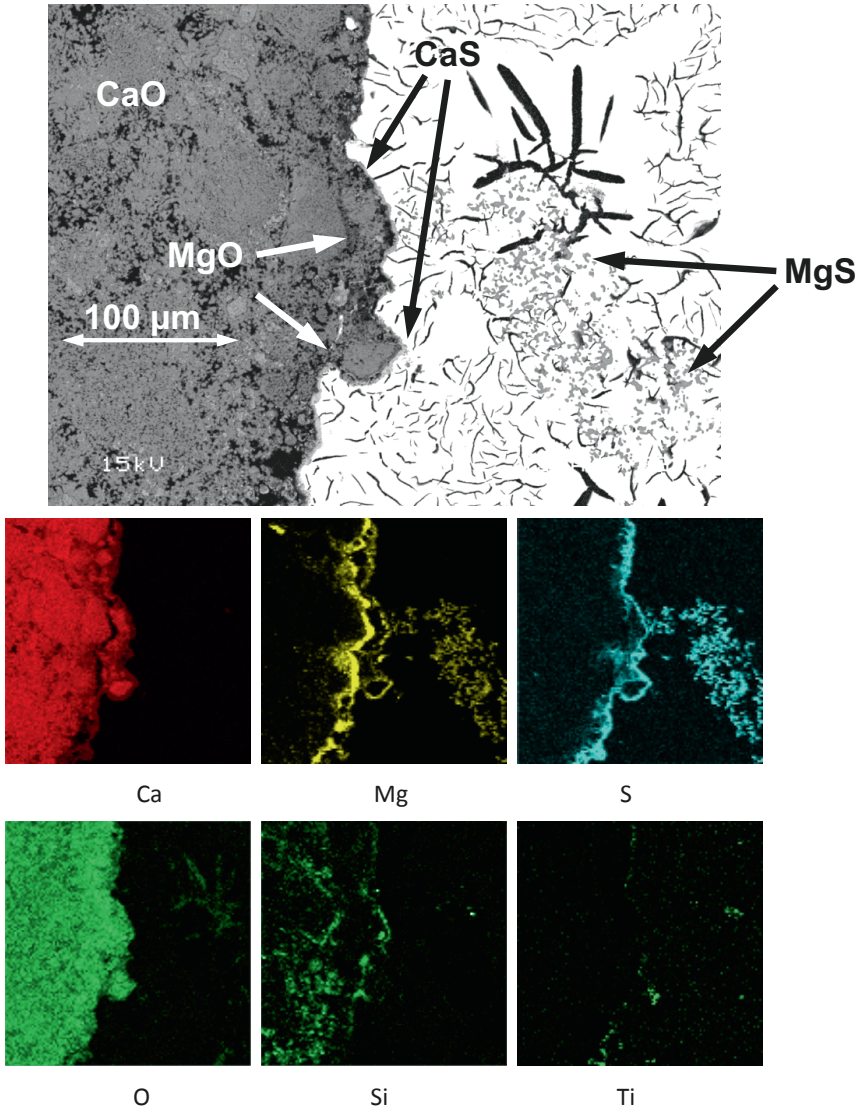

Figure 3-10. SEM-BS image and EDS element mappings of the product layer on a lime particle in sample B-1, taken before slag raking.

The lime particle in this picture also is covered with a CaS product layer enriched with Mg and Si, most likely bound to MgO and SiO_2. Similar to the observations on Figure 3-9, it seems Mg has penetrated deeper into the lime particle than S. Ti(C,N) particles are deposited on the lime particle and are also present as separate particles in the solidified hot metal matrix.

In the right half of Figure 3-10 clusters of MgS particles are present in the hot metal phase. In the SEM-BS image these are grey whereas the laminar graphite is black. These particles are observed throughout the iron layers of both samples. The MgS particles are larger and present in higher concentrations than those found in the samples taken from a depth of 60 cm. It therefore seems likely that these clusters are formed by agglomeration of smaller particles that accumulated in the top layer of the hot metal. Their presence indicates that the MgS particles have not completely been washed out to the slag layer. With their experiments Lindström et al.[1] found clusters of MgO-MgS, approximately 150 µm in size, close to the upper surface of the hot metal bath. The cluster in Figure 3-10 is in the same size range and was found also close to the upper surface of the bath. The difference from their observations is that the element mappings in Figure 3-10 do not give an indication for the presence of oxygen in the cluster that would point to MgO.

3.3.3 Ti(C,N)

In Figure 3-9 and Figure 3-10 Ti(C,N) particles are deposited on the interface of the lime particles with the hot metal. These are also present as separate particles in the solidified hot metal matrix but in lower concentrations compared to the particle/hot metal interfaces. Detailed analysis indicates the Ti(C,N) is enriched with vanadium. Particles of the same type were found in the hot metal samples taken from the hot metal bulk, see Figure 2-4 and Figure 2-8 in Chapter 2.

Ender et al.[2] studied slag samples taken from the hot metal desulphurisation process, after injection of reagents. They also found a border of Ti(C,N) particles surrounding an iron droplet dispersed in the slag. Koros et al.[3],[4] have described the effect of ilmenite addition to the blast furnace burden on the steelmaking processes. During the hot metal desulphurisation, the hot metal cools down which causes significant amounts of Ti(C,N) particles to float out of the iron gathering at the underside of the slag. Titanium compounds decrease the surface tension between hot metal and slag.[5] This agrees with their preferential presence on the hot metal/slag interface as shown in Figure 3-9 and Figure 3-10 which, in general, leads to a diminishing of the surface tension between phases. The effect of the Ti(C,N) particles on the process is further discussed in 3.5.4.

3.3.4 CaO/CaS particles

Several examples of lime particles covered with a CaS product layer haven been shown. The product layer is enriched with SiO_2 or MgO or both. This confirms reactions (2), (3) and (4) as described in section 1.3 take place on the surface of the lime particles. In some examples MgO has penetrated into the CaO particles deeper than the CaS product layer. Due to calcium's greater affinity to oxygen, CaO can not be reduced by magnesium.[6]

A possibility for the formation of the MgO layer could be that some calcium hydroxide was present on the lime particle which can react according to: [6]

$$Ca(OH)_2 + Mg_g = CaO_s + MgO_s + H_2 \quad (27)$$

The CaO particles found in these samples present a small fraction of the 400 kg of fluidised lime that has been injected. It is expected, however, that the same reactions have occurred on the bulk of the injected lime particles.

In Chapter 2 the analysis of more than ten hot metal samples is described. These were taken from a depth of 60 cm below the top layer. In each of these samples the number of particles composed of (Mg,Mn)S/Ti(C,N)/Ti_8S_3 ranges from 800 to 2000, see Table 2-7. In the same samples none to, at the most three CaO- or CaS-containing particles were found, see Table 2-11. By contrast, in the two samples taken from the top layer, CaO/CaS containing particles are found in high concentrations.

The lime particles found, however, are larger than the particles that have been injected into the hot metal. According to the material specifications the average size of lime particles is 75 µm with a maximum of 90 µm. Since the large particles are covered by CaS and no sulphur is found inside the particles, the particles must have been formed by agglomeration before getting into contact with the hot metal. Another possibility would be that a fraction of the injected particles was larger than the specifications.

In their laboratory scale measurements, described in more detail in section 2.1, Lindström et al.[1] also found larger lime particles of about 300 µm. These were not present before contact with the hot metal and did not contain CaS in the interior. Therefore, they also concluded that these result from rapid agglomeration before the smaller particles react with sulphur.

Larger particles are expected to be easier removed by flotation than smaller particles due to their higher Stokes velocity. The current observations show the contrary: no small lime particles have been found in the hot metal bulk and top layer whereas larger lime particles are found in the top layer. Smaller lime particles must overcome relatively more surface energy to pass the gas/hot metal interface at the point of injection due to their higher specific surface area. The occurrence of larger lime particles dispersed in the hot metal indicates these had sufficient kinetic energy to pass the gas/hot metal interface as they were injected into the hot metal. However, their absence in the bulk of the hot metal bath during the injection process indicates these particles are immediately washed out as the hot metal flow entrained with the bubble plume reaches the bath surface. A fraction of these larger lime particles has remained in the top layer of the hot metal and was not absorbed into the slag layer.

As a consequence, the absence of smaller lime particles in the hot metal could indicate these did not get dispersed in the hot metal but remained in the gas bubble. It does not imply that these particles can not take part in desulphurisation. During their travel upward in the hot metal bath, bubbles continuously break-up into smaller bubbles and coalesce back to greater spherical cap bubbles. The bubble surface is thus continuously renewed and the powder is mixed. Reaction between dissolved sulphur and lime can take

place on the bubble/gas powder interface. From the current measurements, however, this cannot be confirmed.

CaC_2 formation

With combined injection of lime and magnesium the lime particles are exposed to low oxygen activities due to deoxidation by magnesium. This could even favour the formation of CaC_2 according to the analysis of the thermodynamic equilibrium by Irons and Celik.[7] To investigate whether this occurs, element mappings of Ca and C have been combined as shown in Figure 3-11 and Figure 3-12.

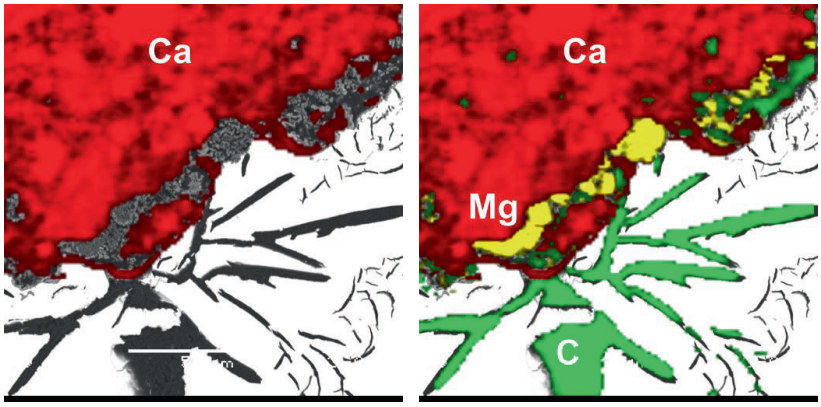

Figure 3-11. SEM-EDS element mappings of Ca, C and Mg of the sample area shown in Figure 3-9.

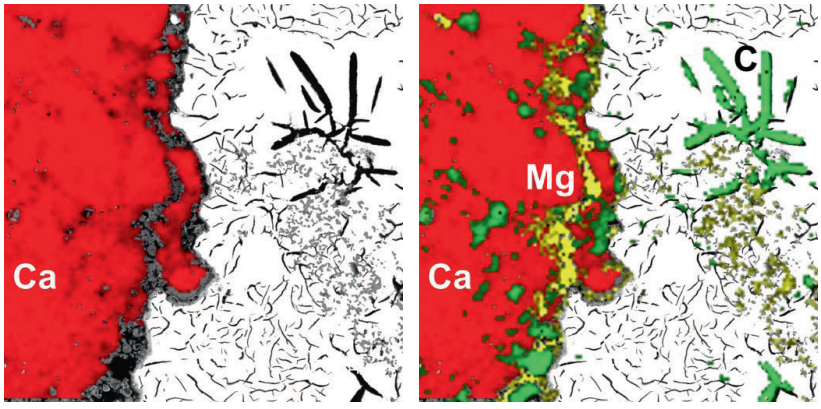

Figure 3-12. SEM-EDS element mappings of Ca, C and Mg of the sample area shown in Figure 3-10.

In both figures, carbon is either detected in the graphite segregates in the solidified hot metal or it is detected in the area of the lime particle where no Ca is detected. With CaC_2 as a compound Ca and C would be detected simultaneously in slightly lower intensity than the pure elements. This could not clearly be detected so no clear indication for the formation of CaC_2 is found.

CaO.FeO

Talballa et al.[8] studied the product layer on a CaO surface in contact with hot metal with 4.25 wt% C and less than 0.02 wt% Si. They found a product layer composed of CaS and CaO.FeO is formed, covered by a second product layer composed of iron oxides and calcium-ferrites. This could indicate that oxygen generated on the CaO reaction interface diffuses back through the product layers to the liquid iron where it reacts with iron. To investigate if this has occurred, the element mappings of Ca and Fe from Figure 3-9 and Figure 3-10 have been combined in Figure 3-13.

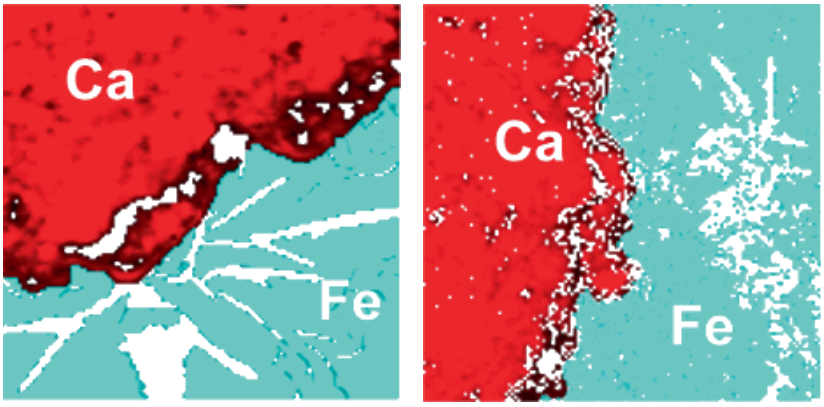

Figure 3-13. SEM-EDS element mappings of Ca and Fe.

In both figures no overlap of Ca and Fe is detected that would indicate the presence of CaO.FeO. In addition, the EDS line-scan of the product layer in Figure 3-8 also indicates a sharp separation between these elements. It therefore seems no CaO.FeO has been formed. Due to magnesium's greater affinity to oxygen compared to iron, this will be the main deoxidant and either pure MgO or CaO.MgO will form as shown in the figures in this section.

3.3.5 Slag layer

The interface of hot metal and slag is irregularly shaped and contains pores, indicating that iron and slag were, at least partially, solidified at the instance of sampling. Figure 3-14 shows an optical microscopic image of the area indicated in the upper part of Figure 3-3. In the slag phase numerous iron droplets are dispersed. Figure 3-15 shows a close-up of the centre region of Figure 3-14 indicated by the white rectangle. In the iron droplets a grey phase is observed. SEM/EDS measurements indicate this is pure MgS or (Mg,Mn)S solid solution. These clusters are seen in the greater fraction of the large irregularly shaped iron droplets in Figure 3-14. Furthermore, (Ca,Mn)S segregates are present in the solidified slag.

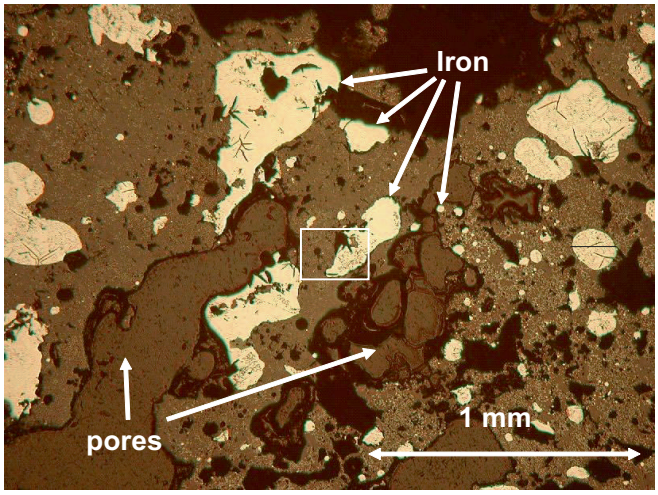

Figure 3-14. Slag with dispersed iron in the middle of sample B-1, taken before slag raking.

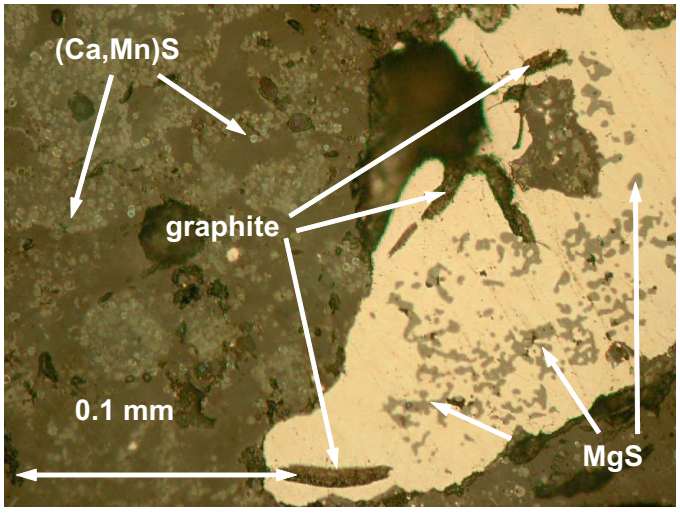

Figure 3-15. Close-up on slag phase with (Ca,Mn)S segregations and iron droplet with MgS clusters.

Figure 3-16 shows globular iron droplets in the slag phase of sample A-1 on the same scale as Figure 3-15. In the iron droplets the dendrite structure is recognised. The graphite segregates are smaller than those in the large, irregularly shaped droplets. Furthermore, no MgS is present in these smaller droplets. In this image (Ca,Mn)S segregates are also present in the slag phase.

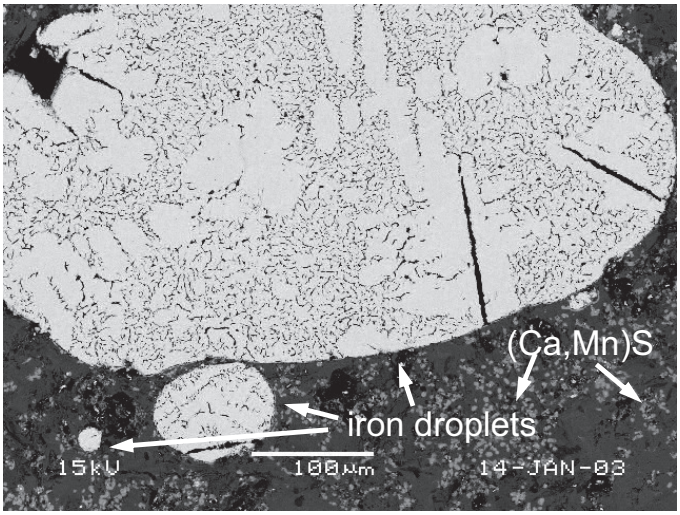

Figure 3-16. SEM-BS image of iron droplets in slag, sample A-1

Previous figures show that the slag contains considerable amounts of dispersed iron droplets. Two types of droplets can be distinguished: globular iron droplets with sizes ranging from 5 to 200 µm and irregularly shaped droplets with sizes ranging from 30 µm to 3 mm. Particularly these large droplets contain clusters of pure MgS or (Mg,Mn)S solid solution. The irregular shape of the larger iron particles could indicate these were, at least partially, solidified before dispersion in the liquid slag. The dispersion of iron droplets is further discussed in section 3.5.

Figure 3-17 shows an image of the slag phase with an iron droplet in sample A-1. On the right-hand side the EDS line scan along the indicated line is shown where iron, (Ca,Mn)S and two slag phases can be distinguished.

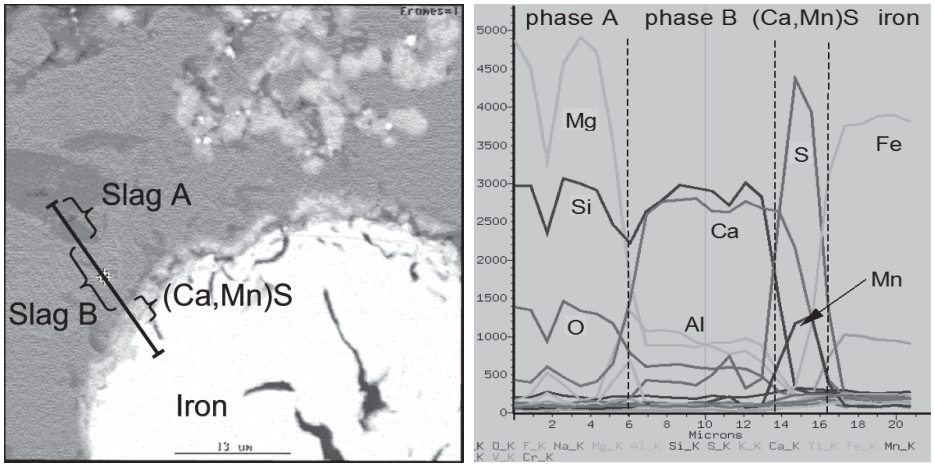

Figure 3-17. SEM-image and line scan of the slag layer in Sample A-1.

(Ca,Mn)S is present as individual segregates in the slag layer but also as a layer on the iron droplet. With EDS spot measurements the average concentrations of both slag phases are determined as given in Table 3-2. It may be noted that the measurement results are presented as oxides and sulphur thus is given as pure sulphur.

Table 3-2. Average composition of slag phases (wt%).

compound	phase A	phase B
Al_2O_3	0	8
CaO	5	30
MgO	50	17
MnO	2	1
SiO_2	43	38
TiO_2	0	5
S	0	1
sum	100	100

Calculation of thermodynamic equilibrium using FactSage shows phase A probably is 2(MgO,MnO,CaO).SiO_2 with small amounts of MnO and CaO. For phase B no single phase could be identified. In Phase A no dissolved sulphur is found. This could indicate that upon solidification of the liquid slag this phase is formed first. With further solidification (Ca,Mn)S segregates from the high sulphur liquid slag.

For comparison the average composition of the slag layer after injection is estimated. Based on the following assumptions, and using the data from Table 3-1, the average composition of the slag layer after injection is calculated (Table 3-3):

- It is assumed that 200 kg of SiO_2 is generated during the injection process. For this heat the decrease in Si-content was not measured but this amount is the average of the measurements as described in section 2.3.2 - Table 2-3.
- Before injection, 500 kg blast-furnace slag carry-over is present on the hot metal. The estimated composition is given in Table 3-4.

As will further be explained in section 3.3.6:

- Sulphur removed from the hot metal by formation of MgS and CaS eventually ends up in the slag layer as (Ca,Mn)S with equal mass fractions of both sulphides.
- It is assumed all injected magnesium eventually ends up as MgO in the slag layer.
- CaO injected in excess is present as CaO in the slag layer.

The results are given in Table 3-3 and Table 3-4.

Table 3-3. Calculation of the slag composition.

mass of hot metal	(t)	307	generated with injection:		
S_{in} - S_{out}	(ppm)	410 - 113	CaO	(kg)	326
sulphur removed	(kg)	91	(Ca,MnS)	(kg)	224
CaO injected	(kg)	413	MgO	(kg)	225
Mg injected	(kg)	136	SiO_2	(kg)	200

Table 3-4. Estimated slag composition before and after injection.

	before injection (wt%)	after injection (wt%)
Al_2O_3	17.3	8.8
CaO	36.3	34.9
(Ca,MnS)	2.4	12.6
MgO	11.0	17.0
SiO_2	33.0	26.8

Although no detailed over-all composition of the slag phase in the top layer samples can be derived from the microscopic images, the estimated over-all slag compositions agree with the observed concentrations of the compounds.

In samples A-1 and B-1, segregates composed of (Ca,Mn)S solid solution are observed throughout the slag phase. Their small size indicates these were formed upon solidification of the liquid slag. EDS spot analyses indicate an average composition of $(Ca_{0.54},Mn_{0.46})S$, thus approximately equal amounts of both sulphides. According to the measurements by Leung and Van Vlack, [9] CaS and MnS form a completely miscible solid solution between 1125 and 1500 °C. This indicates the temperature of the slag was above 1125 °C at the instance of sampling. Upon sampling this sulphide phase segregated from the liquid slag and cooled down quickly enough to freeze the sulphide phase.

3.3.6 Absorption of MgS into the slag

Figure 3-18 shows an image of the slag in sample A-1 with iron droplets and (Ca,Mn)S segregates. The other images show the combined element mappings of Ca, Mg, O and S. The colours of the elements combine as shown in Figure 3-7.

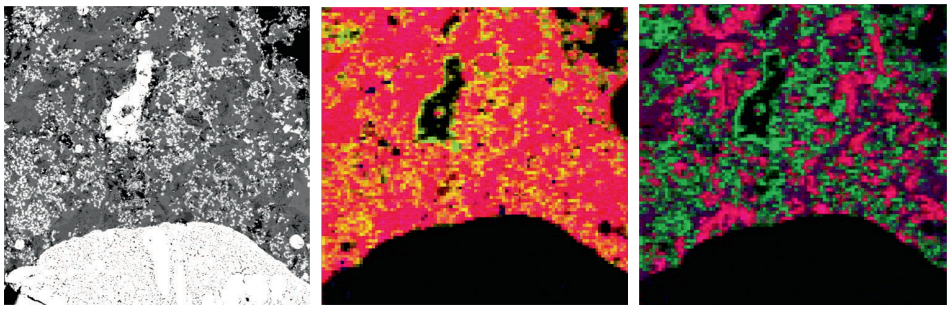

SEM-BS Ca:■, S:■, O:■ Mg:■, S:■, O:■

Figure 3-18. SEM-image and combined element mappings of Ca, Mg, O and S of area in the slag layer in Sample A-1.

In the centre image the (Ca,Mn)S segregates are yellow. The green layer surrounding the smaller iron droplets is an indication for (Ca,Mn)S with a high Mn-content. The slag phase surrounding the segregates and the iron droplets is purple indicating the presence of CaO. In the rightmost image, MgS would appear yellow but this is not present. Instead, two shades of purple can be seen. The lighter, violet fraction indicates slag with higher MgO content. The darker, more bluish fraction indicates slag with lower MgO content. This coincides with the two phases shown in Figure 3-17 and Table 3-2.

Figure 3-19 shows the image and element mappings of another area in the slag layer in sample A-1. The colours of the elements combine as shown in Figure 3-7.

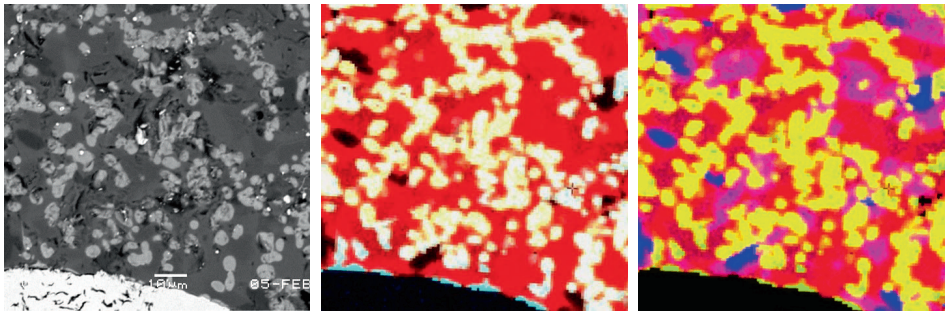

SEM-BS Ca:■, S:■, Mn:■ Ca:■, S:■, Mg:■

Figure 3-19. SEM-image and combined element mappings of Ca, Mg, Mn and S of area in the slag layer in Sample A-1

In the centre image, (Ca,Mn)S is white to light blue and the slag phase is red. In the right image (Ca,Mn)S is yellow. MgS would appear as light blue but this is not present. The

colour of the slag phase ranges from red to violet to blue corresponding to variation in CaO and MgO content.

With additional EDS spot-analyses on both samples neither MgS, (Mg,Mn)S nor pure CaS or pure MnS was found in the slag. Sulphur was only present in the form of (Ca,Mn)S with varying composition.

As described in section 2.4.3, during the injection of magnesium into the hot metal MgS particles are formed in situ in high concentrations. These are subsequently washed out to the slag layer. In the slag layers of samples A-1 and B-1, however, no MgS is found and sulphur only is present in the form of (Ca,Mn)S segregates. This is explained by the following. MgS and CaS particles formed by the desulphurisation reactions in the hot metal bath are washed out and absorbed into the liquid slag layer. With the solidification of the slag samples (Ca,Mn)S forms as a solidification product.

With their experiments on laboratory scale, Yang et al.[10] found that resulphurisation of hot metal took place after the injection of magnesium vapour was finished. To further study this phenomenon experiments were done with MgS, CaO, C, and CaS powders added to the surface of the iron melt. They found that, depending on temperature and oxygen partial pressure, up to 71 % of the sulphur content of the added MgS powder dissolved into the iron melt in a period of 60 minutes. Addition of equal amounts of CaO and MgS powder on the melt surface resulted in approximately half of the final sulphur content. While CaS has higher stability than MgS it is considered the following reaction takes place on the surface:

$$MgS_{(s)} + CaO_{(s)} = MgO_{(s)} + CaS_{(s)} \quad (28)$$

Addition of a tenfold amount of CaO powder led to almost complete repression of resulphurisation. These results confirmed CaS has much higher stability than MgS even under oxidizing conditions.

With the industrial process the conditions are somewhat different. First of all, lime powder is injected simultaneously with the magnesium. Furthermore, SiO_2 is generated during the injection process as described in section 2.3.5. Finally, some blast-furnace slag carry-over can be present on the hot metal. Reversal of sulphur, however, can also be observed. The experiments performed by Yang et al.[10] indicate that sufficient CaO must be injected together with Mg to prevent sulphur reversal. With the industrial heats CaO was added in an approximate threefold of the amount of Mg. In the extreme case where all injected Mg is first converted to MgS, this would correspond to 30 % more CaO than MgS. According to the results from Yang et al. the reversal of sulphur could be further minimised by further increasing the CaO content of the slag.

From the current observations and conformed by the experimental results from Yang et al. it is concluded that with industrial hot metal desulphurisation a slag with sufficient CaO-content is required for proper absorption of the sulphides and prevention of sulphur removal. The minimum lime to magnesium ratio, when all injected lime properly reacts with MgS, would be one mole of CaO per one mole of lime. This corresponds to lime/magnesium ratio of 2.3/1. In practice, mixing will not be perfect so a higher ratio is required.

3.3.7 Crumbly top layer

The samples from the uppermost layer, taken in addition to the hot metal/slag samples, have been analysed by G. Dörsam [11].

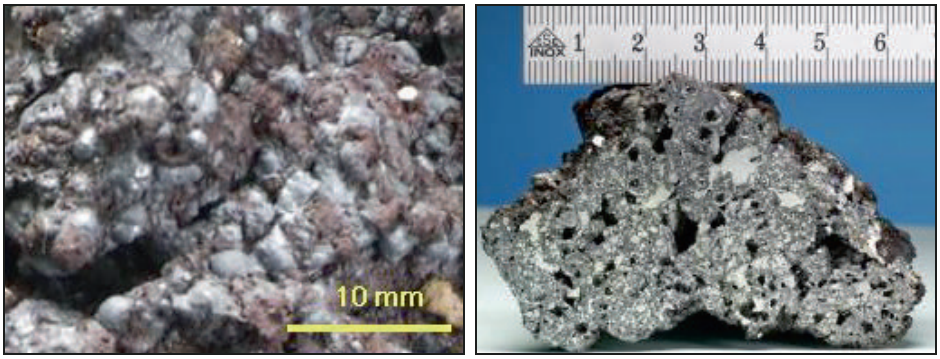

Figure 3-20. Outer surface and cross-section of top slag sample taken from Heat 1 [11].

Figure 3-20 shows pictures from one of the samples. Globular metal droplets set in slag parts can clearly be recognised. The cross-section indicates a high metallic content of the sample. Microscopic analysis of the sample resulted in the same observations as described in section 3.3.5 but, in addition, pure CaO particles of 10 to 20 µm in size were found embedded in the solidified slag phase. This indicates saturation of the slag with CaO. Dörsam explains this by the change in slag composition during the injection process. Initially the slag layer consists of liquid blast furnace slag. During the injection process the CaO content increases up to the level that the liquidus of the slag lies above 1600 °C, temperatures not attained with hot metal desulphurisation.

3.4 Top layer after slag removal

3.4.1 Residual MgS particles

Two samples were taken from the top layer of the hot metal bath after slag raking. Figure 3-21 shows a cross section of sample B-2 composed of a series of optical microscopic images. In samples A-2 and B-2 only some small droplets of slag are present on the upper surface indicating the slag layer was removed properly.

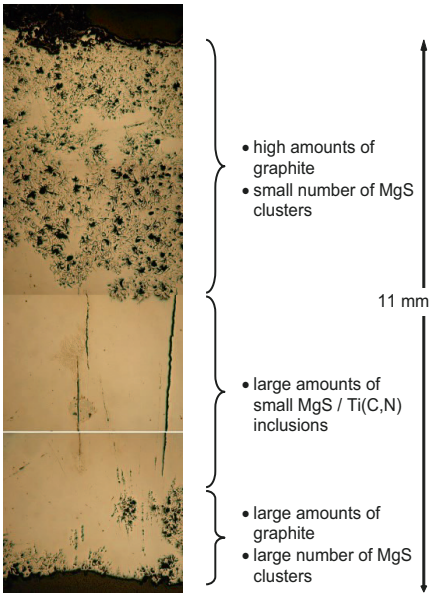

Figure 3-21. Cross section of sample B-2

As indicated in Figure 3-21, three regions can be recognised in this sample. These regions are also present in Sample A-2. In the uppermost 5 mm a high concentration of relatively large graphite segregates can be seen. This layer contains low concentrations of clusters of MgS. In the layer beneath no graphite segregates are seen but this layer contains high amounts of MgS particles. As an example, Figure 3-22 shows an SEM image of the centre part of sample A-2 together with the combined EDS-element mappings of Mg, S and Ca. The colours of the elements combine as shown in Figure 3-7.

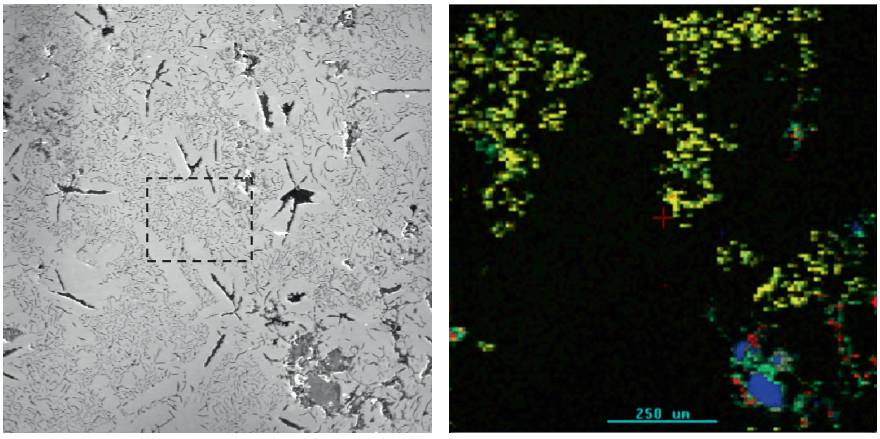

SEM-BS Mg:■, S:■, Ca:■

Figure 3-22. SEM-BS-image and combined element mappings of Mg, S and Ca of Sample A-2, taken after slag raking.

The graphite segregates are smaller than those in the upper 5 mm of the sample. The MgS particles appear as yellow spots in the composition plot. Because the resolution of the element mappings is lower than the BS-image the MgS spots are enlarged in the picture. MgO (red) is not present in these clusters of MgS particles. In the lower-right corner clusters of CaO (blue), CaO (green) and MgO (red) is present. This resembles the phases found in the iron phase of the samples taken before slag removal, as shown in, for example, Figure 3-6.

Figure 3-23 shows the region indicated by the dotted line in Figure 3-22 at higher magnification. Besides graphite segregates clusters of MgS are found in the iron matrix. For clarity this phase is coloured yellow. These clusters have been found throughout sample A-2 and B-2 and are similar to those found in the top layer samples taken before slag removal, as shown in Figure 3-4 and Figure 3-10. It can be assumed these are present everywhere in the top layer of the iron bath.

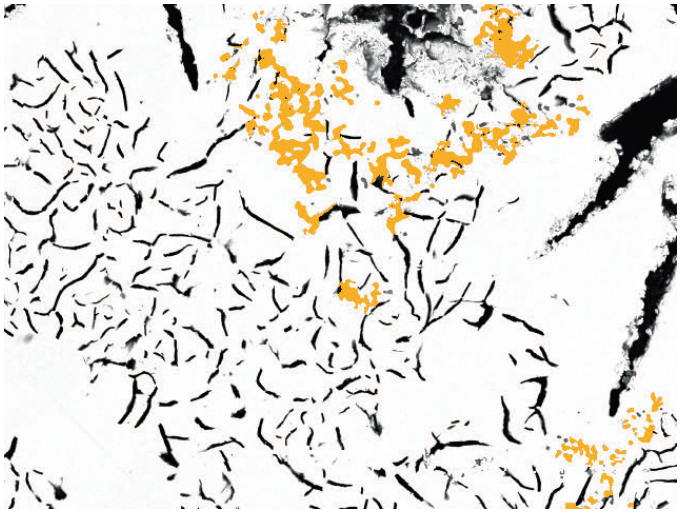

Figure 3-23. SEM-BS image of clusters of MgS (yellow) in sample B-2 taken after slag raking.

3.4.2 Effect on total sulphur content

These clusters present an extra sulphur content in the hot metal that is not measured with chemical analysis of hot metal samples that are taken from a depth of 60 cm. After slag removal the hot metal is charged into the oxygen steelmaking converter where these clusters are oxidised to sulphur and MgO. This may contribute to the, on average 70 ppm sulphur pick-up mentioned in section 1.3. The contribution of these clusters to the total sulphur content depends on their concentration and the thickness of the layer in which they are present. The thickness of the sample is 11 mm and the clusters are present throughout the sample. Without further image processing, the surface fraction of MgS clusters in the images is estimated as 1 %. With densities for MgS and hot metal of 2840 and 6800 kg/m^3, this accounts for 0.42 wt% of MgS or 0.2 wt% of sulphur. The average of the sulphur contents of the hot metal samples taken from the investigated heats was 110 ppm (Table 3-1). Table 3-5 gives the total effective sulphur content of the hot metal ladle

for a range of thicknesses of the MgS cluster containing top layer. It is clear these residual MgS clusters can contribute to the total sulphur content of the hot metal ladle and the sulphur pick-up observed with the converter process.

Table 3-5. Total sulphur content with 0.42 wt% MgS in the top layer for varying top layer thicknesses.

thickness of top layer (cm)	average sulphur content (ppm)
0	110
1	115
2	120
5	134
10	158

3.4.3 Explanation for residual MgS

The question remains why the MgS clusters have not completely been washed out. The following explanation is given for this.

Two types of graphite segregates appear in the hot metal phase in the samples taken before and after slag removal:

- Large segregates, often observable to the naked eye, randomly distributed in the hot metal, as for example in Figure 3-10 and Figure 3-15. These are also present in the large irregularly shaped hot metal droplets dispersed in the slag that also often contain clusters of MgS.
- Microscopic small segregates, often present in a dendrite structure, as for example in Figure 3-16. Their dendrite structure indicates these have been formed with the solidification of the sample.

Hot metal, tapped from the blast furnace, contains more than 4 wt% dissolved carbon. During the subsequent handling, including tapping from the torpedo into the hot metal ladle, transport from the desulphurisation station to the converter and charging into the converter, graphite dust, known as “kish” escapes from the hot metal surface. See for example Figure 3-24.

Figure 3-24. Graphite dust escaping from a hot metal ladle after slag removal.

Hot metal exposed to the air at the surface cools down and the solubility of carbon decreases resulting in the formation of graphite. Also during the injection process heat is lost at the top layer. As described in 2.3.5, Kishimoto et al.[12] found that in a gas-stirred ladle only less than 1 % of the stirring energy is dissipated at the upper surface outside the spout zone. The convective heat transfer from the hot metal bulk thus is poor and the temperature of the top layer decreases due to exposure to the environment.

Liquid oxide slag does not wet graphite. Increasing the FeO content of the slag, however, results in an improved wetting. This can be explained by the change in interfacial energy brought about by the interfacial reduction reaction of FeO with carbon. This is described by for example K. Nakashima and K. Mori [13], Shen et al.[14] and Siddiqi et al.[15][16] The oxygen activity in hot metal and blast furnace slag is low due to the high carbon and silicon content [17]-[19]. This is even lowered further by the injection of magnesium. Carbon-rich to –saturated hot metal does not wet graphite due to the absence of interfacial dissolution reaction of carbon. The graphite segregates in the top layer thus are can be expected to be non-wetting to the slag layer floating on the hot metal. This promotes accumulation of these segregates in the top layer. Pure liquid iron wets graphite.

It is postulated that during the injection process the large graphite segregates were formed in the top layer of the hot metal, as shown in Figure 3-21. These have obstructed the MgS particles from further rising and being absorbed into the slag layer. This has taken place at the surface area outside the spout area. The large, irregularly shaped iron particles with large graphite segregates and MgS clusters found in the slag have probably been ripped from the top layer at the edge of the spout area. The small, rounded iron particles with small graphite segregates and no large MgS clusters have probably been formed from hot metal entrained with the bubble plume. This hot metal was not cooled down before reaching the spout area so large graphite segregates and MgS clusters are not present in these particles.

In addition to the graphite segregates, Ti(C,N) particles were found in the hot metal just beneath the large graphite segregates, see Figure 3-21. As discussed in 3.3.3 Koros et al.[3],[4] concluded that with hot metal desulphurisation significant amounts of Ti(C,N) particles float out of the iron gathering at the underside of the slag creating a sticky slag. This coincides with the current observations. These Ti(C,N) particles also form an obstruction for the MgS particles rising towards the surface.

According to Table 3-5 the contribution to the total sulphur content can be considerable. According to the suggested mechanism, the absorption of MgS is promoted by high hot metal temperatures, low titanium and low carbon contents. Since, at BOS No.2 the carbon content is not measured on a regular basis, this cannot be assessed. Additional stirring is expected to be less effective due to low fraction of mixing energy available outside the spout area.

3.5 Iron dispersion in the slag layer and hot metal loss

3.5.1 Hot metal loss

The figures in sections 3.3.5 to 3.3.7 show that after the injection process the slag layer contains considerable amounts of dispersed metallic iron droplets. With slag raking, the slag, including these iron droplets is removed. To provide the process model of the oxygen steelmaking converters at BOS No.2 with accurate input data, the hot metal ladle mass is measured before and after the desulphurisation process. As a result it is estimated that with desulphurisation the total loss of hot metal can amount to up to 2 %. The costs accompanied with this production loss exceed the costs of the injected reagents. This hot metal loss can be attributed to two factors: loss of iron dispersed in the slag that is raked off and entrainment of liquid hot metal with the raking. For comparison, Magnelöv et al.[20] collected slag samples before slag raking from 33 hot metal desulphurisation heats at SSAB Tunnplåt. The average iron content in the slag samples was determined to be 60 % which accounts for 1.7 % of the hot metal treated. This is excluding losses due to raking.

In the following section, an explanation for the high amount of iron dispersed in the slag layer is given.

3.5.2 Entrainment of hot metal droplets

Several references describe the entrainment of iron occurring when a bubble passes the interface between hot metal and molten slag.[21]-[25]. Han and Holappa[21],[22] studied the phenomena occurring during passage of gas bubbles through the iron/molten slag interface. These experiments were performed with low carbon iron and completely liquid Al_2O_3/CaO slag in a crucible measuring 35 mm in diameter and 60 mm in height. Their observations were as follows. When the bubble reached the interface it was lifted and an iron dome was formed. As the bubble rose further into the slag this iron film got thinner. Finally the iron film ruptured and the bubble entered the slag phase, immediately pulling an iron jet into the slag. Two distinct groups of droplets were formed this way: fine droplets, usually smaller than 10 µm, resulting from the rupture of the metal film and large droplets, typically 1-3 mm, resulting from the entrained jet. During their decent through the slag the large iron droplets were not spherical but were dragged into an

irregular shape by viscous force. When the gas flow rate was increased, a bubble column or foam was formed. A succeeding bubble could push the previous bubble upwards in the slag before it ruptured. This resulted in an iron ring in between the bubbles from which a large iron droplet could form. It is assumed that the large droplets formed by this "ring" mechanism are non-spherical during their descent as well.

The industrial hot metal desulphurisation conditions often differ from the experiments performed by Han and Holappa. The two classes of dispersed iron droplets as described by them, however, coincide well with the current observations: globular iron droplets with sizes ranging from 5 to 200 µm and irregularly shaped droplets with sizes ranging from 30 µm to 3 mm. It therefore seems likely a similar mechanism is acting here as well. With the experiments by Han and Holappa the droplets formed by jet entrainment were irregularly shaped during their descent and coalesced to bigger globules afterwards. With the current observations the droplets have kept their irregular shape, most likely because after formation they solidified in the slag layer.

With industrial desulphurisation, high injection rates are applied to minimise treatment time and promote mixing of the ladle content. This creates a spout area with the gas bubbles bursting to the atmosphere and where the slag is pushed aside. During injection it can be observed that hot metal droplets are thrown up as a result from break-up of the gas bubbles. On the outer side of the spout area the iron droplets fall onto the slag layer. This forms another source for dispersion of iron into the slag.

3.5.3 Settling of hot metal droplets

In the previous sections the mechanism for entrainment of iron droplets into the slag layer was described. In the following, the settling of droplets back through the slag layer is described.

To study the motion of liquid metal droplets in molten slag, Iwamasa and R. J. Fruehan[26] performed X-ray measurements on a laboratory scale furnace. They accurately predicted the settling velocity of liquid steel droplets in molten slag from Stokes' law:

$$v_{Stokes} = \frac{g {d_d}^2 \left(\rho_{metal} - \rho_{slag}\right)}{18 \eta_{slag}} \tag{29}$$

The viscosity of the slag has been estimated by N. Jones [27]. For various process conditions like CaO:Mg ratio, temperature and assumptions for the amount and composition of blast furnace slag present on the ladle, the overall slag composition during the desulphurisation process has been predicted. Using these compositions, the properties of the slag in the course of the desulphurisation process have been calculated. It follows that during desulphurisation the viscosity of liquid slag ranges from 0.9 to 2 Pa·s, depending on the progress of injection, amount of blast furnace slag, and temperature.

As described in 2.3.5, Kishimoto et al.[12] found that in a gas-stirred ladle only less than 1 % of the stirring energy is dissipated at the upper surface outside the spout zone. The convective heat transfer from the hot metal bulk thus is poor and the temperature of the

slag layer decreases due to exposure to the air. This alone already leads to an increase in viscosity but in addition partial solidification further increases the apparent viscosity. The calculated viscosities thus form the lower boundary for the actual slag viscosity and in practice the viscosity can increase to up to 20 Pa·s.

Figure 3-25 shows the settling velocities for a range of slag viscosities and particle diameters calculated using Stokes' Law.

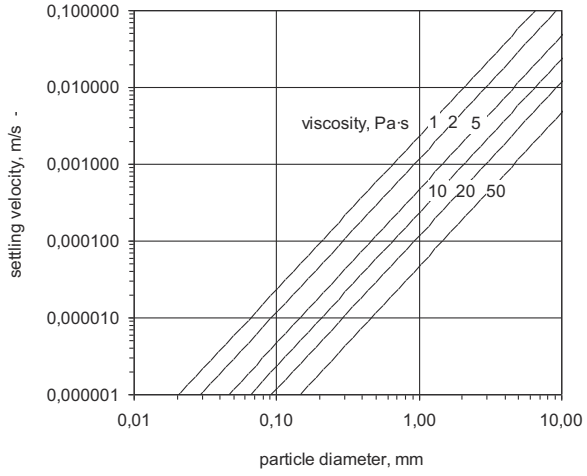

Figure 3-25. Settling velocities of iron particle in molten slag.

The total amount of slag is determined by the amount of injected reagents and the amount of blast furnace slag carry-over. The latter is estimated to be 1000 kg. The amount of slag resulting from the injection of reagents is estimated to be 1000 kg, see Table 3-4. During the injection process the slag mass thus increases from 1000 kg to 2000 kg. With an assumed average density of 2700 kg/m³ and with a ladle diameter of 4 m the thickness of the slag layer increases from 3 to 6 cm during the injection process. For a range of conditions that can be experienced in practice, the settling time required for a hot metal droplet to sink through a slag layer is calculated as given in Table 3-6. For various heats, the injection times range from 3 to 5 min.

The results in Table 3-6 show that only when the viscosity has minimal values, there is sufficient time for particles of 1 mm and larger to sink back through the liquid slag layer to the hot metal. At a higher viscosity, for example 20 Pa·s, these particles may remain dispersed in the slag layer. The time to descend through the slag layer grows quadratic with decreasing diameter, so the particles shown in Figure 3-14 with sizes of 5 - 200 µm will not sink back to the hot metal, even with low viscosity slag. The drag force on the irregularly shaped particles observed in the slag layers is higher than on globular particles. The terminal velocity of these particles thus is lower than globular particles of the same mass. So although these particles can be up to 3 mm in size, the greater part of these particles will not fall back into the hot metal during the injection period. So even when the slag on the hot metal ladle is fully liquid, the viscosity will be too high for particularly the smaller hot metal droplets to sink through the slag layer back into the hot metal

within the period of injection. As more and more iron droplets accumulate in the liquid slag, the apparent viscosity further increases enhancing the accumulation of even the larger droplets.

Table 3-6. Settling times for hot metal droplets in desulphurisation slag.

hot metal density	(kg/m³)	7000
slag density	(kg/m³)	2700
slag thickness	(m)	0.03

slag viscosity	(Pa s)	1	2	5	10	20
particle diameter	(mm)	0,2	0,2	1,0	1,0	1,0
settling velocity	(m/s)	$9{,}4\cdot10^{-5}$	$1{,}9\cdot10^{-5}$	$4{,}7\cdot10^{-4}$	$2{,}3\cdot10^{-4}$	$1{,}1\cdot10^{-4}$
settling time	(s)	312	1572	60	126	254

3.5.4 Accumulation of hot metal droplets

Based on the observations and aforementioned estimations, the following explanation is given for the observed high hot metal content in the, initially fully liquid, slag layer. Figure 3-26 schematically shows the build-up of hot metal in the slag layer during the injection process.

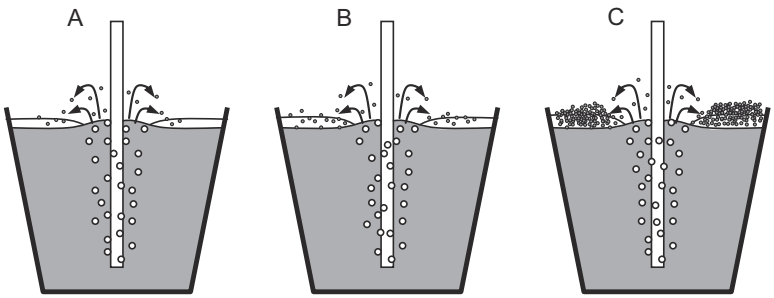

Figure 3-26. Build-up of hot metal droplets in desulphurisation slag.

A. Initially, the hot metal bath is covered with a thin layer liquid slag, primarily composed of blast furnace slag carry-over. The injection of reagents and carrier gas results in the formation of a bubble plume in the hot metal bath. At the surface, hot metal droplets are entrained by gas bubbles into the liquid slag layer. Furthermore, hot metal droplets thrown up from bubbles bursting in the spout area exposed to the air, fall onto the slag layer. The lime powder contained in the bubbles is also released in the spout area as the bubbles burst and this lime adds to the slag layer. The hot metal droplets that have been entrained into the slag and those that have fallen on the slag slowly sink through the slag layer.

B. The rate at which hot metal droplets are added exceeds the rate at which they sink through the liquid slag due to the low settling velocity. Hot metal droplets thus accumulate in the slag. As the injection proceeds, the slag gets saturated with CaO due to the lime injection. This leads to a further increase in apparent viscosity. In addition to this, the viscosity of the liquid slag further increases due to cooling as a result of exposure to the environment.

C. As the injection further progresses, the slag becomes so viscous that all entrained and thrown up iron droplets pile up on the surface, together with slag and injected lime. This results in the solid crumbly upper layer as observed in Figure 3-2 and Figure 3-20. With slag raking, this iron is removed from the ladle resulting in loss of hot metal.

As discussed in 3.3.3 Koros et al.[3],[4] concluded that with hot metal desulphurisation significant amounts of Ti(C,N) particles float out of the iron gathering at the underside of the slag creating a sticky slag. Iron droplets carried up by the gas bubbles are deposited and trapped in this thick, lime-rich underside of the slag layer. This mechanism results in the build up of an iron rich slag from the underside of the slag instead of build up from the upper side. With the current observations Ti(C,N) particles have also been found in the top layer as described in Figure 3-9, Figure 3-10 and Figure 3-21.

According to this explanation, the total amount of iron in the slag after the injection process increases with decreasing hot metal temperature, increasing titanium content and increasing injection period. To validate this, heat data from BOS No. 2 have been analysed as described in the following section.

3.5.5 Factors affecting hot metal loss

At BOS No.2, the mass of the hot metal ladle is measured before the injection process and after the slag raking. The difference is recorded as the hot metal loss. To assess the effects of injection time and amount, hot metal temperature and hot metal titanium content separately, heats with otherwise similar process conditions were collected from a data set of 5000 heats. The properties of the selected heats are given in Table 3-7. Since the same injection rate is used with all heats, heats with the comparable amounts of reagents have comparable injection periods: 4 minutes for 90 kg and 5½ minutes for 144 kg. For all heats, lime was injected with a fixed lime to magnesium mass ratio of 3:1. For every comparison, 50 heats with furthermore equal heat properties were selected.

Table 3-7. Selection parameters for heat data.

hot metal mass	(t)	290
titanium content	(wt%)	0.076 and 0.117 or variable
hot metal temperature	(°C)	variable or 1384
inject amounts of magnesium	(kg)	90 or 144
lime/magnesium ratio	-	3

Figure 3-27 shows the measured hot metal loss versus hot metal temperature for two amounts of injected magnesium and a hot metal titanium content of 0.076 wt%. Figure 3-28 shows the same for a hot metal titanium content of 0.117 wt%.

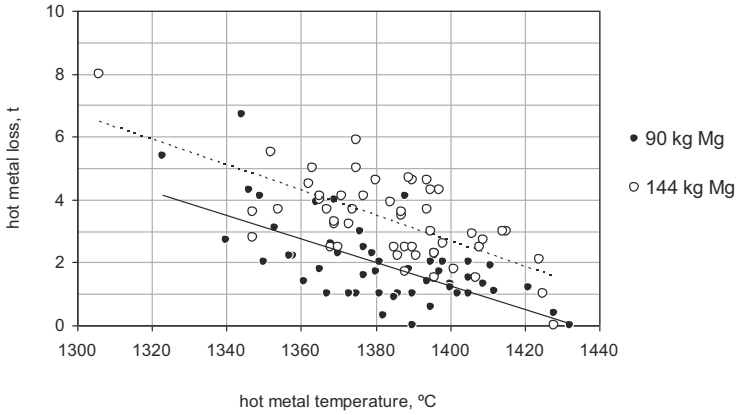

Figure 3-27. Hot metal loss per versus hot metal temperature. Hot metal titanium content is 0.076 wt% and hot metal mass is 290 t.

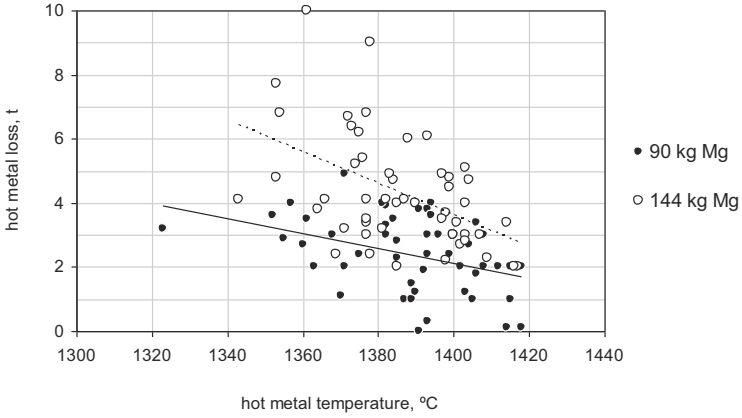

Figure 3-28. Hot metal loss per versus hot metal temperature. Hot metal titanium content is 0.17 wt% and hot metal mass is 290 t.

Blast-furnace slag carry-over varies from heat to heat but is not measured. Therefore, with the calculation of the hot metal loss a value of 1.5 t is used for each heat. Furthermore, the amount of hot metal entrained with the raking is dependant on the condition of the hot metal ladle lip and the slag scraper and the skills of the operator controlling the slag scraper. These variations cause scatter in the figures. An actual slag carry-over of less than 1.5 t can result in 0 t of measured hot metal loss as indicated in the figures.

Notwithstanding the scatter, trends can be recognised: The hot metal temperature has a significant effect on hot metal loss. With increasing hot metal temperature, the hot metal loss decreases. Injection of an extra amount of 54 kg magnesium and 162 kg of lime results in, on average, 1.5 t of extra hot metal loss. Comparing the figures, the hot metal losses are higher with higher the hot metal titanium content. To further clarify the influence of hot metal titanium content, heats with varying titanium content but similar hot metal temperature are compared. The temperature most frequently occurring in the set of heat data is 1384 °C. The results are shown in Figure 3-29.

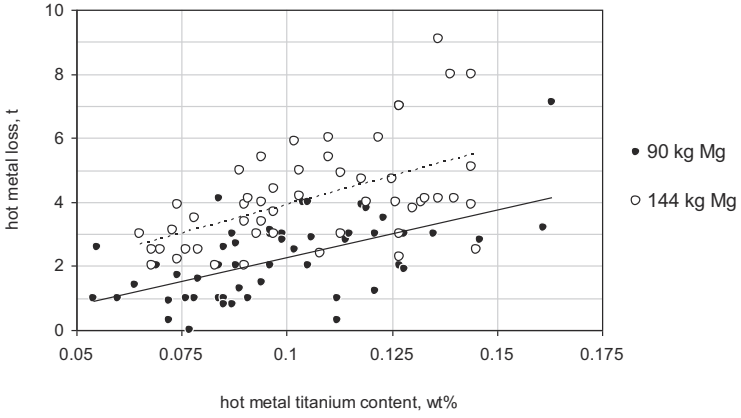

Figure 3-29. Hot metal loss versus hot metal titanium content. Hot metal temperature is 1384 °C and hot metal mass is 290 t.

Figure 3-29 clearly shows the hot metal loss increases with increasing hot metal titanium content. Doubling the hot metal titanium content results in an almost doubling of the hot metal loss.

The influences of hot metal temperature and titanium content and the duration of the injection process on the hot metal loss as predicted in 3.5.4 thus are confirmed by the operational practices in an industrial steel plant.

3.6 Summary and conclusions

Microscopic analysis of samples taken from the top layer of the hot metal bath before and after desulphurisation has resulted in the following conclusions:

- During injection lime particles react with sulphur dissolved in the hot metal. With this a product layer is formed on the particles, composed of CaS and either SiO_2 and/or MgO.
- Upon absorption of MgS particles into the slag layer, MgS reacts with co-injected CaO to MgO and CaS. This prevents the sulphur from reversing into the hot metal by oxidation of MgS by oxygen in the air. CaS dissolved in the liquid slag fraction forms (Ca,Mn)S solid solution segregates upon solidification of the slag.
- The absorption of MgS particles into the slag layer is impeded by graphite segregates and Ti(C,N) particles. This results in residual MgS particles in the top

layer of the hot metal bath. After charging into the converter, this leads to sulphur pick-up with the converterproces.

- The hot metal loss experienced during slag raking after the injection is explained by the accumulation of hot metal droplets in the slag layer. Hot metal droplets entrained by gas bubbles rising through the slag layer and droplets thrown up at the spout area accumulate in the slag layer due to the low settling velocity. From this, it is understood how hot metal temperature and titanium content and amount of injected reagents affect the amount of hot metal lost.

The costs of hot metal desulphurisation for a steel plant can thus be minimised by taking the following into account:

- Lime powder should be injected in a lime to magnesium ratio of at least 2.3 but preferably more to prevent reversal of sulphur from the slag into the hot metal.
- After injection of the required amount of magnesium, the injection carrier gas should continue for a while to achieve proper flotation and absorption of magnesium sulphide in the slag layer.
- To minimise hot metal loss, the hot metal temperature should be as high as possible and the hot metal titanium content should be as low as possible.

3.7 References

[1] D. Lindström, P Nortier and D. Sichen. Functions of Mg and Mg-CaO mixtures in hot metal desulphurisation. Steel. Res. Int. 85 (2014) 76-88.

[2] A. Ender, H. van den Boom, H. Kwast, H. Lindenberg, Metallurgical Development in Steel-plant-internal Multi-injection Hot Metal Desulphurisation. Steel Research int. 76 (2005) 562-572.

[3] S. Street, R. Stone and P.J Koros. The presence of titanium in hot metal and its effects on desulfurization. AISTech 2005 Proceedings - Volume I, May 9-12, 2005, Charlotte, North Carolina, USA , pp. 759-770.

[4] P.J. Koros, S. Street and R.P. Stone. An explanation for the effect on steelmaking of titanium in hot metal. Sohn Int'l Symposium, August 27-31, 2006, San Diego, pp. 571-584.

[5] K. Nakashima and K. Mori. Interfacial properties of liquid iron alloys and liquid slags relating to iron- and steel-making processes. ISIJ Int. 32 (1992) 11-18.

[6] H. J. T. Ellingham. Transactions and Communications. J. Soc. Chem. Ind. 63 (1944) 125-160.

[7] G.A. Irons and C. Celik. Comparison of iron desulphurisation using calcium carbide and lime-magnesium mixtures. Ironmaking and Steelmaking 19 (1992) 136-144.

[8] M. Talballa, P.K. Tojan, W.C. Bigelow, R.A. Flinn and L.O. Brockway. Mechanism of Desulfurization of liquid iron carbon alloy with solid CaC_2 and CaO. Transactions of the American Foundrymen's Society (1976) 775-786.

[9] C.H. Leung and L.H. van Vlack. Solubility limits in binary (Ca,Mn) chalcogenides. Journal of the American Ceramic Society 62 (1979) 613-616.

[10] J. Yang, M. Kuwabara, T. Teshigawara and M. Sano. Mechanism of Resulfurization in Magnesium Desulfurization Process of Molten Iron. ISIJ Int. 45 (2005) 1607-1615.

[11] G. Dörsam. Mineralogical Research on Desulphurisation Slag, Corus RD&T report 109487, 2003.

[12] Y. Kishimoto. Y. Sheng, G. A. Irons and J-S. Chang. Energy Dissipation Distribution In Gas-stirred Liquids,. ISIJ Int. 39 (1999) 113-122.

[13] K. Nakashima and K. Mori. Interfacial properties of liquid iron alloys and liquid slags relating to iron- and steel-making processes - Review. ISIJ Int. 32 (1992) 11-18.

[14] P. Shen, H. Fujii and K. Nogi. Wettability of some refractory materials by molten SiO_2-MnO-TiO_2-FeO_x slag. Materials Chemistry and Physics 114 (2009) 681-686.

[15] N. Siddiqi, B. Bhoi, R.K. Paramguru, V. Sahajwalla and O. Ostrovski. Slag-graphite wettability and reaction kinetics. Part 1 Kinetics and mechanism of molten FeO reduction reaction. Ironmaking and Steelmaking 27 (2000) 367-372.

[16] N. Siddiqi, B. Bhoi, R.K. Paramguru, V. Sahajwalla and O. Ostrovski. Slag-graphite wettability and reaction kinetics. Part 2 Wettability influenced by reduction kinetics. Ironmaking and Steelmaking 27 (2000) 437-441.

[17] S.C. Ghorpade, R.W. Heine and C.R. Loper. Oxygen probe measurements in cast iron. AFS transactions (1975) 193-198.

[18] U.B. Pal and B.V. Patil, Role of dissolved oxygen in hot metal desulphurisation. Ironmaking and Steelmaking 13 (1986) 294-300.

[19] Y.-F. Zhao and G.A. Irons. The role of oxygen in hot metal desulphurisation with calcium carbide. Scaninject V part II, 5th international conference on ladle metallurgy, Luleå, Sweden, June 1989, 63-81.

[20] M, Magnelöv, J. Eriksson, L. Nilsson, J. Drugge. Industrial investigation of iron losses during desulphurisation of hot metal. SCANMET III- 3rd International Conference on Process Development in Iron and Steelmaking, 8-11 June 2008, Luleå, Sweden, Vol.2 pp. 145-146.

[21] Z. Han and L. Holappa. Mechanisms of iron entrainment into slag due to rising gas bubbles. ISIJ Int. 43 (2003) 292-297.

[22] Z. Han and L. Holappa. Characteristics of iron entrainment into slag due to rising gas bubbles. ISIJ Int. 43 (2003) 1698-1704.

[23] G. Reiter and K. Schwerdtfeger. Observations of physical phenomena occurring during passage of bubbles through liquid/liquid interfaces. ISIJ Int. 32 (1992) 50-56.

[24] G. Reiter and K. Schwerdtfeger. Characteristics of entrainment at liquid/liquid interfaces due to rising bubbles. ISIJ Int. 32 (1992) 57-65.

[25] S. Kobayashi. Iron droplet formation due to bubbles passing through molten iron/slag interface. ISIJ Int. 33 (1993) 577-582.

[26] P. K. Iwamasa and R. J. Fruehan. Separation of Metal Droplets from Slag. ISIJ Int. 36 (1996) 1319-1327.

[27] N. Jones. Physico-Chemical Analysis of ROZA Slag. Corus RD&T report 120667, June 2006.

4 Modelling hot metal desulphurisation on an industrial scale

4.1 Introduction

In Chapters 2 and 3 the kinetics of the hot metal desulphurisation reactions have been studied. This has resulted in the following description of the hot metal desulphurisation process:

- Lime powder and magnesium granules are conveyed pneumatically through the injection lance using nitrogen as carrier gas. The gas injection induces a bubble plume and a circulation flow of hot metal through the ladle. This has extensively been described by various authors [3]-[10].
- The magnesium granules heat up and vaporise as the flow exits the lance at the injection ports.
- Sulphur, dissolved in hot metal, reacts with magnesium gas to MgS at the gas bubble/hot metal interface. This is shed off the rising bubble resulting in a suspension of MgS seeds in the hot metal. This mechanism is proposed by Irons and Guthrie [11],[12] and has been confirmed by further investigations as described in Chapters 2 of this thesis.
- In parallel, a fraction of the lime powder particles contacts the hot metal on the bubble interface and reacts to CaS with dissolved sulphur. This is described by, for example Taballa [13], Irons and Celick [14]-[15] and Zhao and Irons [16]. The (partially converted) particles rise to the surface with the bubbles and accumulate in the slag. This results in a CaO-rich slag layer as is described in Chapter 3 of this thesis.
- A fraction of the magnesium vapour dissolves in the hot metal due to the high partial vapour pressure of magnesium in the gas bubbles. This is described by Irons & Guthrie [11], and Yang et al.[17],[18], both referring to the measurements performed by Speer and Parlee [19].
- The suspended MgS seeds distribute throughout the ladle volume where they grow by formation of MgS from sulphur and magnesium dissolved in the hot metal. The sulphide component of theses particles attributes to the measured total hot metal sulphur content. This is described in Chapter 2 of this thesis.
- The suspended MgS particles float to the slag layer induced by the bubble plume. As described in Chapter 3 of this thesis, these particles react with CaO present in the slag layer to CaS and MgO. It is at this stage where sulphur effectively is removed from the hot metal by the injected magnesium. To prevent re-entrainment of sulphur by oxidation of MgS exposed to the atmosphere sufficient CaO must be present in the slag layer. This is also described by Yang et al.[20].

– After the injection, the sulphide-containing slag layer is removed by raking. With this, the sulphur is finally removed from the hot metal charge to the converter. This is described in Chapter 3 of this thesis.

Figure 4-1 shows these governing phenomena and reactions taking place in the hot metal ladle during the injection process.

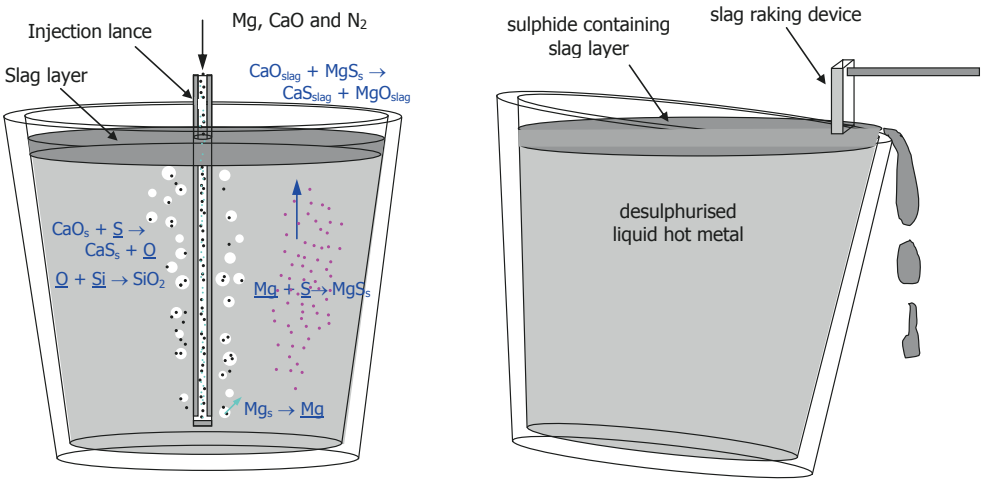

Figure 4-1. Schematic of the hot metal desulphurisation process.

To improve the understanding of the hot metal desulphurisation at BOS No.2, a mathematical process simulation is set up using the description from the introduction.

Parts of this work have been presented at the 3rd ICS, Charlotte USA in 2005 and are published in the ISIJ International vol. 46 in 2006 [1],[2].

4.2 Model set-up

The desulphurisation process is modelled by simultaneously solving the mass balances of the constituents, applying the relevant thermodynamic relations and solving the equations describing mass transfer on the micro and macro scale. In addition to the description given in the introduction, the following approximations and assumptions are applied:

– The hot metal bath is modelled as a well-mixed reaction vessel with uniform composition, operated batch wise, referred to as Batch Reactor (BR), of constant volume and temperature.

– The decrease of silicon content due to reaction with oxygen from the atmosphere, as described in section 2.3.5, is not taken into account.

4.2.1 Plume model

The injected carrier gas and magnesium vapour form a bubble plume in the hot metal. The upward plume velocity determines the residence time of the gas bubbles and the injected lime particles in the bath. From the energy dissipation in the bath by turbulence

and the energy input by the injection of gas, Sahai and Guthrie [3],[4] derived the relation for the upward velocity of liquid and gas in the bubble plume:

$$v_{plume} = 4.5 \frac{\phi_{v,g}^{\frac{1}{3}} L_{im}^{\frac{1}{4}}}{r_l^{\frac{1}{3}}} \tag{30}$$

The gas volume flow is composed of the nitrogen carrier gas and the magnesium vapour:

$$\phi_{v,g} = \phi_{v,N_2} + \phi_{v,Mg} \tag{31}$$

The actual gas volume flow rate changes with the height of the plume due to expansion and dissolution of magnesium. Therefore an average gas flow rate is used. The average pressure in the plume follows from:

$$p_{plume} = p_{atm} + \frac{L_{im} \cdot \rho_{HM} \cdot g}{2} \tag{32}$$

The set point of the nitrogen flow rate is given in standard cubic meters per second. The average actual nitrogen volume flow rate thus is given by:

$$\phi_{v,N_2} = \phi_{v,st,N_2} \frac{T_{HM}}{T_{st}} \frac{p_{st}}{p_{plume}} \tag{33}$$

It is assumed that the injected magnesium granules vaporise immediately at the point of injection. Measurements of the sulphur and magnesium concentrations during the injection process indicate that magnesium does not completely dissolve as described in 2.3.4. Based on the result presented in Table 2-6 a dissolution fraction, f_d of 0.4 is first applied. Assuming the dissolution of magnesium is homogeneously distributed over the plume, the average magnesium volume flow rate is described by:

$$\phi_{v,Mg} = \frac{\dot{m}_{Mg}}{M_{Mg}} \frac{RT_{HM}}{p_{plume}} \left(1 - \tfrac{1}{2} f_d\right) \tag{34}$$

The residence time of the injected powder in the bath is now determined by the plume velocity, given by (30), and the immersion depth of the lance:

$$\tau_p = \frac{L_{im}}{v_{plume}} \tag{35}$$

4.2.2 CaO reactions

The desulphurisation reaction of lime is repeated from the introduction:

$$CaO_{solid} + [S] = CaS_{solid} + [O] \quad (2)$$

The sulphur concentration on the particle-hot metal interface thus will be determined by the oxygen potential on the interface. The two main deoxidants present during hot metal desulphurisation are magnesium and silicon:

$$Mg_{gas} + [O] = MgO_{solid} \quad (3)$$

$$[Si] + 2\,[O] = SiO_{2\,solid} \quad (4)$$

Reaction (3) will than run preferably over (4) due to the higher affinity of magnesium to oxygen. Initially, only silicon is present in the hot metal. The injection process starts with the injection of lime powder only. When 60 kg of lime powder has been injected, the injection of magnesium starts and both reactants are injected simultaneously. When the magnesium injection is finished, the injection of lime is prolonged for some time to achieve complete flotation of magnesium sulphide. In the sampled heats, described in 2.3.1, 730 kg of lime powder was injected. In general the amount of injected lime ranges from 500 to 900 kg. Thus, during the greater part, 88% to 92%, of the lime injection, magnesium is present in the direct vicinity of the lime powder particles, either as vapour or dissolved in the hot metal. Therefore, it is assumed that reaction (3) governs the oxygen activity on the reaction interface of the lime powder particles.

As described in section 2.4.6, only a few MgO particles have been found in hot metal samples taken during the injection process. MgO formed in the plume as result of reactions (2) and (3) thus is kept in the bubble plume and directly transported to the slag layer.

The desulphurisation rate of the injected CaO powder is given by:

$$\left(\frac{d[\%S]}{dt}\right)_{CaS} = -\frac{6 f_{CaO} \dot{m}_{CaO} \tau_p \rho_{HM}}{d_{p,CaO} \rho_{CaO} m_{HM}} k_{S,CaO} \left([\%S] - [\%S]_{CaS}\right) \quad (36)$$

According to Zhao and Irons [16], the fraction of contact of lime particles injected in hot metal can vary between 0.3 and 0.5. For the injected lime particles a uniform diameter of 10^{-5} m is applied.

The mass-transfer between a sphere and it surrounding liquid can be expressed by the Ranz-Marshall equation:[21]-[23]

$$Sh = 2.0 + 0.6 Re^{\frac{1}{2}} Sc^{\frac{1}{3}} \quad (37)$$

For a CaO particle in hot metal the dimensionless numbers are given by:

$$Sh = \frac{k_{S,CaO} d_{p,CaO}}{D_{S,HM}},\ Re = \frac{v_p d_{p,Cao}}{\nu_{HM}},\ Sc = \frac{\nu_{HM}}{D_{S,HM}} \tag{38}$$

For lime particles of this size it can be assumed there is no relative velocity with respect to the surrounding liquid hot metal, i.e. $v_p = 0$, $Re = 0$ and $Sh = 2$.

The mass diffusivity of sulphur is taken from Turkdogan[24] as:

$$D_{S,HM} = 4.9 \cdot 10^{-8} e^{-\frac{36000}{RT}} \tag{39}$$

4.2.3 Magnesium reactions

After dissolution of magnesium vapour into the hot metal, dissolved sulphur and magnesium react on the surface of the MgS seeds according to following reactions.

$$Mg_{gas} \rightarrow [Mg] \tag{40}$$

$$[Mg] + [S] = MgS_{solid} \tag{41}$$

Dissolved sulphur, magnesium and MgS are considered in equilibrium on the surface of the seeds. The concentrations corresponding to equilibrium are expresses by the solubility product as discussed in 2.3.3.:

$$P_{MgS} = [\%Mg]_{MgS} [\%S]_{MgS} \tag{42}$$

The value for the solubility product is determined using the relation described by Turkdogan: [24]

$$P_{MgS} = 1.033 \cdot 10^{-\frac{17026}{T} + 13.161} \tag{43}$$

The molar fluxes of the reactants towards the reaction interface are equal due to stoichiometry and are given by:

$$J_{Mg} = J_S \tag{44}$$

$$J_{Mg} = k_{Mg,MgS} \left([Mg] - [Mg]_{MgS} \right) \tag{45}$$

$$J_S = k_{S,MgS} \left([S] - [S]_{MgS} \right) \tag{46}$$

Analogous to lime particles, for MgS particles it can be assumed there is no relative velocity with respect to the surrounding liquid hot metal so *Sh* equals 2:

$$Sh = \frac{k_{i,MgS}\, d_{p,MgS}}{D_{i,HM}} = 2 \tag{47}$$

The mass diffusivity of sulphur is given by (39). The mass diffusivity of magnesium is taken from Turkdogan[24] as:

$$D_{Mg,HM} = 3.9 \cdot 10^{-8} e^{-\frac{32500}{RT}} \tag{48}$$

The reaction rates of dissolved magnesium and sulphur, in kg/s, are given by:

$$\frac{dm_{Mg}}{dt} = J_{Mg}\, a_{MgS}\, V_{HM}\, M_{Mg} \tag{49}$$

$$\frac{dm_{S}}{dt} = J_{S}\, a_{MgS}\, V_{HM}\, M_{S} \tag{50}$$

Converting molar concentrations to weight percentages, the rates of change of magnesium and sulphur concentrations are given by:

$$\left(\frac{d[\%Mg]}{dt}\right)_{MgS} = -k_{Mg,MgS}\, a_{MgS} \left([\%Mg] - [\%Mg]_{MgS} \right) \tag{51}$$

$$\left(\frac{d[\%S]}{dt}\right)_{MgS} = -k_{S,MgS}\, a_{MgS} \left([\%S] - [\%S]_{MgS} \right) \tag{52}$$

With microscopic analysis, as described in sections 2.4.4 en 2.4.5, it is found that the concentration and size distribution of the MgS particles change during the injection process. The specific surface area therefore also changes. In this model, however, a constant value for the surface area is assumed. From the results described in section 2.4.4 and 2.4.5, a value of 10 m²/m³ is estimated.

Based on the conclusions discussed in sections 2.4.6 and 4.2.2, the formation and growth of MgO particles in the hot metal bath is not considered in this model.

4.2.4 Mass balances

The concentration of dissolved sulphur decreases due to the reactions with lime and magnesium:

$$\frac{d[\%S]}{dt} = \left(\frac{d[\%S]}{dt}\right)_{CaS} + \left(\frac{d[\%S]}{dt}\right)_{MgS} \tag{53}$$

The concentration of dissolved magnesium increases due to dissolution of injected magnesium and decreases due to the formation of MgS:

$$\frac{d[\%Mg]}{dt} = f_d \frac{\dot{m}_{Mg}}{m_{HM}} \cdot 100 + \left(\frac{d[\%Mg]}{dt}\right)_{MgS} \tag{54}$$

After formation of MgS seeds in the plume, the MgS particles accumulate in the hot metal bath where they grow and subsequently float to the slag layer induced by the gas plume. The rate of floatation of the particles follows from growth, agglomeration, the flow pattern of hot metal in the ladle and pickup by the slag. As a first approximation the rate of flotation from the hot metal to the slag is set proportional to the concentration. Residual MgS particles in the top layer, like described in 3.4.1, are not taken into account. The mass balance of MgS in the hot metal thus is given by:

$$\frac{d[\%MgS]}{dt} = -\frac{M_{MgS}}{M_{Mg}}\left(\frac{d[\%Mg]}{dt}\right)_{MgS} - C_f[\%MgS] \tag{55}$$

From the results presented in Figure 2-22 it is estimated that after a 2 minutes period of post injection of CaO and N_2 the MgS content in the bath is approximately halved. This results in a flotation rate constant C_f of 0.006 s^{-1}. It is assumed that flotation is absent when no CaO and N_2 are injected. The total hot metal sulphur and magnesium contents follow from:

$$[\%S]_{tot} = [\%S] + \frac{M_S}{M_{MgS}}[\%MgS] \tag{56}$$

$$[\%Mg]_{tot} = [\%Mg] + \frac{M_{Mg}}{M_{MgS}}[\%MgS] \tag{57}$$

4.3 Modelling results

The set of relations (30) to (57), together with appropriate initial conditions, is simultaneously solved using the Aspen Custom Modeller software package. In the model the injection rates of nitrogen, CaO and Mg can be varied during the process such that the injection schemes as actually applied in the steel plant can be simulated.

For the heats described in section 2.3 the sulphur and magnesium concentrations during the injection process are calculated using the model. The initial conditions are listed in Table 2-2 and Table 4-1. Table 4-2 lists the values initially used for the several model variables as discussed in 4.2. The modelling results were compared to the sulphur and magnesium concentrations measured with XRF (Table 2-3) and the concentrations of MgS measured with AIA (Table 2-9).

Table 4-1. Injection properties of lime and magnesium.

		Heat 1	Heat 2
period of CaO injection	(s)	432	493
amount of CaO injected	(kg)	732	728
injection rate of CaO	(kg/s)	1,69	1,48
period of Mg injection	(s)	320	332
amount of Mg injected	(kg)	117	144
injection rate of Mg	(kg/s	0,365	0,434

Table 4-2. Initial values of model variables.

variable	unit	initial value	optimized value	description
a_{MgS}	(m^2/m^3)	10	7.5	specific surface area of MgS particles in hot metal
$d_{p,MgS}$	(m)	10^{-6}	10^{-6}	diameter of MgS particles in hot metal
$d_{p,CaO}$	(m)	10^{-5}	10^{-5}	diameter of lime particles
C_f	(-/s)	0.007	0.01	flotation rate constant of MgS particles
f_d	(-)	0.4	0.5	fraction of injected Mg that dissolves in hot metal
f_{CaO}	(-)	0.5	0.3	contact fraction of lime powder particles

With the first comparison to the measurement results, it appeared that the rate of flotation of MgS was underestimated. This was adjusted for by increasing the flotation rate constant. Subsequently, the rate of desulphurisation had to be slightly adjusted by lowering the contract fraction of the lime powder particles to a value still within the range indicated by Zhao and Irons [16]. The final optimisation was achieved by adjusting the dissolution fraction of magnesium. The optimised values thus obtained are also given in Table 4-2. The results of the modelling calculations, in comparison to the measurement results for both heats are given in Figure 4-2 and Figure 4-3. The sulphur measurement is regularly calibrated. The 95% confidence interval (± 2 σ) of the measured sulphur contents is guaranteed as 14% of the measured value with a minimum of 8 ppm. The XRF-equipment used is not calibrated for the measurement of magnesium. Due to its lower molar weight, a lower measurement accuracy is expected. The 95% confidence interval of the measured magnesium content is therefore estimated as 25% of the measured value with a minimum of 15 ppm. The 95% confidence intervals are indicated in the figures by error bars. For the MgS-contents, as derived from the AIA measurements, the confidence interval is unknown and no error bars are indicated.

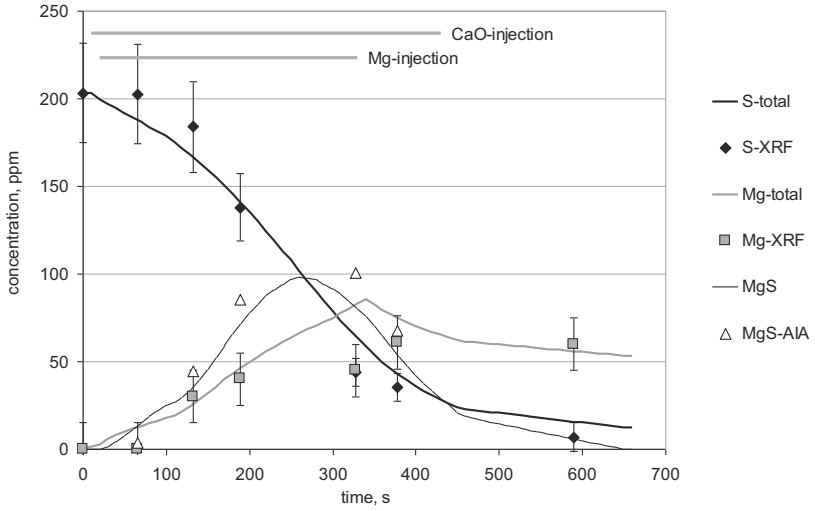

Figure 4-2. Calculated and measured concentrations for Heat 1.

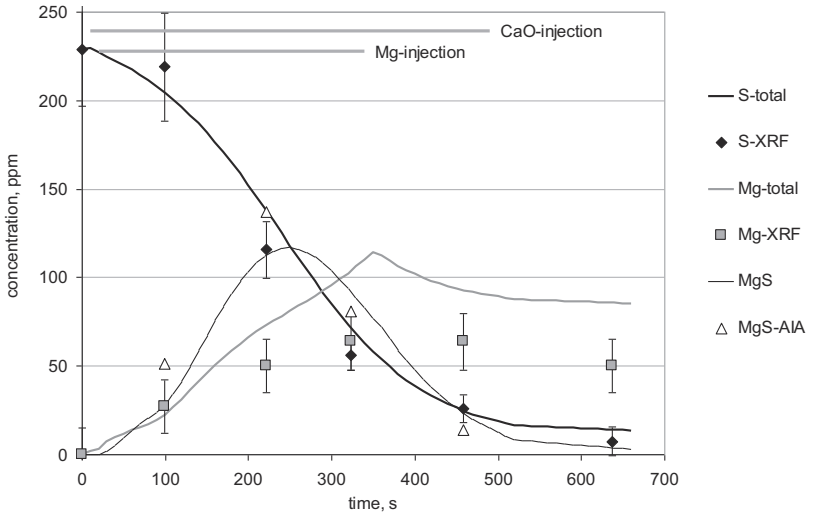

Figure 4-3. Calculated and measured concentrations for Heat 2.

Both figures show good agreement between the predicted and measured concentrations. Only for Heat 2 the concentration of magnesium in overestimated. Most likely, this is due to the XRF-analyser that is not calibrated for this element. Furthermore, the actual solubility product of MgS could differ from the predicted value. For Heat 1, however, the predicted and measured magnesium contents show better agreement and the difference in hot metal temperatures of Heats 1 and 2 is 22 °C so the solubility products will not differ much.

In section 2.3.3 the observed apparent super saturation of hot metal with magnesium and sulphur is discussed and two possible explanations are given for this: reaction rate limitations and accumulation of MgS. Figure 4-4 and Figure 4-5 show the calculated concentrations of sulphur and magnesium and the products of these concentrations.

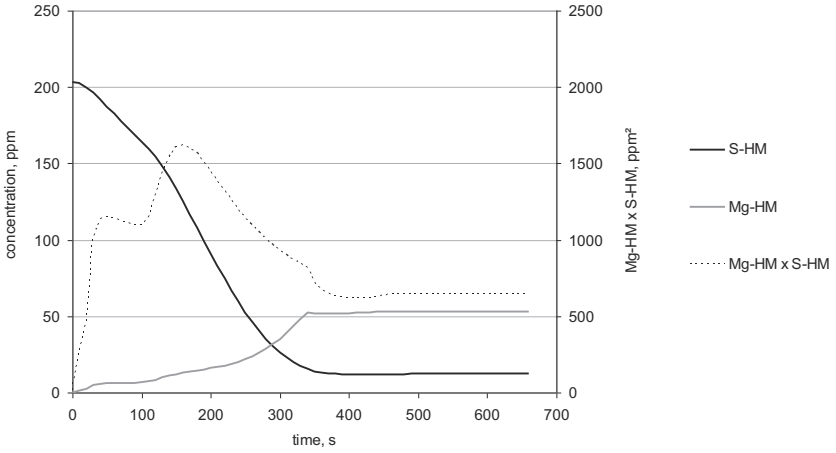

Figure 4-4. Calculated concentrations of dissolved sulphur and magnesium for Heat 1.

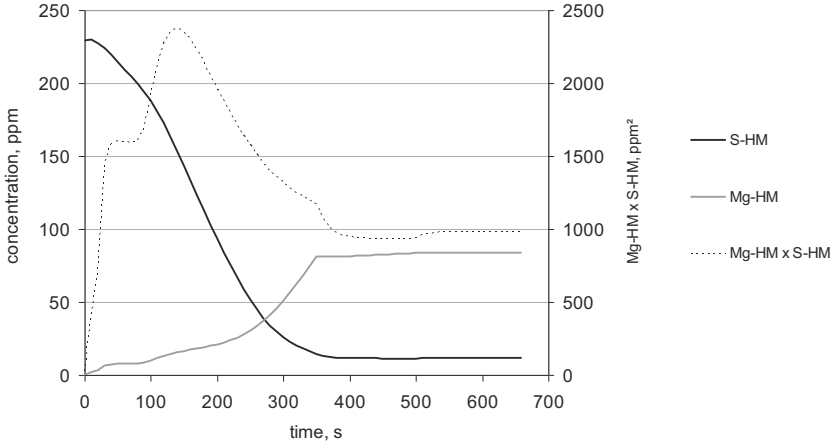

Figure 4-5. Calculated concentrations of dissolved sulphur and magnesium for Heat 2.

Both graphs indicate that shortly after the magnesium injection has started the solubility product of MgS is exceeded. This indicates that the formation of MgS is reaction rate limited. In the further course of the injection process, the products of dissolved magnesium and sulphur concentrations approach the calculated solubility products of 650 and 980 ppm² and equilibrium is reached. Both graphs also indicate that the final concentration of dissolved sulphur is attained within 400 seconds. In the remainder of the

injection process, accumulated MgS particles remain to float out of the hot metal bath effectively lowering the total sulphur content.

The values for the solubility products differ slightly from the values used in section 2.3. This is because in this model the relation given by Turkdogan[24] is implemented whereas in section 2.3 the relation given by Yang et al.[18] is used. As shown in Table 2-4 this hardly makes a difference in calculated magnesium concentration at a given sulphur concentration. Furthermore, directly after the start of injection, before the injection of magnesium has started, the magnesium concentrations already increase to 2 ppm. This is a result of the model set-up which prevents division by zero. This does not affect the modelling results for the period after the start of magnesium injection.

4.4 Discussion

In the process model, both the reaction rates and the formation and flotation of the reaction products on bulk scale are modelled by relations describing the small scale behaviour of single MgS particles. This way, a good match to the results of the XRF analysis and the Automated Inclusion Analysis is obtained. A limitation in the current model, however, is that a constant specific surface area and a single diameter is used for the MgS seeds. In reality the concentration and size of the MgS particles change during the injection process. This affects the reaction rates, as implied by, for example equations (47) and (49). Moreover, in reality the rate of flotation is a function of the particle diameter, as measured by Arai et al.[25] To increase the range of application of the process model, the development of the number density of MgS particles dispersed in hot metal should be modelled using population balance equations. This is recommended for future work aimed to increase the understanding of the hot metal desulphurisation process and achieve further improvements of the industrial process. As described in the next chapter, this is already done with the modelling of the conversion of alumina particles in liquid steel during calcium treatment.

4.5 Improvement to the hot metal desulphurisation at BOS No.2

Several improvements were made to the operation of the hot metal desulphurisation station at BOS No.2 using the model and the results of the studies of the reaction kinetics [26].

4.5.1 Carrier gas flow rate

The initial work on hot metal desulphurisation already started in 2002. At that time calcium carbide was used as desulphurisation reagent at BOS No.2. The plume model indicated that reducing the nitrogen carrier gas flow rate would increase the residence time of the reagents improving their efficiency. Accordingly a trial was set up where the gas flow rate was reduced step-wise. From the measured sulphur concentrations the efficiency of injected calcium carbide was estimated. The results are given in Figure 4-6. Up to the trial, 24 Nm^3/h was the set point for the flow rate. The results indicated a 10% improvement of efficiency with 20 Nm^3/h. Further decreasing the gas flow rate did not result in further improvement.

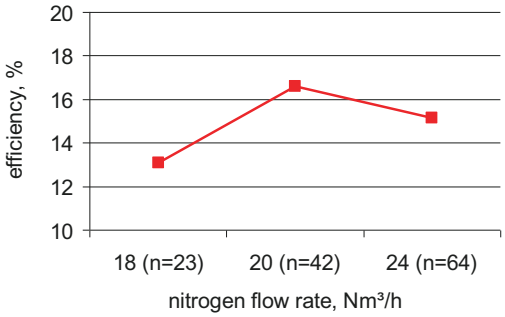

Figure 4-6. Efficiency of injected calcium carbide for various carrier gas flow rates.

4.5.2 Post-injection

After changing to a refractory with lower silica content for the hot metal ladle lining, it became possible to use lime instead of calcium carbide without excessive wear to the ladle lining. A next step became the optimisation of the post-injection, the prolonged injection of CaO after magnesium injection. Up to the trials, 60 kg of CaO was used for post-injection to clean the pneumatic conveying system from residual magnesium granules. This takes approximately 45 seconds. Initiated by the results of the sample analyses and the modelling work, a period of 3 minutes of post-injection was applied to a series of heats. The results given in Table 4-3 show that lower final sulphur levels are attained. With the trials extra reagent in the form of lime powder is injected but this does not explain the decrease in final sulphur content.

Table 4-3. Average final sulphur contents (ppm).

	45 s		3 min.	
S_{aim}	S_{final}	no.	S_{final}	no.
50	10	20	26	2255
60	12	12	30	1024
140	67	14	95	1547

After the trials post-injection was increased to two minutes for all heats. To assess the effect on hot metal loss, data were collected for heats with similar hot metal titanium content and temperature both with 45 seconds and 3 minutes of post-injection. The results given in Table 4-4 indicate that both the loss of hot metal and the time required for slag removal have been decreased by extending the period of post-injection.

Table 4-4. Average hot metal losses.

		45 s	2 min.
no. of heats	(-)	26	46
Ti-content	(wt%)	0.103	0.102
temperature	(°C)	1383	1388
hot metal loss	(kg)	4700	3850
deslagging time	(min.)	11	9

4.6 Summary and conclusions

A process model of the industrial hot metal desulphurisation process has been set up from first principles. For process variables describing transport phenomena, like dissolution of Mg into hot metal and the contact of injected particles with hot metal, values were used that match those mentioned in publications on that subject. The results are:

- The model correctly predicts the decrease in sulphur concentration and MgS concentration during the process as described in Chapters 2.
- In the beginning of the process, the formation of MgS is reaction rate limited. In the later stage of the process, the observed desulphurisation consists of the flotation of MgS particles formed in the earlier stage which determines the desulphurisation rate.
- Directions to further improve the practice of hot metal desulphurisation at BOS No.2 are given have been implemented. These are: optimisation of the carrier gas flow rate and the implementation of post-injection of lime.

4.7 References

[1] H. Visser and R. Boom: Process modelling of ladle desulphurisation by injection of CaO/Mg and CaC_2/Mg Mixtures in 300 ton ladles. Proceedings of the 3rd International Congress on the Science and Technology of Steelmaking, Charlotte, North Carolina, USA, May 9-12, 2005, pp. 369-379.

[2] H. Visser and R. Boom: Advanced process modelling of hot metal desulphurisation by injection of Mg and CaO. ISIJ Int. 46 (2006) 1771-1777.

[3] Y. Sahai and R.I.L. Guthrie. Hydrodynamics of gas stirred melts: Part I. Gas/liquid coupling. Metallurgical Transactions 13 B (1982) 193-202.

[4] Y. Sahai and R.I.L. Guthrie. Hydrodynamics of gas stirred melts: Part II. Axisymmetric flows. Metallurgical Transactions 13 B (1982) 193-202.

[5] D. Mazumdar and R.I.L. Guthrie. The physical and mathematical modelling of gas stirred ladle systems - Review. ISIJ int. 35 (1995) 1-20.

[6] D. Mazumdar and J. W. Evans. Macroscopic models for gas stirred ladles - Review. ISIJ int. 44 (2004) 447-461.

[7] Mazumdar, Guthrie and Sahai. On mathematical models and numerical solutions of gas stirred ladle systems. Appl. Math. Modelling 17 (1993) 255-262.

[8] K. Krishnapisharody and G.A. Irons. A study of spouts on bath surfaces from gas bubbling: part I. Experimental investigation. Metall. Trans. B 38B (2007) 367-375.

[9] K. Krishnapisharody and G.A. Irons. A study of spouts on bath surfaces from gas bubbling: part II. Elucidation of plume dynamics. Metall. Trans. B 38B (2007) 377-388.

[10] K. Krishnapisharody and G.A. Irons. Fundamental characterization of the fluid mechanics of multi-phase interactions in ladle metallurgy, Proc. Scanmet III, 8-11 June 2008, Luleå, Sweden, pp.589-599.

[11] G.A. Irons and R.I.L Guthrie: Kinetic aspects of magnesium desulphurization of blast furnace iron. Ironmaking and Steelmaking 8 (1981) 114-121.

[12] G.A. Irons and R.I.L Guthrie: The role of an interfacial product layer in magnesium desulphurization of molten iron. Can. Met. Quart. 21 (1982) 429-443.

[13] M. Taballa, P. Trojan, W. Bigelow, R. Flinn and L. Brockway: Mechanism of Desulfurization of Liquid Iron Carbon Alloy with Solid CaC_2 and CaO. Transactions of the American Foundrymen's Society 122 (1976) 775-786.

[14] G.A. Irons and C. Celik: Comparison of iron desulphurisation using calcium carbide and lime-magnesium mixtures. Ironmaking Steelmaking 19 (1992) 136-144.

[15] G.A. Irons: Metallurgical Aspects of Desulphurization. Paper presented at the International Magnesium Association Meeting, Prague, 1999.

[16] Y.F. Zhao and G.A. Irons: Calcium carbide powder injection into hot metal. Part 1: Heat transfer to particles. Ironmaking and Steelmaking 21 (1994) 303-308.

[17] J. Yang, S. Ozaki, R. Kakimoto, K. Okumura, M, Kuwabara and M. Sano: Desulfurization of molten iron with magnesium vapor produced in-situ by carbothermic reduction of magnesium oxide. ISIJ Int. 41 (2001) 945-954.

[18] J. Yang, K. Okumura, M. Kuwabara and M. Sano: Desulfurization of molten iron with magnesium vapor produced in-situ by aluminothermic reduction of magnesium oxide. ISIJ Int. 41 (2001) 965-973.

[19] M.C. Speer and N.A.D. Parlee: Dissolution and desulfurization reactions of magnesium vapour in liquid iron alloys. Cast Metals Research Journal 8 (1972) 122-128.

[20] J. Yang, M. Kuwabara, T. Teshigawara and M. Sano: Mechanism of resulfurization in magnesium desulfurization process of molten iron. ISIJ Int. 45 (2005) 1607.

[21] W.E. Ranz and W.R. Marshall. Jr. Chem. Eng. Prog. 48 (1952) 141-146, 173-180.

[22] R.B. Bird, W.E. Stewart and E.N. Lightfoot: Transport phenomena. John Wiley & Sons, New York (1960) p.409 and p.647.

[23] F.P. Incropera and D.P. De Witt: Fundamentals of heat and mass transfer 3rd ed., John Wiley & Sons, New York (1990) p.348 and p.418.

[24] E.T. Turkdogan: Fundamentals of Steelmaking. The Institute of Materials, 1996, p.124 and p.132-135.

[25] H. Arai, R. Otake, K. Matsumoto, N. Taniguchi. Water model experiment of removal of Inclusions in liquid steel by bubble flotation, Proc. of the 28th Journees Siderurgiques Internationales, Paris 13-14 Dec. 2007 186.

[26] H.J. Visser, E. Graveland, L. Knorren, A. Overbosch and R. Boom: Optimisation of hot metal desulphurisation at BOS2 Corus Strip Products IJmuiden. Proceedings of the 5th European Oxygen Steelmaking Conference EOSC2006, 26-28 June 2006, Aachen, Germany, pp. 3-8.

5 The calcium treatment of aluminium killed liquid steel

5.1 Introduction

In Chapters 2 and 3 the study of the hot metal desulphurisation process is described. Based on the knowledge gained, Chapter 4 describes the set-up of a process model predicting the decrease of the hot metal sulphur content during the process. In this chapter the set-up of a process model of the calcium treatment is described. The modelling assumptions are primarily based on work done by Tiekink et al.[1]-[3] First the results of his measurements on both the laboratory and industrial scale are summarised. Based on this, a reactor model is derived from first principles predicting the chemical composition of the non-metallic particles during the calcium treatment. Finally the model predictions are compared to the measurements. An additional objective is to assess Population Balance Equations in modelling ladle metallurgy processes.

This work has been presented at the 28èmes Journées Sidérurgiques Internationales ATS, on 13-14 Dec. 2007 in Paris and has been published in La Revue de Métallurgie in 2008 [4],[5].

5.2 Measurements

The calcium treatment of aluminium killed liquid steel as performed at BOS No.2 is described in section 1.4. Tiekink et al.[1]-[3] have done measurements on calcium treatment on both the laboratory and industrial scale. In the laboratory test, CaSi wire was injected into a 40 kg aluminium killed steel melt. At the same time, a water cooled tube was inserted in the melt. In the steel freezing on the tube, reaction products were arrested during the progress of the reaction. Microscopic analysis of the solidified steel shell showed the following development of reaction products: first Al_2O_3 with some CaO was formed, followed by calcium aluminate (in the following abbreviated by CA) with high Al_2O_3 content, sometimes with CaS deposited on it, then CA and finally CA with high CaO content. Due to the absence of ferrostatic pressure, the CaSi wire injection in an open 40 kg furnace caused considerable splashing. Even in this oxidising environment some CaS was formed on calcium aluminates. This implies local depletion of dissolved oxygen by the initial formation of CaO.

With plant trials at BOS No.2 calcium-cored wire (CaFe and CaSi) was injected into 320 t steel ladles, both at the ladle furnace and at the stirring station. Steel samples were taken before, during and after the injection. Analysis of the inclusions in the samples indicated that before calcium injection Al_2O_3 particles can contain some CaO and MgO. During injection, CaS and CaO appear to form simultaneously resulting in almost complete conversion of Al_2O_3 particles to CA/CaS, but on average not within the liquid window. This discrepancy with the lab scale test, where formation of CaO was observed before CaS, is explained by the distance between the locations of sampling and the calcium bubble plume where the reactions take place. In this calcium-rich zone dissolved oxygen is locally

depleted, which was measured with oxygen activity probes, creating conditions for the formation of CaS. The reaction products are then mixed up into the rest of the liquid steel bath where the concentration of these high-CaO CA/CaS particles increases with time. The initial formation of high Al_2O_3 containing CA may thus be missed in the samples taken from the steel bulk.

Figure 5-1 shows examples of the CA/CaS reaction products. CaS is nearly always observed on CA suggesting the formation reaction takes place on existing particles.

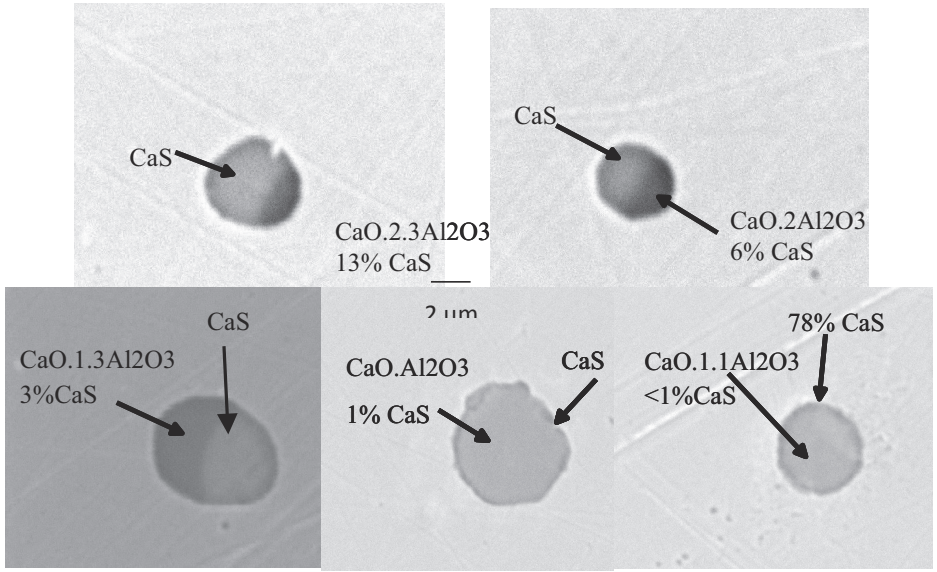

Figure 5-1. Inclusions in a ladle sample (two photos top) and in a tundish sample from the same heat (lower three photos) of CaFe-treated low carbon aluminium killed steel. Tiekink et al.[2]

5.3 Modelling calcium treatment

5.3.1 Solubility of calcium in liquid steel

An important subject in the set-up of a reactor model of the calcium treatment is the state of calcium during the modification reactions of Al_2O_3 to CA. Published opinions vary from calcium being dissolved in liquid steel to complete insolubility and reaction in the gaseous state only. Due to the high vapour pressure, low solubility and quick reaction with oxygen, the solubility of metallic calcium in liquid steel is difficult to measure. Sponseller and Flinn[7] and Köhler et al.[8] performed measurements under high argon pressure to keep the calcium liquid resulting in a maximum solubility of 300 ppm at 1600°C. Ototani et al.[9] estimated the solubility of calcium dissolved in liquid iron to be 240 ppm. Kobiyashi et al.[10] proposed that the amount of dissolved calcium, in a steady state system of calcium/argon bubbling and liquid iron, is not greater than 30 ppm. In a recent study by Taguchi et al.[11] the equilibrium between CaO-Al_2O_3 slag and liquid iron the calcium concentration was measured to be below 3 ppm and a concentration of 1 ppm was assumed.

In the steel samples taken at BOS No.2 hardly any pure CaO and CaS particles have been found. These would have resulted from a reaction between gaseous calcium and dissolved oxygen and sulphur forming new particles thus requiring nucleation. Based on this, it is assumed that after dissolution of the cored wire, calcium is released as either droplets or bubbles and then dissolves into liquid steel where it reacts with dissolved oxygen and sulphur on the already existing particles. With the modelling simulations, the varying values for the calcium solubility can be tried out.

5.3.2 Modification of an individual alumina particle

Based on the results of the laboratory scale experiments it is assumed that dissolved calcium and oxygen react with Al_2O_3 to CA with gradually increasing CaO fraction. If the oxygen activity has become sufficiently low, dissolved calcium and sulphur react on the surface of the particle to form CaS. SEM analysis of the reaction products did not clearly show concentration gradients within the oxide fraction so this is considered homogeneous. This is shown schematically in Figure 5-2.

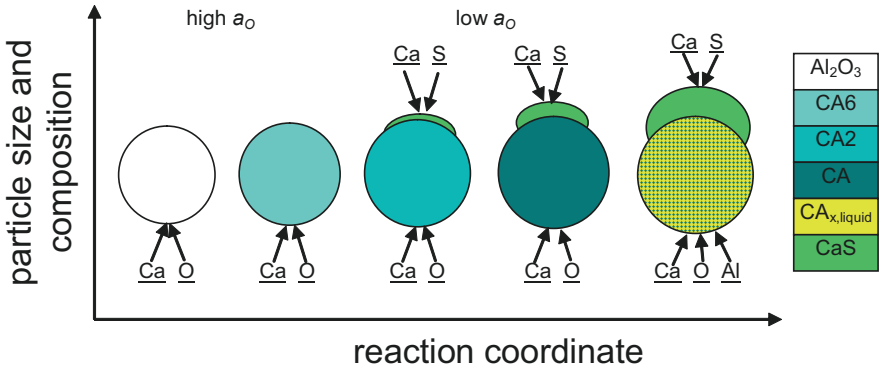

Figure 5-2. Conversion of an Al_2O_3 particle to an $nCaO.Al_2O_3$/CaS particle.

Before addition of calcium, the dissolved oxygen and aluminium contents are at near equilibrium with pure alumina. With the measurements on industrial samples more complex compositions sometimes have been encountered, containing for example MgO. For this model only the formation of CaO and CaS on Al_2O_3 particles is considered.

5.3.3 Flow field in the steel ladle

The plant scale trials indicate the presence of a calcium rich/oxygen depleted region in the liquid steel bath. This region is well stirred due to the break-up of the calcium wire and the rising calcium droplets and bubbles. The remaining volume of the steel bath is stirred by injection of argon through bottom stirring plugs. The calcium vapour plume induces a circulation flow of liquid steel with suspended particles between these zones. This flow field is modelled by division of the liquid steel bath into two continuously operated Ideally Stirred Tank Reactors (CISTR's), each representing one of the steel volumes, coupled by a circulation flow of liquid steel. This is shown in Figure 5-3.

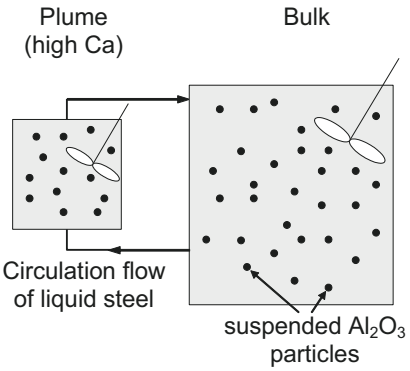

Figure 5-3. The two reaction zones in the liquid steel bath, each modelled by a CISTR.

Particles that leave the plume zone and enter the bulk are exposed to steel with alternating solute concentrations: from high calcium/low oxygen to low calcium and somewhat higher oxygen. This implies that CaS formed in the plume could revert to CaO in the bulk.

Figure 5-4 shows the calculated flow field in the steel ladle resulting from the calcium vapour plume that entrains liquid steel in a circulation flow as calculated by T. Lucas.[12] At the depth where the calcium vapour pressure is reached, the volume fraction of calcium vapour suddenly increases.

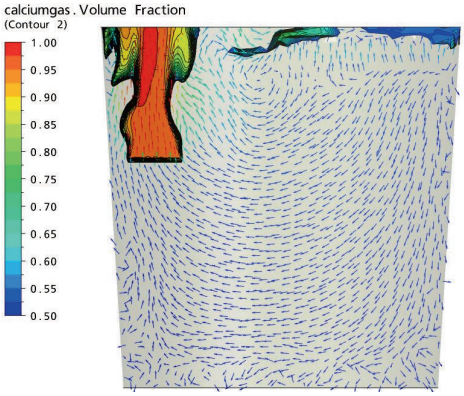

Figure 5-4. CFD flow field simulation of calcium injection in liquid steel ladle.

The volumes of the two reaction zones and the circulation flow rate were derived from the results of these CFD flow field calculations and are given in Table 5-1

Table 5-1. Properties of the two reaction zones

V_{plume}	(m^3)	0.58
V_{bulk}	(m^3)	40
Q_{circ}	(m^3/s)	0.74

5.3.4 Flotation, agglomeration and nucleation.

With ladle furnace treatments at BOS No.2 the last aluminium injection is always followed by a minimum period of stirring by injection of argon through the bottom stirring plugs. This ensures there is sufficient time for growth, coalescence and flotation of alumina particles. After this only the smallest fraction of particles remains in the liquid steel. It is assumed that these particles do not float out and do not further agglomerate during the injection of calcium.

Automated inclusion Analysis (AIA) of steel samples taken right before the start of calcium injection indicates the concentration of alumina particles is in the order of 10.000 per mm³ (Figure 5-6). The oxygen content of the samples was measured as 20 ppm. This abundance of nucleation sites, together with the observed development of Al_2O_3 to CA/CaS particles leads to the assumption that CaO and CaS are deposited on existing particles and homogeneous nucleation can be neglected. This is also discussed in 5.3.1. The total number of particles thus remains unaltered although their size and composition change.

5.3.5 Population Balance of alumina particles

The alumina particles suspended in liquid steel are entrained with the circulation flow between the two reaction zones and are therefore subjected to alternating thermo-chemical conditions that govern the conversion to calcium-aluminates. After a certain period, each particle has a different history of presence in each of the zones and therefore a different composition and size. This results in a population of particles distributed over composition and size. This can be described by Population Balance Equations as explained by Ramkrishna.[13] In this particular metallurgical system, a particle is described by its diameter d_p and its composition defined by X_{CaO} and X_{CaS}. The properties of a particle thus are denoted by the vector x:

$$x = \left(d_p, X_{CaO}, X_{CaS}\right)$$

The population of particles in liquid steel at time t is given by the number density f_1:

$$f_1 = \left(d_p, X_{CaO}, X_{CaS}, t\right) = f_1\left(x, t\right), \text{ -/μm}^4$$

The number of particles per unit volume of liquid steel within a certain range of size and composition is obtained by integrating f_1 over that range. The unit of f_1 is number of particles per volume unit of liquid steel per length scale of particle diameter per molar fraction CaO per molar fraction CaS. The dimension therefore is $1/L^4$. Because the particle diameter is in the order of μm, $1/\mu m^4$ is used. Formally this should be written as $-/(\mu m)^4$ but $-/\mu m^4$ is used here for convenience.

Due to the chemical reactions the properties of a particle change in time with the rate of change denoted by the vector $\dot{X}$:

$$\dot{X} = \left(\frac{\partial d_p}{\partial t}, \frac{\partial X_{CaO}}{\partial t}, \frac{\partial X_{CaS}}{\partial t}\right)$$

The components of $\dot{X}$ are derived from the conversion rates of the particle. These are functions of the particle properties, the concentrations of the solutes, the temperature and various physical and thermodynamic properties.

With the previously explained assumptions that flotation, coalescence and nucleation do not occur and the division of the steel bath into two reaction zones coupled by a circulation flow, the development of f_1 in each reaction zone is described by the following Population Balance Equation:

$$\frac{\partial f_1}{\partial t} + \nabla_x \left(\dot{X} f_1 \right) = \frac{1}{\tau} \left(f_{1,in} - f_1 \right) \text{-/µm}^4\text{s} \tag{58}$$

where the residence time in each reaction zone follows from:

$$\tau_{plume} = \frac{V_{plume}}{Q_{circ}} \text{ and } \tau_{bulk} = \frac{V_{bulk}}{Q_{circ}} \tag{59}$$

The depletion rates of solutes Ca, O, S and Al from the liquid steel are obtained by integrating the chemical conversion rates over the complete domain of f_1.

5.3.6 Conversion of a single particle

It is assumed that the rates of formation of CaO, CaS and Al_2O_3 are limited by mass transfer of the solutes from the bulk of the steel to the particle surface. The concentrations of the solutes on the inclusion interface, [*%i*]* follow from the activities on the surface that are governed by the thermodynamic equilibria. The phases in the multiphase particle are assumed to be in equilibrium. The formation reactions and Gibbs energies of formation are:

$$[Ca] + [O] = CaO_{solid} \qquad \Delta G^o_{CaO} = -1205.115 + 0.37714T \tag{60}$$

$$2\,[Al] + 3\,[O] = Al_2O_{3\,solid} \qquad \Delta G^o_{Al_2O_3} = -678.227 + 0.197947\,T \tag{61}$$

$$[Ca] + [S] = CaS_{solid} \qquad \Delta G^o_{CaS} = -413.044 + 0.80417T \tag{62}$$

The Gibbs energies refer to the 1wt% standard state for the solutes. The interface concentrations follow from the equilibria constants and activity coefficients:

$$K_{Al_2O_3} = \frac{a_{Al_2O_3}}{h_{Al}{}^{*2}\, h_O{}^{*3}} = \frac{a_{Al_2O_3}}{f_{Al}{}^{*2}\,[\%Al]^{*2}\, f_O{}^{*3}\,[\%O]^{*3}} \tag{63}$$

$$K_{CaO} = \frac{a_{CaO}}{h_{Ca} * h_O *} = \frac{a_{CaO}}{f_{Ca} * [\%Ca] * f_O * [\%O] *} \tag{64}$$

$$K_{CaS} = \frac{a_{CaS}}{h_{Ca} * h_S *} = \frac{a_{CaS}}{f_{Ca} * [\%Ca] * f_S * [\%S] *} \tag{65}$$

The equilibrium constants relate to the Gibbs energies of formation according to:

$$\Delta G_j^o = -RT \ln K_j \tag{66}$$

The activity coefficients can be derived from:

$$\log f_i * = \sum e_i^k [\%k] * \tag{67}$$

The interaction coefficients e_i^k are taken from Sigworth and Elliott.[14]

The activity of CaS is unity. CaO and Al_2O_3 form solutions of solid and liquid calcium aluminates like CA6, CA2, CA, C12A7, C3A, each with its own enthalpy of formation. This results in a decrease of the activities of CaO and Al_2O_3 in the particle. Figure 5-5 shows the calculated activities of CaO and Al_2O_3 in the binary system.

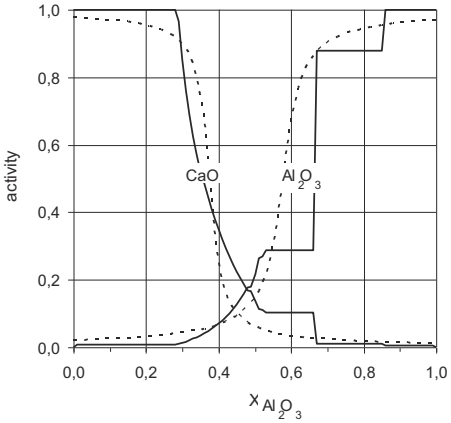

Figure 5-5. Activities of CaO and Al_2O_3 in the binary system; results of FactSage calculation and fitted (dotted) relations.

To avoid having to incorporate all equilibria of the various calcium aluminates, smooth functions are fitted for the activities of Al_2O_3 and CaO. Since a particle can also contain CaS, the molar fraction of Al_2O_3 is divided by the sum of the molar fractions of Al_2O_3 and CaO.

$$a_{Al_2O_3} = 0.5 + \frac{1}{\pi} a\tan\left(26\frac{X_{Al_2O_3}}{X_{Al_2O_3} + X_{CaO}} - 15\right) \tag{68}$$

$$a_{CaO} = 0.5 - \frac{1}{\pi} a\tan\left(40\frac{X_{Al_2O_3}}{X_{Al_2O_3} + X_{CaO}} - 15\right) \tag{69}$$

The concentration difference between the particle surface and the liquid steel results in a mass flux of solute *i* to and from the particle surface:

$$J_i = \frac{k_{m,i}\rho_{steel}}{100M_i}\left([\%i] - [\%i]^*\right) \tag{70}$$

The particles are assumed to be spherical. The mass-transfer between a sphere and it surrounding liquid can be expressed by the Ranz-Marshall equation:[15]-[17]

$$Sh = 2.0 + 0.6Re^{\frac{1}{2}}Sc^{\frac{1}{3}} \tag{71}$$

For a particle in liquid steel the dimensionless numbers are given by:

$$Sh = \frac{k_{m,i}d_p}{D_{i,steel}},\ Re = \frac{v_p d_p}{\nu_{steel}},\ Sc = \frac{\nu_{steel}}{D_{i,steel}} \tag{72}$$

For particles of this size it can be assumed there is no relative velocity with respect to the surrounding liquid steel, i.e. $v_p = 0$, $Re = 0$ and $Sh = 2$.

Calcium diffusing towards the particle surface can react with oxygen and sulphur to form CaO and CaS. Aluminium forms Al_2O_3 and calcium can react with Al_2O_3 to form CaO and dissolved aluminium. The stoichiometric requirement for the molar fluxes to the inclusion surface thus becomes:

$$J_{Ca} + {}^3/_2 J_{Al} = J_O + J_S \tag{73}$$

Simultaneous solution of equations (63) to (73) results in the molar fluxes of solutes to and from the particle leading to an increase in the masses of the compounds constituting the particle. Sulphur diffusing to the particle with surface area a_p forms CaS:

$$\frac{dn_{CaS}}{dt} = A_p J_S \tag{74}$$

Where:

$$A_p = \pi d_p^{\,2} \tag{75}$$

Aluminium diffusing to the particle forms Al_2O_3:

$$\frac{dn_{Al_2O_3}}{dt} = \tfrac{1}{2} A_p J_{Al} \tag{76}$$

The CaO formation is determined by the diffusion of calcium to the particle minus the formation of CaS

$$\frac{dn_{CaO}}{dt} = A_p \left(J_{Ca} - J_S \right) \tag{77}$$

Assuming the density of CA is the proportional average of CaO and Al_2O_3, the particle size and composition are related by:

$$\frac{\pi}{6} d_p^{\,3} = \sum_j \frac{n_j M_j}{\rho_j} \tag{78}$$

and:

$$X_j = \frac{n_j}{\sum_j n_j} \tag{79}$$

For each reaction zone the components of $\dot{X}$ can be derived from (78) and (79). For all solutes, except calcium in the plume zone, the development of the concentrations follows from the mass balance of a CISTR where the reaction rate r_i is obtained by integrating the molar fluxes per particle over the entire particle population.

$$\frac{d[\%i]}{dt} = r_i + \frac{1}{\tau} \left([\%i]_{in} - [\%i] \right) \tag{80}$$

$$r_i = \frac{100 M_i}{\rho_{steel}} \int_{d_p=0}^{\infty} \int_{X_{CaO}=0}^{1} \int_{X_{CaS}=0}^{1} J_i A_p f_1 dX_{CaS} dX_{CaO} dd_p \tag{81}$$

Where $[\%i]_{in}$ represents the concentration of solute *i* in the liquid steel circulation flow coming from the other reaction zone. For dissolved calcium in the plume zone, a source term should be added to (80) representing the dissolution from the calcium droplets and

bubbles into the steel. This is now modelled by keeping the liquid steel in the plume zone saturated with calcium during calcium injection.

5.3.7 Initial number density of alumina particles

Before calcium injection only pure Al_2O_3 particles are suspended in the liquid steel. Figure 5-6 shows their number density in the steel sample taken before calcium treatment of the trial heat (Table 5-3) as measured AIA.

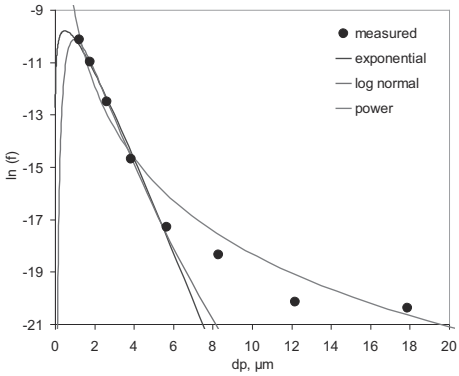

Figure 5-6. Initial density of alumina particles, expressed in μm^{-4}.

With this measurement the lower limit for the particle cross section was set at 0.8 μm^2 so circular particles with a diameter smaller than 1 µm were not measured although they exist. To include these small particles in the calculations, an assumption has to be made for the initial distribution. In Figure 5-6 several assumptions are compared to the measurements. Since the derivation of the number density of the larger particles from the AIA results is accompanied with greater uncertainty, emphasis is put on the proper fit for the small particles and the exponential distribution is used for the calculations. The fit is described by:

$$f_1 = 3 \cdot 10^{-4} d_p e^{-2 d_p} \tag{82}$$

5.4 Modelling Results

5.4.1 Numerical solution

Equations (58) to (81) are solved simultaneously using Aspen Custom Modeller 2004.1. The result is the development of size and composition of the particle population and the concentration of solutes during calcium injection. To limit the computation time required, the Al_2O_3 part of each particle is considered inert. This means no alumina is formed or according to reaction (61) and the activity of CaO is not lowered according to (69) but is kept constant as 1. The values for the diffusivities of solutes in liquid steel were taken from Zu et al.[18] The value for the diffusivity of aluminium is estimated.

Table 5-2. Diffusivities of solutes in liquid steel.

solute	Diffusivity (m^2/s)
Al	$3.5 \cdot 10^{-9}$
Ca	$3.0 \cdot 10^{-9}$
O	$3.1 \cdot 10^{-9}$
S	$4.3 \cdot 10^{-9}$

5.4.2 Measured data

The results form trial Heat LF K, described in Section 4.5 of the thesis W. Tiekink[3] are used as measurement data. To compare the calculation results to the measurements, the measured particle data are processed by classifying the particles into the same intervals of d_p, X_{CaS} and X_{CaO} as used in the numerical solutions. The number densities are derived from the AIA measurements on the sample cross sections using the software CSDCorrections 1.37 developed by M.D. Higgins[19],[20]. Table 5-3 gives the properties of the heat and the instances of sampling.

Table 5-3. Properties of the heat and sampling.

Steel temperature	(°C)	1592
Steel mass	(t)	311
[%Al]	(wt%)	0.05
[%S]	(wt%)	0.005
duration of calcium injection	(s)	120
amount of calcium added	(kg)	47

sample	time after start injection (s)
1	0
2	12
3	73
4	132
5	225
6	360

5.4.3 Calcium solubility

Simulations were done using two values for the calcium solubility in liquid steel: 1 ppm and 30 ppm. The results shown refer to the bulk volume of the steel; this is where the samples were taken and measurements where done and which accounts for 98.6 % of the steel volume in the reactor model. Figure 5-7. shows the measured oxygen activities and the results of both simulations. The results for using $[Ca]_{sat}$ = 1 ppm show good agreement with the measured oxygen activities.

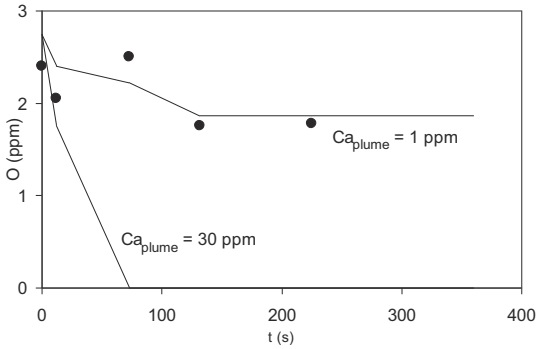

Figure 5-7. Predicted versus measured concentration of dissolved oxygen.

Figure 5-8 shows the predicted versus measured total calcium content (Ca_{tot}). Ca_{tot} is obtained by integration of X_{CaO} and X_{CaS} of all particles over the complete range of d_p, X_{CaO} and X_{CaS} plus the amount of dissolved calcium. Again, the results for Ca_{sat} = 1 ppm show better agreement with the measurements.

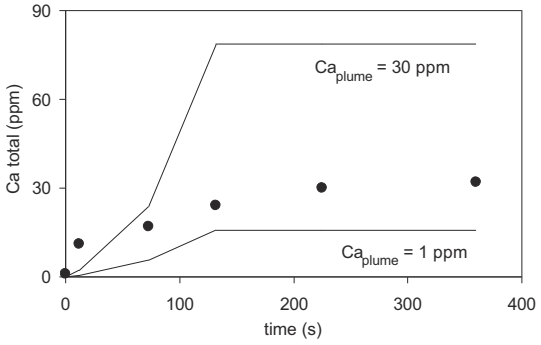

Figure 5-8. Predicted versus measured total calcium content.

Figure 5-9 shows the predicted versus the measured fraction of CaS averaged over all particles. For both simulations, the predicted CaS-content is higher than the measured values.

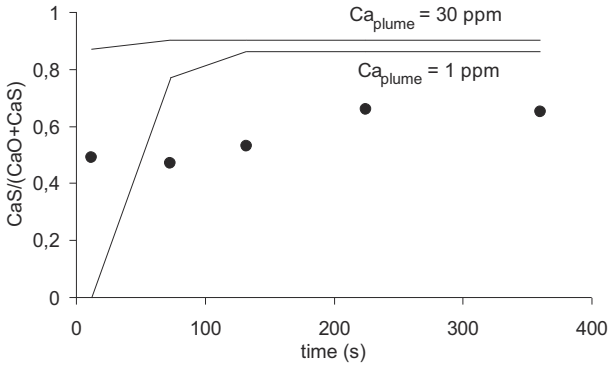

Figure 5-9. Predicted and measured average value of CaS over total calcium content of the particles.

From the results presented in Figure 5-8 and Figure 5-9 it is concluded that the predicted amount of CaO formation is lower than observed. This is probably due to oxygen pick up during the calcium injection. Due to the assumed calcium saturation of the plume zone, this will result in the same oxygen activity but more CaO will actually be formed. Oxygen can be picked up at the spout area where the slag is pushed aside and steel is exposed to open air. Another source of oxygen could be formed by the air present inside the cored wires.

5.4.4 Number densities

Figure 5-10 shows the predicted number densities of the suspended (initial) alumina particles as a function of size only, at the instances of sampling. The predictions were done using the exponential initial particle size distribution and a calcium saturation concentration of 1 ppm.

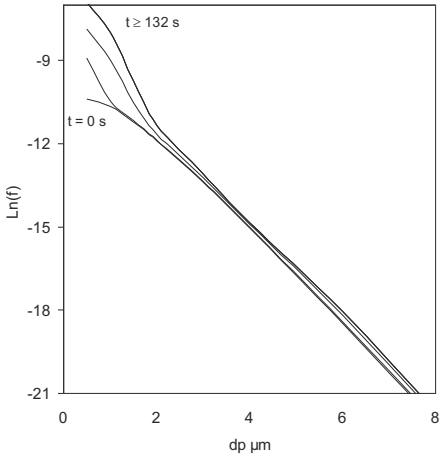

Figure 5-10. Predicted number densities (ln f (μm^{-4})) as function of particle size only.

The injection of calcium lasted for 120 seconds and after 132 seconds the distribution does not change anymore. Due to growth of the smallest particles (< 1 µm) , the number density of particles with diameter between 0.5 and 3 µm increases considerably during the calcium treatment. For d_p = 1 µm, the density increases by a factor of fifteen.

Figure 5-11 shows the predicted versus measured number densities at the instances of sampling. Over the whole range of particle size, the coincidence is quite good. Also the predicted increase of density of small particles is observed with the measurements. This coincides with the assumption that initially a high concentration of particles below the detection limit is present (section 5.3.7).

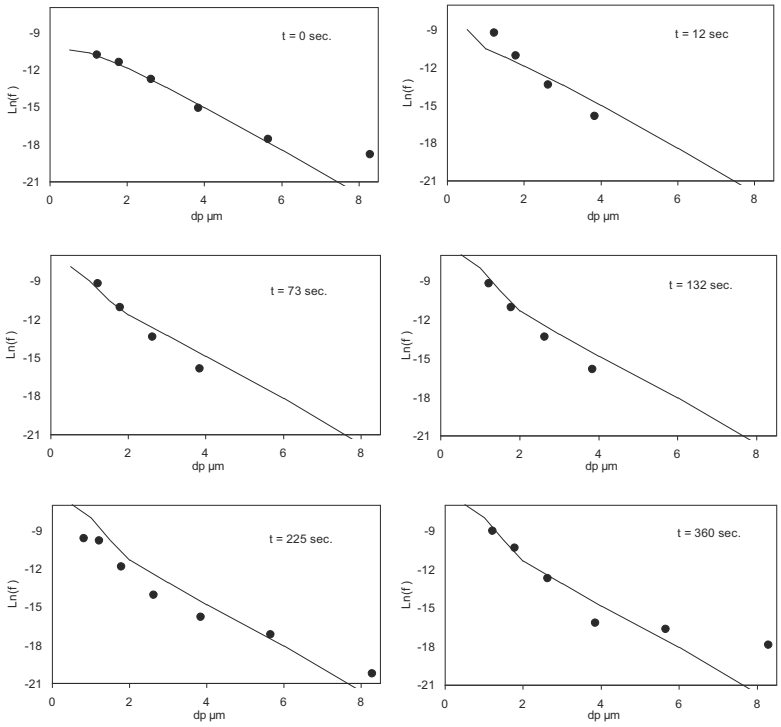

Figure 5-11. Predicted and measured number densities as function of particle size only.

5.5 Discussion

Important assumptions in the model describing the calcium treatment of alumina particles concern the division into two reactor zones, the solubility of calcium in liquid steel, the presence of particles smaller than the detection limit and the assumption that the total number of particles remains unaltered.

The measured increase in particle concentration is explained by the growth of smaller particles to particles larger than detection limit. According to eq. (72) the mass transfer coefficient is higher for smaller particles, so CaO and CaS are deposited at a higher rate and the smallest particles grow at a relatively higher rate.

Division of the liquid steel bath into two reactor zones and assuming that the solubility of calcium in liquid steel is 1 ppm has led to a proper prediction of the particle composition. The difference between measurement results on the laboratory and industrial scale can therefore be explained by non-homogeneity of the liquid steel in the 320 t ladle during calcium treatment. The CaS content predicted, however, is too high, most likely because the oxygen pick-up is neglected in the model.

Based on the results of laboratory scale measurements, Lu, Irons and Lu [21] concluded that reactions between dissolving calcium with oxygen and sulphur in the liquid film surrounding calcium vapour bubbles are inevitable, resulting in direct formation of CaO and CaS. This was not observed by Tiekink [1]-[3]. Furthermore, they also concluded that the effective dissolved calcium content is less than 1 ppm. This is in reasonable accordance with the finding that using a value of 1 ppm in the calculations results in a better agreement with measurements than using a value of 30 ppm dissolved calcium.

Ye, Jönsson and Lund [22] proposed a similar mechanism for the modification, including diffusion of dissolved calcium, oxygen and sulphur to the particle surface. The difference with the current proposal is the suggestion that CA6 is first formed on the surface, from which CaO diffuses into the particle volume. When oxygen activity has become sufficiently low, a layer of solid CaS is formed on the surface. This impedes further reaction of calcium with oxygen resulting in an homogenous aluminate with lower conversion than expected. Particles as shown in Figure 5-1, however, do not show a gradient in CaO in the oxide phase and the CaS is often only formed locally on the surface. Furthermore, in steel samples from both the laboratory and industrial scale, high-CaO CA particles with CaS have been found indicating advanced conversion.

5.6 Summary and conclusions

Based on the results of previous experimental work on the transformation of alumina particles a process model of the calcium treatment of aluminium killed steel has been set up from first principles. The results are:

- The observed difference between the inclusion composition resulting from calcium injection on the laboratory and industrial scale is explained by inhomogeneity of the liquid steel bath in the 320 t ladle. This has been modelled by division of the liquid steel bath into two, well mixed, reaction zones with a circulation flow of liquid steel.
- Division of the liquid steel bath into two reactor zones and assuming that the solubility of calcium in liquid steel is 1 ppm leads to proper prediction of the particle composition.
- The predicted CaS content of the particles however, is too high, most likely because oxygen pick-up is neglected in the model.
- The observed increase in number of inclusions during the injection of calcium is explained by the growth of smaller particles to particles with cross section above the lower detection limit.
- Automated Inclusion Analysis generates an abundance of measurement data of phases formed with calcium injection. Population Balance modelling is a suitable

tool in the interpretation of these results and therefore supports the development of new theories about the process.

5.7 References

[1] W. Tiekink, B. Santillana, R. Kooter, F. Mensonides, B. Deo, R. Boom: Calcium: toy, tool or trouble. Conf. proc. AIST 2006 Vol II. Cleveland USA, May 1-4 (2006) 395-404.

[2] W. Tiekink, R. Kooter, E. Bosma, J. Brockhoff, R. Hackstein, F. Villette: Improved calcium wire properties results in high yields. EOSC Aachen Germany, 26-28 June 2006, 66-71.

[3] W. Tiekink: Al_2O_3 in steel and its transformation with calcium. PhD-thesis, Delft University of Technology, Delft (Netherlands), 2012.

[4] Hessel-Jan Visser, Mostafa Biglari and Rob Boom: Simulation of the Ca-treatment of Al-killed liquid steel. Proceedings of the 28èmes Journées Sidérurgiques Internationales ATS, Paris, 13-14 Dec. 2007, pp. 147-154.

[5] Hessel-Jan Visser, Mostafa Biglari and Rob Boom: Simulation of the Ca-treatment of Al-killed liquid steel. La Revue de Métallurgie - CIT 105 (2008) 172-180.

[6] S.R. Story, T.J. Piccone, R.J. Fruehan and M. Potter: Inclusion analysis to predict casting behaviour. ISSTech 2003 Conf. Proc. (2003) pp. 129-139.

[7] D.L. Sponseller and R.A. Flinn: The solubility of calcium in liquid iron and third-element interaction effects. Trans. Met. Soc. AIME. 23 (1964) 876-888.

[8] M. Köhler, H-J. Engell and D. Janke: Solubility of calcium in Fe-Ca-Xi melts. Steel Research 65 (1985) 419-423.

[9] T. Ototani, Y. Kataura and T. Degawa: Deoxidation of liquid iron and its alloys by calcium contained in lime crucible. Trans. ISIJ 16 (1976) 275-282.

[10] S. Kobayashi, Y. Omori and K. Sabongi: On the deoxidation of liquid iron with bubbles of argon-calcium mixture. Trans. ISIJ 11 (1971) 260-269.

[11] K. Taguchi, H. Ono-Nakazato, T. Usui, K. Marukawa, K. Katogi and Hi. Kosaka: Complex deoxidation equilibria of molten iron by aluminium and calcium. ISIJ Int. 45 (2005) 1572-1576.

[12] T. Lucas: Calcium injection study for optimal mixing in the ladle furnace at OSF2. Internal communication Corus RD&T (2007).

[13] D. Ramkrishna: Population balances: theory and applications to particulate systems in engineering. San Diego, CA: Academic Press (2000).

[14] G.K. Sigworth and J.F. Elliott: The thermodynamics of liquid dilute iron alloys. Metal Science 8 (1974) 298-310.

[15] W.E. Ranz and W.R. Marshall. Jr. Chem. Eng. Prog. 48 (1952) 141-146, 173-180.

[16] R.B. Bird, W.E. Stewart and E.N. Lightfoot: Transport phenomena. John Wiley & Sons, New York (1960) p.409 and p.647.

[17] F.P. Incropera and D.P. De Witt: Fundamentals of heat and mass transfer 3rd ed., John Wiley & Sons, New York (1990) p.348 and p.418.

[18] D.Z. Lu, G.A. Irons and W.K. Lu: Kinetics and mechanisms of calcium dissolution and modification of oxide and sulfide inclusions in steel. Ironmaking and Steelmaking 21 (1994) 362-371.

[19] M.D. Higgins: Measurement of Crystal Size Distributions. American Mineralogist 85 (2000) 1105-1116.

[20] M.D. Higgins: Closure in crystal size distributions (CSD) verification of CSD calculations, and the significance of CSD fans. American Mineralogist 87 (2002) 171-175.

[21] D-Z. Lu, G.A. Irons and W-K. Lu: Kinetics and mechanisms of calcium absorption and inclusion modification of steel. Proc. Scaninject VI, June 1992, Lulea, Sweden, pp. 239-263.

[22] Ye. Guozhu, P. Jönsson: Thermodynamics and kinetics of the modification of Al_2O_3 inclusions, ISIJ Int. 36 (1996) Supplement 105-S108.

6 Modelling of injection processes in liquid metals

6.1 Recapitulation

In the previous chapters the research on the reaction kinetics of hot metal desulphurisation and the calcium treatment of aluminium killed steel is described, followed by the development and validation of reactor models of these processes. In addition to setting up these models, an additional goal of this work is to give directions for future work on the modelling of injection processes in general. For this, the findings of the work so far are shortly summarised.

For both the hot metal desulphurisation and the calcium treatment of aluminium killed steel the formation of the reaction products has been studied with Scanning Electron Microscopy on samples taken during the processes. With both processes, the reaction products appear as particulates dispersed in the liquid hot metal and steel. Changes in dimensions, compositions and concentrations of these particulates during the course of the injection processes have been obtained using Automated Inclusion Analysis. For both processes this has led to detailed insights on the formation, growth and flotation of the reaction products. With hot metal desulphurisation, magnesium sulphide particles are formed in the bubble plume, get dispersed in the hot metal bulk and grow further by deposition of MgS, formed by reaction of dissolved sulphur and magnesium. Subsequently, the particulates are washed out by the bubble plume and are finally absorbed into the slag layer where they react with co-injected lime to more stable calcium sulphide. With calcium treatment of aluminium killed steel, dispersed, initially pure alumina particles grow by deposition of calcium oxide and calcium sulphide formed by the reaction of dissolved calcium, oxygen and sulphur. They are thus converted to multiphase calcium aluminate /calcium sulphide particles of varying compositions and size that remain dispersed in the steel.

The behaviour of the particulates explains the observed deviations from over-all thermo chemical equilibrium for these industrial scale processes. For hot metal desulphurisation the observed initial low rate of desulphurisation and the apparent super saturation of magnesium sulphide during the process are explained by the initial dissolution of magnesium and the accumulation of magnesium sulphide particulates in the hot metal. For the calcium treatment, the variety of compositions of the calcium aluminate /calcium sulphide particles is explained by the strong local differences in calcium activity in the steel bath to which the particles are subjected repeatedly.

Based on the observations, reactor models of the two processes have been developed. In general, a chemical reactor model incorporates descriptions of the thermodynamics, kinetics, mass-transfer and mixing, as described by Westerterp et al.[1] These topics have all been addressed. The thermodynamics are described by the relations for chemical equilibria. Chemical reactions can be assumed to proceed instantaneously at steelmaking temperatures. The reactions therefore are limited by mass transfer as described by the mass transfer of the reactants to the surface of the product particulates. The dissimilar

behaviour of the injected reagents has led to different solutions for the description of macroscopic mixing. Since magnesium can dissolve into hot metal to approximately 0.2 wt% and the hot metal is well mixed by the gas injection a uniform composition of the hot metal bath is assumed. The conversion of dissolved sulphur in the hot metal bath therefore is adequately described by a well-mixed batch reactor. On the contrary, calcium hardly dissolves in liquid steel and quickly escapes the steel bath after injection. This way, only locally interaction between calcium and alumina particulates can occur. Based on this, the mixing of the steel bath is modelled by two continuously ideally stirred tank reactors (CISTR's) coupled by a liquid steel circulation flow. To properly include the effect of mixing of the liquid steel on the dispersed particles, a population balance was set-up for the particles. This way the influence of the particle size on the reaction rates could also be included. For future work on the modelling of the hot metal desulphurisation, it is recommended to apply a population balance for the MgS particles as well such that flotation and reaction rate can be modelled as function of particle diameter. With both models, the observed conversion rates are correctly described. Since the models are based on first principles and furthermore only requires tuning of some general process parameters this model set-up can be applied to successfully describe other ladle injection processes as well. Before directions for future work on this topic are given, the macroscopic flow field in gas stirred ladles is discussed in some more detail.

6.2 Mixing in gas stirred ladles

The mixing of the liquid metals the gas stirred ladles often is a topic for publications in the field of metallurgy. According to Mazumdar and Evans[2], macroscopic models, despite being simplistic have a sound basis and can form a reasonably reliable predictive framework for first hand analysis of rate processes in gas stirred ladles. According to Oeters et al.[3] and Pietzka et al.[4] three main zones can be distinguished in the melt when gas is injected from the bottom of a ladle: (1) the buoyant plume with high turbulence and a clear upward flow and the deflected stream underneath the slag layer, (2) a torus below the surface near the wall with high velocities and, (3) for ladles with H/D larger than 0.6, a so-called stagnant zone under the torus with creeping motions that is weakly mixed. There seems to be no difference between injection through a porous plug or a tuyere in the bottom or a lance positioned near the bottom. Figure 6-1 schematically shows, on the left hand side, the division of the hot metal bath into these three zones and the circulation flows exchanging hot metal between these zones.

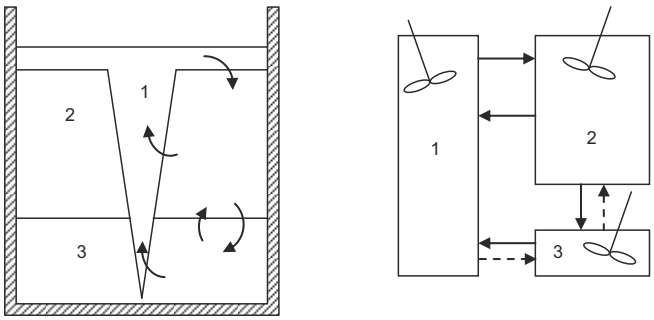

Figure 6-1. Gas-stirred ladle divided into three zones and the configuration of CISTR's.

Setting-up a reactor model of a gas stirred ladle, each zone can be modelled by a CISTR, including the plume. As described by Mazumdar and Evans[2], as the plume rises and broadens, liquid hot metal is entrained from the bulk and the turbulence in the plume zone is high. This results in the reactor model shown on the right hand side in Figure 6-1. Since the main direction of the flow field is upward in the plume and downward along the walls, the circulation flows $3 \rightarrow 2$ and $1 \rightarrow 3$ could probably be neglected. Using this reactor model, Pietzka et al.[4] could effectively predict the settlement of tracer concentrations as measured with their experiments. Also Oeters et al.[3] concluded that models with two or three partial volumes effectively model the macro mixing in the melt. To quantify the volumes of the zones and circulation flow rates Pietzka et al.[4] performed flow field measurements. It may, however, also be done without measurements. The relations derived by Krishnapisharody and Irons[5],[6] can be put to use for this. From analysis of the fundamental aspects of fluid mechanics characterising the bubble plume of a gas stirred ladle, they derived a system of equations describing the plume quantities as a function of the non-dimensional gas flow rate and the dimensionless bath height. Using these equations the volume of the bubble plume zone, the liquid velocities in the plume, and thus the volume flow rates can be quantified for several ladle dimensions and gas flow rates. The division of the remaining volume into the torodial flow zone and the stagnant bottom zone, remains to be estimated. Although in this work the melts have been modelled using less than three zones, for future work it is recommended to apply the division into three zones.

As an alternative to these macroscopic models, the flow and mixing in gas stirred ladles can also be described using Computational Flow Dynamics (CFD).With this, the flow field is calculated in greater detail than with macroscopic models Several references describe the reactor models of gas stirred ladle processes[7]-[9]. Based on the results of this work, however, it is thought that, in order to properly describe the chemical conversion in a well mixed ladle it is most important to describe the formation and behaviour of the particles in detail and that macroscopic flow field models are sufficient for this purpose. As the number of dimensions of the vector describing the particles in the population balance increases, the computational power required to solve the set of equations will quickly rise. Since macroscopic flow field models require little computational power to solve, all power available can be put into the simulation of the complex behaviour of the product particulates. Furthermore, these models offer easier scaling of the ladle dimensions and gas flow rates without the necessity to set-up a new grid.

6.3 Recommendations for future work

For future work on the modelling of ladle injection metallurgy the following route now is recommended: The first step is to obtain thorough understanding of the formation of the reaction products. After initial assessment of the thermodynamics governing the reactions, measurements should be done. This can be done by taking, either on laboratory or industrial scale, samples from the steel or hot metal during the injection of the reagent of study. Using Scanning Electron Microscopy combined with Automated Inclusion Analysis a thorough understanding of the formation, growth and, where applicable, the removal of the product particulates can be obtained.

The next step is to set up a reactor model based on a macroscopic flow field model using three CISTR's representing the three mixing zones of which one represents the bubble plume. This will provide for proper scaling of measurements on laboratory scale and proper representation of the bulk concentrations in the liquid metal in the ladle. Based on the results of the study of the reaction kinetics, for each zone the conversion should be described by a population balance of the product particulates incorporating nucleation, growth by chemical reaction, agglomeration and finally removal of the reaction products by flotation induced by gas injection or electromagnetic stirring where applicable. The terms of this balance can all subsequently be described by generic relations derived from first principles.

Finally, using the results of measurements and parameter studies using the reactor model ways to improve the performance of the injection process can be investigated, aiming on achieving the required product specifications at minimal total costs and identifying causes for loss of efficiency of the injected reactants.

6.4 References

[1] K. R Westerterp, W. P. M. Van Swaaij, A. A. C. M. Beenackers: Chemical Reactor Design and Operation, 2nd Edition (1987) John Wiley & Sons Ltd.

[2] D. Mazumdar and J. W. Evans: Review, Macroscopic models for gas stirred ladles, ISIJ Int. 44 (2004) 447-461.

[3] F. Oeters, W. Pluschkell, E. Steinmetz, and H. Wilhelmi: Fluid flow and mixing in secondary metallurgy, Steel Research 59 (1988) 192-201.

[4] J. Pietzka, E. Steinmetz und H. Wilhelmi: Modelluntersuchungen zur strömung und durchmischung in metallurgischen pfannen, Steel Research 58 (1987) 538-536.

[5] K. Krishnapisharody and G.A. Irons: Fundamental characterization of the fluid mechanics of multi-phase interactions in ladle metallurgy. Proc. Scanmet III, 8-11 June 2008, Luleå, Sweden, pp.589-599.

[6] K. Krishnapisharody and G.A. Irons: A study of spouts on bath surfaces from gas bubbling: part II. Elucidation of plume dynamics, Metall. Mater. Trans. B 38 (2007) 377-388.

[7] L. Jonsson, D. Sichen and P. Jönsson: A new approach to model sulphur refining in a gas-stirred ladle – A coupled CFD and Thermodynamic model. ISIJ Int. 38 (1998) 260-267.

[8] Y. Kwon, J. Zhang and H. Lee: A CFD-based nucleation-growth-removal model for inclusion behaviour in a gas-agitated ladle during molten steel deoxidation. ISIJ Int. 48 (2008) 891-900.

[9] J-P. Bellot, V. De Felice, B. Dussoubs, A. Jardy and S. Hans. Coupling of CFD and PBE calculations to simulate the behaviour of an inclusion population in a gas-stirring reactor. Metall. Mater. Trans. B 45 (2014) 13-21.

[10] D. Ramkrishna: Population balances: theory and applications to particulate systems in engineering. San Diego, CA: Academic Press (2000).

List of used symbols

a_j	chemical activity of phase *j*	-
a_{MgS}	specific surface area of MgS seeds in hot metal	m²/m³
A_p	particle surface	m²
A_{pc}	particle cross-section	µm²
A_{scan}	total scanned sample surface area	mm²
C_f	flotation rate constant of MgS particles	-
d	diameter	m
$d_{p,CaO}$	diameter of injected lime particles	m
$d_{p,MgS}$	diameter of MgS particle	m
D_i	diffusivity of solute *i*	m²/s
e_i^k	interaction coefficients	-
f_1	number density of dispersed particles	-/µm⁴
$f_{1,in}$	number density of particles in incoming circulation flow	-/µm⁴
f_i	activity coefficient of solute *i*	-
f_i*	activity coefficient of component *i* on the interface	-
f_{CaO}	contact fraction of CaO particles in hot metal	-
f_d	fraction of injected magnesium that dissolves in the hot metal	-
$f_{v,MgS,HM}$	volume fraction of MgS in hot metal	-
$f_{v,MgS,p}$	volume fraction of MgS a particle	-
g	gravitational acceleration	m/s²
ΔG_j	Gibbs energies of formation of compound *j*	kJ/mole
h_i	Henrian activity of solute *i*	[wt%]
J_i	molar flux of substance *i*	mole/m²/s
$k_{S,CaO}$	mass transfer coefficient of dissolved sulphur to lime particles	m/s
$k_{i,MgS}$	mass transfer coefficient of Mg or S to MgS particle surface	m/s
$k_{m,i}$	mass transfer coefficient of solute *i*	m/s
K_j	equilibrium constant of compound *j*	-
L_{im}	immersion depth of the lance	m
m, m_i,	mass, mass of substance *i*	kg

$m_{Mg,injected}$	injected amount of magnesium	kg
$\dot{m}_{CaO}, \dot{m}_{Mg}$	injection rates of CaO and Mg into the hot metal bath	kg/s
M_i	molar mass of substance *i*	kg/mole
n_i	amount of substance *i*	mole
p	pressure	kPa
P_{MgS}	solubility product of MgS in hot metal	ppm²
Q_{circ}	circulation flow rate	m³/s
r_i	reaction rate of solute *i*	[wt%]/s
r_l	radius of the ladle	m
R	gas constant	8.314 J/mole/K
Re	Reynolds number	-
Sc	Schmidt number	-
Sh	Sherwood number	-
t	time	s
T	temperature	K
x	vector denoting particle properties	
X_i	molar fraction of substance *i*	-
$\dot{X}$	vector denoting rate of change of particle properties	
v	velocity	m/s
V	volume	m³
$V_{m,j}$	molar volume of phase *j*	m³/kmole

Concentrations

$[\%C]_{sat}$	carbon saturation concentration by mass in hot metal	%
$[ppmi]$	mass fraction of substance *i* in hot metal	ppm
$[\%Mg]$, $[\%S]$	concentration of dissolved Mg and S in hot metal bulk	wt%
$[\%MgS]$	concentration of dispersed MgS in hot metal bulk	wt%
$[\%i]_{CaO}$	concentration of solute *i* on CaO/hot metal interface	wt%
$[\%Mg]_{MgS}$, $[\%S]_{MgS}$	concentration of Mg and S on MgS/hot metal interface	wt%
$[\%i]$	concentration of solute *i*	wt%
$[\%i]_{in}$	concentration of solute *i* in incoming circulation flow	wt%
$[\%i]$*	concentration of solute *i* at reaction interface	wt%
$[Mg]$, $[S]$	concentration of Mg and S in hot metal bath	mole/m³

$[Mg]_{MgS}$, $[S]_{MgS}$	concentration of Mg and S on reaction interface	mole/m³
ρ_j	density of substance *j*	kg/m³
ϕ_{vst,N_2}	nitrogen feed rate, in standard cubic meters	Nm³/s
$\phi_{v,g}$	gas volume flow rate	m³/s
η_{Mg}	overall efficiency of injected magnesium	-
η	dynamic viscosity	Pa·s
τ	residence time	s
τ_p	residence time of injected powder in the hot metal bath	s
ν	kinematic viscosity	m²/s

Subscripts

atm	atmospheric
bulk	bulk
d	droplet
HM	hot metal
p	particle
plume	plume
slag	liquid slag
st	standard
steel	liquid steel

Acknowledgements

Vrij snel na mijn aantreden bij Corus RD&T in 2001 nam Dirk van der Plas het initiatief voor dit onderzoek en ook om daar promotie voor mij van te maken. Dit idee werd van harte ondersteund door Rob Boom en ik ben er vervolgens mee aan de slag gegaan. Ik begon met het modelleren van de ruwijzerontzwaveling maar kwam al snel tot de conclusie dat metingen nodig waren. Hans ter Voort en Lammert Knorren hebben mij veel geleerd over de ruwijzerontzwaling in de praktijk en hebben mij de gelegenheid gegeven om de metingen uit te voeren en proeven te doen bij de ROZA's in Oxystaalfabriek 2. Daarbij ben ik enthousiast geholpen door Gerrit Barendregt. Met de ruwijzermonsters die we toen hebben genomen, toog ik naar het Ceramic Research Centre waar Max Koolwijk me kennis heeft laten nemen van de wondere wereld van de elektronenmicroscopie en de ruwijzermonsters voor me heeft geanalyseerd. Later heeft Corrie van Hoek dit overgenomen. Enno Zinngrebe heeft me vervolgens geholpen met de analyse en presentatie van de grote hoeveelheid meetgegevens. Ongeveer tegelijkertijd deed Wouter Tiekink zijn metingen aan de calciumbehandeling van aluminiumrustig staal. De mooie resultaten van deze metingen heb ik mogen gebruik om daar, samen met Mostafa Biglari ook een reactormodel van de te maken.

Samen met Rob Boom heb ik verscheidene conferenties mogen bezoeken waar ik deze mooie resultaten mocht presenteren en in contact kwam met de experts op mijn vakgebied. Ik vond dit geweldige ervaringen. Gedurende vele jaren heeft Rob me veel geholpen door mijn werk regelmatig van commentaar te voorzien en met me te bespreken.

Mijn chefs, achtereenvolgend Dirk van der Plas, Aart Overbosch en San Filbri hebben mij in mijn werk ruimte gegeven om dit onderzoek te kunnen doen en dit proefschrift af te ronden. Veel dank daarvoor. Ook mijn collega's van de convertersectie hebben me dit laten afronden.

Mijn eerste ervaringen met gloeiend heet staal deed ik op in de smederij van mijn pake. Ik wilde hier graag een foto van in mijn proefschrift plaatsen maar omdat er geen foto's van waren, heeft mijn neef Bastiaan Epker daar een mooie illustratie van gemaakt die ik in mijn proefschrift mocht plaatsen.

Boven alles, dank aan mijn ouders, Hans en Anneke, en mijn vrouw Ester voor hun betrokkenheid bij mijn werk en hun aansporingen om dit proefschrift af te ronden.

Curriculum Vitae

Name:	Hessel-Jan Visser
Date of birth	22 January 1971
Place of birth	Sneek, The Netherlands

2011-to date	Tata Steel Europe
	Senior Process and Product Engineer Steelmaking
	Basic Oxygen Steel Plant No.2 IJmuiden
2008-2011	Corus RD&T
	Principal Researcher
	Knowledge group Steelmaking
2001-2008	Corus RD&T,
	Researcher
	Knowledge group Process Kinetics and Reactor Design
1997-2001	NUON
	Trainee
1995-1997	University of Twente
	Post-Graduate Student
	Faculty of Chemical Engineering
1989-1995	University of Twente
	Student
	Faculty of Mechanical Engineering
	Department of Thermal Engineering
1983-1989	Lienward College Leeuwarden, Atheneum

Publications

Hessel-Jan Visser and Rob Boom. Process Modelling of Ladle Desulphurisation by Injection of CaO/Mg and CaC_2/Mg Mixtures in 300 Ton Ladles. Proceedings of the 3rd International Congress on the Science and Technology of Steelmaking, May 9-12, 2005, Charlotte (NC), USA. AIST, Warrendale (PA), USA, pp. 369-379.

Rob Boom and Hessel-Jan Visser. Advanced process modelling of hot metal desulphurisation by Injection of Mg and CaO. 12th ISIJ-VDEh Seminar on Fundamentals of Iron and Steelmaking, Kyushu Institute of Technolgy, Kokura, Japan, 21-22 November 2005, pp.26-32.

Hessel-Jan Visser, Elizabeth Graveland, Lammert Knorren, Aart Overbosch, Rob Boom. Optimisation of hot metal desulphurisation at BOS2 Corus Strip Products IJmuiden. Proceedings of the 5th European Oxygen Steelmaking Conference EOSC2006, 26-28 June 2006, Aachen, Germany, pp. 3-8.

Hessel-Jan Visser and Rob Boom. Advanced process modelling of hot metal desulphurisation by injection of Mg and CaO. ISIJ International 46 (2006) 1771-1777.

Selected Paper. Hessel-Jan Visser, Elizabeth Graveland, Lammert Knorren, Aart Overbosch, Rob Boom. Optimisation of hot metal desulphurisation at BOS2 Corus Strip Products IJmuiden. La Revue de Métallurgie-CIT 103 (2006) 487-492.

Hessel-Jan Visser, Mostafa Biglari and Rob Boom. Simulation of the Ca-treatment of Al-killed liquid steel. Proceedings of the 28èmes Journées Sidérurgiques Internationales ATS, Paris 13-14 Dec. 2007, pp. 147-154.

Selected Paper. Hessel-Jan Visser, Mostafa Biglari and Rob Boom. Simulation of the Ca-treatment of Al-killed liquid steel. La Revue de Métallurgie - CIT 105 (2008) 172-180.

Hessel-Jan Visser and Rob Boom. Development of a reactor model of hot metal desulphurisation on an industrial scale. Proceedings of the SCANMET III-3rd International Conference on Process Development in Iron and Steelmaking, Volume 2, 8-11 June 2008, Luleå, Sweden, pp. 147-156.

Hessel-Jan Visser, Fokke Zwaan, Manuel Atienzo, Coen van Kralingen, Jan Brockhoff and Pieter Broersen. Continuous improvement of hot metal desulphurisation at Tata Steel BOS No.2. Proceedings of the 6th European Oxygen Steelmaking Conference, 6-7 September 2011, Stockholm, Sweden , pp. 1-5.


TATA STEEL

TU Delft

materials
innovation
institute